A Study on Precise Measurements and On-Line Diagnosis for Laser-Accelerated Ion Beams

Kanasaki, Masato

(Degree)
博士（工学）

(Date of Degree)
2014-03-25

(Date of Publication)
2015-03-01

(Resource Type)
doctoral thesis

(Report Number)
甲第6136号

(URL)
https://hdl.handle.net/20.500.14094/D1006136

Doctoral Dissertation

A Study on Precise Measurements and On-Line Diagnosis for Laser-Accelerated Ion Beams

（レーザー駆動イオン加速におけるイオン計測の高精度化とオンライン化に関する研究）

January 2014

Graduate School of Maritime Sciences, Kobe University

Masato KANASAKI

Contents

Chapter 1 Introduction

1.1 Laser-driven ion acceleration

Laser-driven ion acceleration experiments have been actively carried out at intense laser facilities [1]. When a target material was irradiated with a focusing intense laser, high energy ions with multi-tens of MeV were generated by laser-plasma interaction. The acceleration field for ions, which created by intense laser, could reach up to ~TV/m theoretically. The acceleration gradient indicates six orders of magnitude higher than the case of conventional radio-frequency ion accelerators. Such an efficient acceleration field can reduce the total size of accelerator. Therefore, the applications of laser-accelerated ion beams have also been studied all over the world such as medical ion accelerator for cancer therapy.

The novel ion acceleration technique has significant merits from the point of view of many applications. However, it still has a number of issues to overcome, such as increasing the particle energy, control of the beam, and stability of the acceleration parameters. To provide a possible resolution to these problems, precise characterizations of laser-accelerated ion beams are one of the most important matters.

The present study is intended to characterize the laser-accelerated ion beams from the targets of thin foil and cluster-gas.

1.1.1 Intense laser-matter interaction

The ultra-short pulse (a few tens of fs) laser systems are able to generate the electromagnetic pulses with energy compression leading the intensities several orders of magnitude above the relativistic threshold ($I\lambda^2 \geqq 1.37\times10^{18}$ W cm^{-2} μm^2), i.e. the intensity of the laser wave in which oscillatory energy of an electron beyond the rest energy [2]. Here, I is laser-intensity and λ is wavelength of laser. When this type of laser irradiates to the target, a significant amount of plasma electrons is accelerated up to the relativistic velocity during a few cycle of laser electric field [3,4]. Additionally, under the action of a high-irradiance laser, electron motion is governed by both magnetic and electric fields in the form of the Lorentz force. The electrons are accelerated towards the laser traveling direction. While the electrons are accelerated forward direction, the ions respond slower and relatively slowly varying (quasi-static) charge-separation fields are formed between the displaced forward electrons and the rest of the plasma. In addition, the electron current leads to quasi-static magnetic field generation. At a longer time scale, protons are accelerated by the slowly varying plasma fields, which have the highest charge-to-mass ratio among the ions, and then heavier ions can follow the protons.

Figure 1.1 shows the world-wide record of maximum energy of laser-accelerated ion as a function of laser intensity. The results of large-scale single-shot Nd:glass lasers are plotted by red. These results were obtained by the experiments using solid targets such as thin foil targets. The repetition rates of Nd:glass lasers, for example, are single shot per day. Therefore, Nd:glass lasers are not suitable for applications even if it can produce high energy ions such as 68 MeV, which is the world record of the energy of laser-accelerated ions as indicated (a) in Fig. 1.1.

On the other hand, the results of compact high repetition Ti:Sapphire laser systems are plotted by blue dot and green dot, which results were obtained by the experiments using solid targets such a thin foil target and cluster-gas target, respectively.

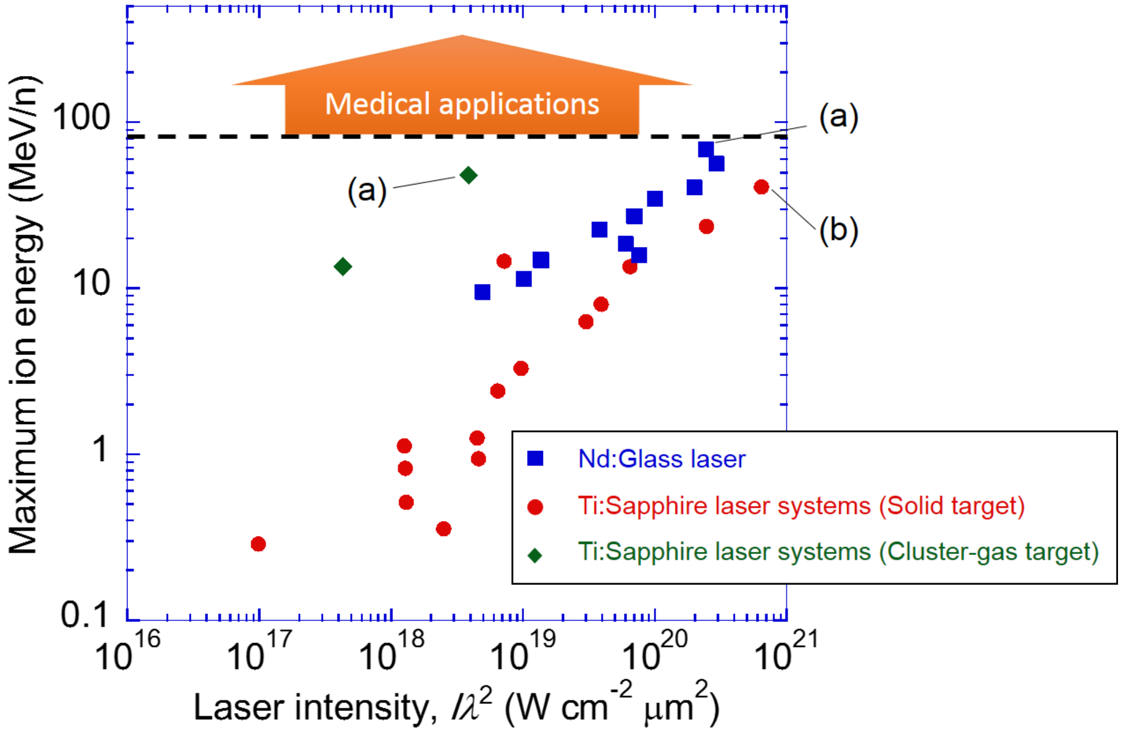

Fig. 1.1 Maximum energy of laser-accelerated ion as a function of laser intensity.

The repetition rates of Ti:Sapphire laser systems, for example, are 10 Hz. Therefore, Ti:Sapphire laser system is easier to utilize for the application such as medical ion accelerator for cancer therapy.

The present study was conducted with J-KAREN laser in Japan Atomic Energy Agency, Kansai Photon Science Institute, JAEA-KPSI [5]. J-KAREN is a femtosecond high intensity laser system that combines both Ti:sapphire chirped pulse amplification (CPA) and optical parametric CPA (OPCPA) techniques. The system consists of two successive CPA stages, where the second one includes a three-pass Ti:sapphire final booster amplifier pumped with the second harmonic from a high energy Nd:glass laser.

Recently, protons with the maximum energy of 40 MeV were accelerated using thin foil target conducted with J-KAREN laser, which is indicated by (b) in Fig. 1.1 [6]. And also He ions with the maximum energy of 50 MeV/n are accelerated from cluster-gas target using the J-KAREN laser, which is indicated by (c) in Fig. 1.1 [7]. In the near future, it can be expected that the maximum energy of laser-accelerated ions will reach up to 80 MeV/n with increasing the laser intensity, which is the minimum requirements for the medical applications.

1.1.2 Characteristics of mixed radiation field by laser plasma

In the laser-driven ion acceleration experiments, high energy electrons and energetic ions are produced by intense laser-matter interaction as described in section 1.1.1. In addition, photons with wide energy spectrum, including X-rays, are also generated in laser plasma [8,9]. In the case of solid targets such as thin foil targets, the laser-accelerated electrons traveled to the laser propagation direction with a Boltzmann-like energy distribution which maximum energies were several-tens of MeV. On the other hand, in the case of cluster-gas target, a significant amount of well-collimated high energy electrons with the maximum energy of 200 MeV were accelerated. In both cases, especially cluster-gas target, such high energy electrons could produce high energy photons which exceed the threshold of photo-nuclear reactions via bremsstrahlung processes. Consequently, the photons could produce photo-neutrons as secondary particles in a series of photo-nuclear reactions [10]. And also, the high energy laser-accelerated protons could produce secondary particles such as neutrons in a series of nuclear reactions. Therefore, the ions from laser plasma should be regarded as in the mixed radiation field.

The generated ions could be classified two components. One of the two was generated by the Coulomb explosion mechanism [11], which consists of highly charged ions with the energies below a few MeV. The Coulomb explosion components indicated non-directional ion beams. On the other hand, the other component was accelerated by electric field which created by intense laser such as Target Normal Sheath Acceleration (TNSA) mechanism of thin foil target (see section 3.1). The energies of this component were widely spread up to multi-tens of MeV. The ions accelerated by TNSA mechanism indicated the directional beam for the target normal direction [1,12].

Thus, the intense laser-plasma interactions generated the mixed radiation field which was composed of not only ions, electrons, X-rays, and gamma-rays, but also neutrons. The diagnosis of laser-accelerated ion beams must be carried out in the fields contaminated with such noise components.

1.2 Current status of measurement technique for laser-accelerated ion beams

Diagnosis of ion beams in fields with mixed radiations of gamma rays, X-rays, and high-energy electrons attracts much attention in the field of laser-driven ion accelerations, because the precise characterization of accelerated ions is crucial to the development of a laser ion accelerator for medical and industrial applications. Because the laser-accelerated ion beams have wide spread energy distributions and it in the mixed radiation field, the conventional ion measurement systems cannot be applied. Thus, a lot of diagnosis techniques for laser-accelerated ion beams have been developed. In this section, the detectors have been introduced, which have been utilized in the laser-driven ion acceleration experiments.

1.2.1 Passive detectors

In the laser-driven ion acceleration fields, the passive detectors are mainly applied as ion detector such as CR-39 track detector, radiochromic film (RCF), and imaging plate (IP). These detectors are applied to obtain the energy spectrum and the spatial distributions of laser-accelerated ion beams. And also, these detectors are utilized as two-dimensional imaging detectors for proton imaging technique [13]. The laser-accelerated proton beams from thin foil targets can be a particle probe for a diagnostic tool for the detection of electric fields in laser-plasma interaction experiments.

Recently, solid state nuclear track detectors [14] such as CR-39 detectors have been extensively used in laser-driven ion acceleration experiments [8,15]. This is because the CR-39 detectors have the great advantages of being insensitive to photons and electrons and capable of detecting only ions [16]. CR-39 track detector can record the high energy protons up to 27 MeV (see section 2.1.2). It can also registrate the tracks of relativistic heavy ions heavier than Li. Since each ion create one etch pit, CR-39 can be utilized for absolute fluence diagnosis.

In the case of RCF, the absorbed dose of energetic ions deposited in the film has been measured from the changes in optical density undergone by the film, yielding information on the number and energy of the ions [17]. In order to measure the signals of only ions, the RCF detectors usually use sandwich with CR-39, because the RCF are sensitive for contaminants such as X-ray, gamma-ray, and electrons.

The IP is a two-dimensional detector which is categorized as photo stimulable luminescence detector [18]. Using the read out system, the radiation signals on IP have been visualized as two dimensional images. The IP are often used as the detection part of Thomson parabola spectrometer [19].

1.2.2 On-line detectors

The on-line detector such as plastic scintillators, fluorescent screens, and micro channel plate (MCP), which is an aggregate of micron sized photo multiplier tube, are utilized as laser-accelerated ion detectors.

The plastic scintillators are usually used for the detection part of time-of-flight (TOF) method

[20]. Thanks to the short decay constant of scintillation, TOF with plastic scintillator system can measure the energy spectrum up to around 10 MeV for protons with high resolution.

The fluorescent screens and MCP are used for the detection part of the Thomson parabola system as two-dimensional imaging detectors. MCP is usually combined with a fluorescent screen when the number of ions is small [21]. A luminescence of fluorescent screen is obtained by a charged coupled device (CCD) [22].

These detectors are sensitive not only ions but also high energy electrons and photons. To apply these detectors, the ions and electrons must be separated to measure the laser-accelerated ions. In addition, the detectors and CCDs are to be shielded by filters such as Al foil to diminish the noise from photons and electrons.

1.3 Structure of the thesis

This thesis is structured in following:

- Chapter 1 is the introduction and motivation of this thesis. This chapter explains outline of laser-driven ion acceleration experiment and the characteristics of mixed radiation field generated by intense laser-matter interaction. The status of measurement technique for laser-accelerated ions is also described.

- In chapter 2, the basic study of ion detectors, CR-39, and ZnS(Ag) fluorescent screen is described. Brief description of the Monte Carlo particle transportation code, PHITS, and the three-dimensional magnetic and electric field analysis software, AMaze, are also given

- Chapter 3 describes the developed diagnosis techniques for laser-accelerated ions from thin foil targets. One of two is the precise measurement of a high energy component using stacked CR-39 detector. The other is on-line Thomson parabola system using ZnS(Ag) fluorescent screen.

- Chapter 4 explains the new diagnosis technique for high energy He ions above the threshold level of CR-39 using back-scattered particles. Such high energy He ions are produced from cluster-gas targets. In the diagnosis, single layer CR-39 detector can work as ion beam intensity profiler.

- Chapter 5 describes the evaluation of photo-neutron fluxes in laser-driven ion acceleration using cluster-gas target. The development of discrimination method of etch pits created by laser-accelerated protons and recoiled protons by photo-neutrons is also explained.

- Design of the measurement system of laser-accelerated ions with less photo-neutron flux at ion detector position is given in chapter 6.

- Chapter 7 is the conclusions of the present thesis.

Chapter 2 Ion detector and calculation code

2.1 Solid state nuclear track detector, CR-39

CR-39 is a commonly used as Solid State Nuclear Track Detector, SSNTD, in various field of research such as nuclear physics, neutron dosimetry, cosmic ray detection and laser-driven ion acceleration [8,23,24]. Firstly, CR-39 has been developed as an optical material by Colombia Chemical Division in 1940s [25]. CR-39 is a colorless and transparent plastic, which is polymerized diethylene glycol bis(allyl carbonate) liquid monomer. Figure 2.1 shows the repeat unit of CR-39.

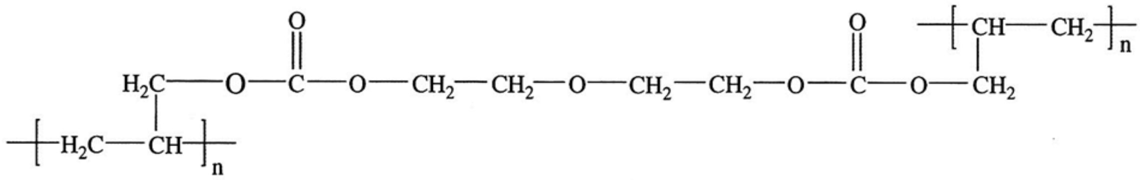

Fig. 2.1 Repeat unit of CR-39

The molecular formula is $C_{12}H_{18}O_7$ and the density is 1.31 g/cm^3.CR-39 has two carbonate ester bonds on the both side of ether bond in a repeat unit. The carbonate ester and the ether bond are well known as radiosensitive groups [26].

In 1978, CR-39 has been discovered as a superior SSNTD material by Cartwright et al. Before discovered CR-39, polyethylene terephthalate (PET), polycarbonate (PC), and cellulose nitrate (CN) have been used as SSNTD [27-29]. These SSNTD materials show the lower sensitivity than CR-39. For example, CN can detect alpha-rays with below a few MeV (stopping power more than 100 keV/μm), on the other hand, CR-39, which is copolymerized with *N*-isopropylacrylamide (NIPAAm), can detect 27 MeV protons (stopping power more than 2.6 keV/μm) at the maximum [30]. In the recent study, modified chemical structure along ion tracks are gradually revealed by means of Fourier transform infrared, FT-IR, spectroscopy method [26].

First of all, the fundamental study of SSNTD has been described including the analysis techniques in section 2.1.1. Secondary, the characteristics of CR-39 has been introduced in section 2.1.2.

2.1.1 The fundamental study of SSNTD

When an ion entered into the SSNTD, it provides the kinetic energy to the material and loses the own energy. The mainly two type of chemical bond breaking are occurred in the process of losing the energy. One of the two is primary ionization process and the other is ionization by secondary electrons. By means of these processes, the damaged region, which is called ion track, can be modified. The ion track region is preferentially etched by chemical etching treatment compared to the pristine region, and then, the etch pit is created.

The size of etch pit allow us to predict the ion species and incident energy. And also, each etch pit shows the unique growth behavior depends on the stopping power, which allow us to understand the more detail information of each incident ion. The etch pit geometry in detail and analysis technique has been studied by pioneering researchers [31-33]. In this study, the etch pit analysis techniques have been chosen for precise diagnosis of laser-accelerated ion beams.

2.1.1.1 Etch pit growth behavior

The sensitivity of SSNTD for a charged particle is defined as ratio of track etching sp eed V_t and bulk etching speed V_b, which is described as Eq. 2.1.

$$S \equiv \frac{V_t}{V_b}, \tag{2.1}$$

where S is sensitivity of SSNTD. And also, the V_t/V_b is called as etch rate ratio. Figure 2.2 shows the ideal etch pit profile.

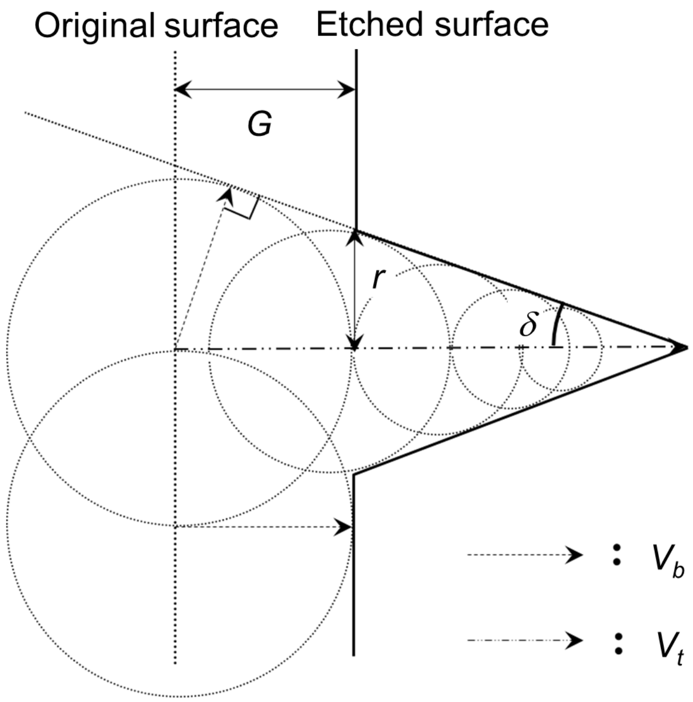

Fig. 2.2 An ideal etch pit profile at constant V_t.

The relation between etch pit tip angle δ and etch rate ratio can described as:

$$\sin\delta = \frac{V_b}{V_t} = \frac{1}{S}, \tag{2.2}$$

From Eq. 2.2, the etch pit tip angle indicate the etch rate ratio directly, but tip angle is hard to obtained by usual optical microscope observation.

Here, it assumed that the V_t is constant. The etch rate ratio S will be constant, because of V_b is always constant in usual chemical etching treatment. In this case, etch pit profile will be ideal conical shape and the sensitivity can be described as follows:

where, r is etch pit radius and G is thickness of layer removed as shown in Fig. 2.2. Practically, Eq. 2.3 is applied to determine the sensitivity of etch pit, because these parameters can be easily to obtained by optical microscope observation.

$$S = \frac{1+\left(\frac{r}{G}\right)^2}{1-\left(\frac{r}{G}\right)^2}. \tag{2.3}$$

However, the etch rate ratio will be changed which depends on the depth in SSNTD, i.e. the sensitivity will change with the etching time, because of the stopping power is not constant in SSNTD. Figure 2.3 shows the sensitivity of alpha-particles for etching time 2 h and 5 h.

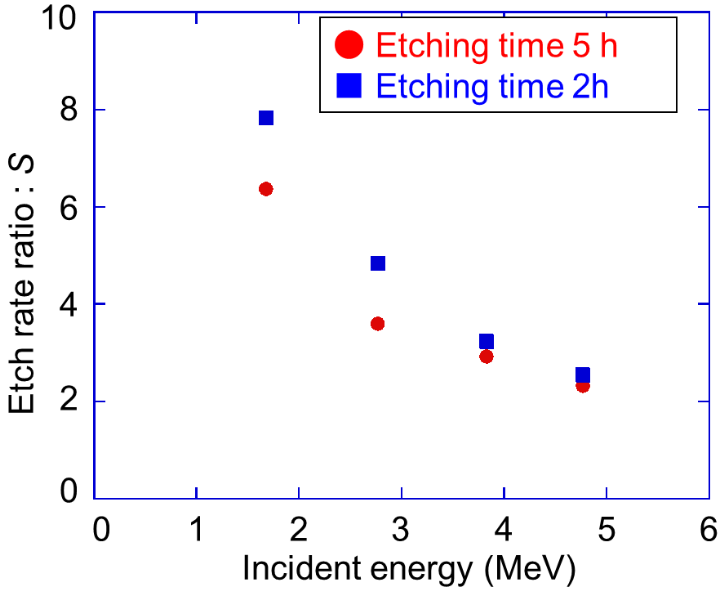

Fig. 2.3 Etching time dependence of etch rate ratio.

These results indicate higher sensitivity shows with shorter etching time at the same energy. Namely, track etching speed is not constant in SSNTD.

Accordingly, the etch rate ratio of SSNTD will be considered with the depth dependence of track etching speed as a function of depth in detector. Figure 2.4 shows the etch pit profile with the depth dependence of track etching speed. Each point is named as shown in Fig. 2.4.

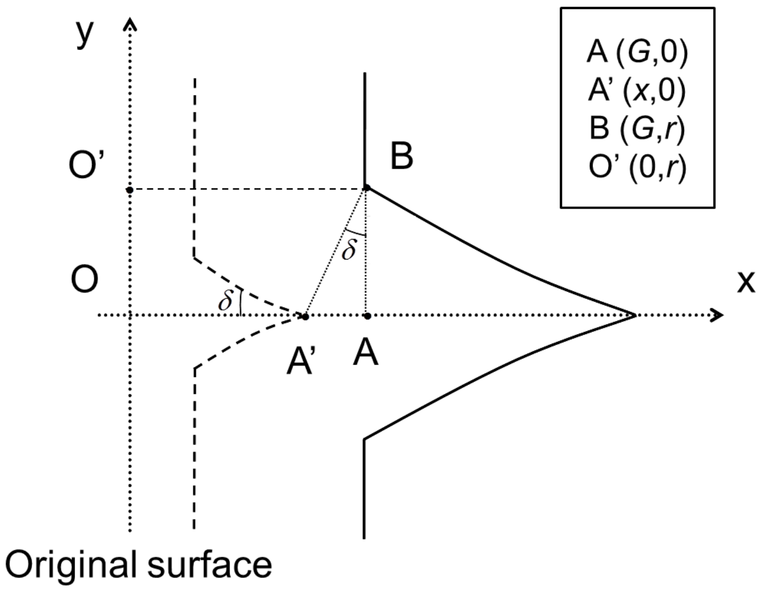

Fig. 2.4 Etch pit profile for various track etching speed.

An ion was entered into the SSNTD with normal incidence from point *O*. The horizontal axis x indicates the depth in detector and the vertical axis y indicates the surface direction. The dashed line indicates the previous etch pit profile of the solid line one. Here, it has been considered that the creation process of point *B*. One of the two way to the point *B* is *O'B*, which is occupied only bulk etching process. The other way is consisted of *OA'* (track etching) and *A'B* (bulk etching). The point B is created by the same etching time, thus the Eq. 2.4 has been obtained,

$$\frac{\overline{O'B}}{V_b} = \int_0^x \frac{d_x}{V_t(x)} + \frac{\overline{A'B}}{V_b}, \tag{2.4}$$

where, V_t(x) is track etching speed with depth dependence. The left side indicate the time to etch *O'B* by bulk etching speed. And the right side indicate the time to etch *OA'* with track etching speed and *A'B* with bulk etching speed.

The distance of *AA'* and *A'B* can be described as follows using the coordinates of the point in Fig. 2.3 and Eq. 2.2:

$$\overline{AA'} = r\frac{1}{\sqrt{S(x)^2 - 1}} = G - x, \tag{2.5}$$

$$\overline{A'B} = \frac{G-x}{\sin\delta} = r\frac{S(x)}{\sqrt{S(x)^2 - 1}}. \tag{2.6}$$

When the substitute Eq. 2.6 for Eq. 2.4 and multiply V_b for both side, Eqs. 2.7 and 2.8 are obtained,

$$G = h(x) + r\frac{S(x)}{\sqrt{S(x)^2 - 1}}, \tag{2.7}$$

$$h(x) = \int_0^x \frac{1}{S(x)} dx , \tag{2.8}$$

where, h(x) is integration of a reciprocal of the sensitivity with depth dependence S(x). From Eqs. 2.5 and 2.7, the etch pit radius r and the thickness of layer removed G are described as follows:

$$r = \{x - h(x)\}\sqrt{\frac{S(x)+1}{S(x)-1}} , \tag{2.9}$$

$$G = \frac{xS(x) - h(x)}{S(x)-1} . \tag{2.10}$$

Thus, the coordinates of the point B has been described. Using these formulae, the etch pit profile can be obtained by etch rate ratio with depth dependence S(x).

On the other hand, the etch pit growth curve is obtained by multi-step etching technique, which the chemical etching and the microscopic observations of pit size are repeated. The slope of the etch pit growth curve β is described as follow:

$$\beta = \frac{dr}{dG} = \frac{\left(\frac{dr}{dx}\right)}{\left(\frac{dG}{dx}\right)} = \sqrt{\frac{S(x)+1}{S(x)-1}} . \tag{2.11}$$

The etch rate ratio S(x) can be derived from Eq. 2.11. The relation between range of an ion R_0 and residual range R, which is the distance from etch pit tip to the end of range, can described as Eq. 2.12.

$$R = R_0 - x , \tag{2.12}$$

where x is the distance between R_0 and R. Using this relationship, the etch rate ratio can rewrite as a function of residual range R as follows:

$$S(R) = S(x) = \frac{1+\beta^2}{1-\beta^2} , \tag{2.13}$$

$$R = R_0 - \left(G - r\frac{1-\beta^2}{2\beta}\right). \tag{2.14}$$

The etch rate ratio, i.e. the response of SSNTD, can be calculated using the parameter which is obtained by multi-step etching technique and Eqs. 2.13 and 2.14.

2.1.1.2 Determination of range in SSNTD

Figure 2.5 shows the etch pit profile before and after rounded out with solid line and dashed line, respectively. The round out is indicated that etching exceeded the range of particle.

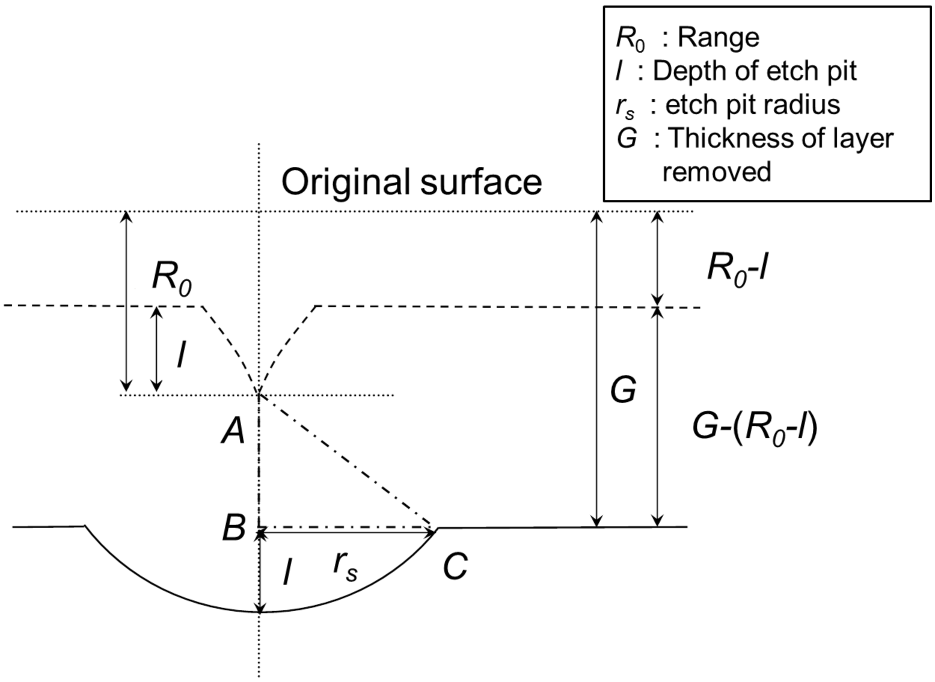

Fig. 2.5 Etch pit profile before and after rounded out.

The distance between each point is indicated in Fig. 2.5. The depth of the etch pit *l* will never change before and after round out. The lengths of the triangle ABC are described as follows:

$$\overline{AB} = G - R_0, \tag{2.15}$$

$$\overline{BC} = r_S, \tag{2.16}$$

$$\overline{CA} = G - (R_0 - l). \tag{2.17}$$

Appling the Pythagorean theorem for triangle ABC, the r_s^2 and R_0 can be derived as follows:

$$r_S^2 = 2lG - 2R_0 l + l^2, \tag{2.18}$$

$$R_0 = G + \frac{1}{4}\left(\frac{dr_S^2}{dG}\right) - \frac{r_S^2}{\left(\frac{dr_S^2}{dG}\right)}. \tag{2.19}$$

From the Eq. 2.18, the squared radius r_s^2 is expressed as a linear function of *G*. Therefore, the growth curve of the etch pit squared radius after round out part will indicate the linear function. And also the range R_0 can be determined from the slope of linear function, i.e. $dr_s^2/dG=2l$, using Eq.2.19. Accordingly, the range R_0 can be calculated by only using the usual parameter of the etch pit which is obtained by multi-step etching technique.

2.1.1.3 Evaluation of traveling direction

The growth curve is defined as an evolution of the radius r of a basal plane of a conical etch pit as a function of the thickness G of a removed surface layer after the chemical etching process. Since r is connected with both of the bulk etch rate V_b and the track etch rate V_t, the detailed etch pit structure and the traveling direction of an ion with respect to the surface can be identified. Concerning etch pit structures, on the basis of the constant-two-velocity model [34], where V_b and V_t are assumed as constant, perfect conical profile etch pits are created in the case with normal incidence ions as shown in section 2.1.2.1.

In actual experiments, however, the pit profiles usually deviate from the perfect conical to trumpet or bell profiles, because V_t varies along the etchable track depending on the rate of change of the stopping power, i.e., the traveling direction of the ion with respect to the surface. Fig 2.6 shows the relationships between etch pit structures and growth curve for three patterns of etch pit.

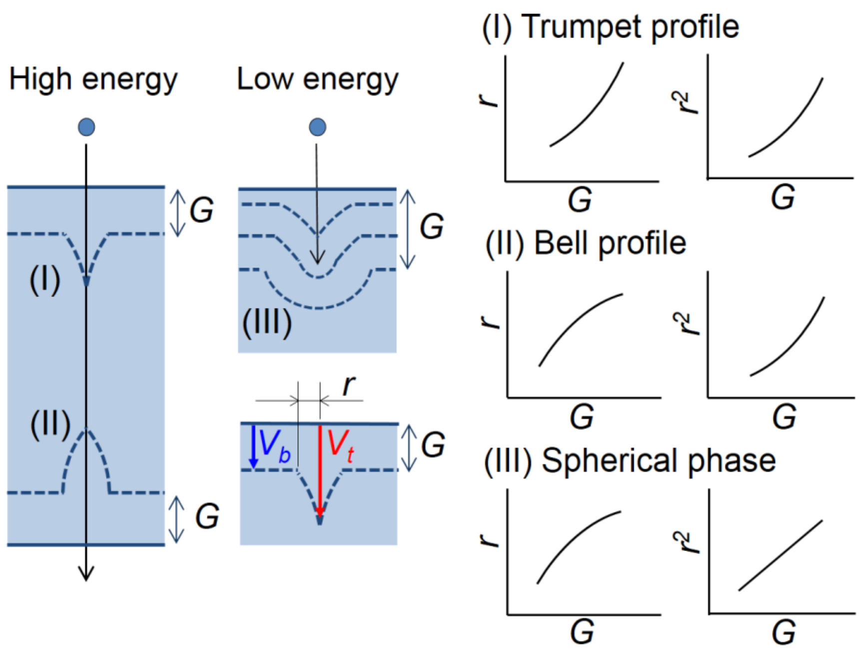

Fig. 2.6. Relationships between pit structures and growth curves. (I) a trumpet profile, (II) a bell profile, and (III) a spherical phase. The broken lines represent cross-sectional profiles of the etched surfaces.

The trumpet profile is created when the ions pass through the CR-39 surface from outside [case (I) in Fig. 2.6]. Since the stopping power along the track etching increases, V_t becomes larger with an increase in the etching depth. Therefore, the growth curve for r is characterized by a convex-downward increasing function of G. In this case, once the track etching reaches the end of the ion's penetration range, V_t equals to zero and etching only with V_b, that is, over-etching, proceeds, resulting in rounding off the tip of the trumpet profile. A further etching beyond the particle range widens the trumpet profile wall, eventually resulting in a spherical shallow structure [case (III) in Fig. 2.6]. According to the comprehensive theory of etch pit [31,35], this final stage is characterized by the variation of the radius squared r^2, that is, r^2 is linear to G, while the growth curve for r is characterized by a convex-upward increasing function of G.

On the other hand, the bell profile is created when the ions passed through the CR-39 surface from inside [case (II) in Fig. 2.6]. In this case, since the stopping power along the track etching decreases, V_t becomes smaller with an increase in the etching depth. Therefore, the growth curve for r is characterized by a convex-upward increasing function of G.

Accordingly, traveling direction for each ion can identified by etch pit growth behavior based on the multi-step etching technique.

2.1.2 Characteristics of CR-39

CR-39 has the higher sensitivity than any other SSNTD material, because of the slow bulk etching speed V_b against the track etching speed V_t. And also, CR-39 keep extremely flat surface even after the chemical etching process. Therefore, CR-39 can detect protons and heavy ions with obvious etch pit open mouth.

When an ion entered into the CR-39, it creates semi-permanent local damage along the track. X-rays, gamma-rays, and electron also create semi-permanent damage, but the damage region spread widely and the damage density is lower than that of an ion. Therefore, X-rays, gamma-rays, and electron cannot produce any etch pit, only an ion can create the etch pit [16]. This is an advantage to use the CR-39 as ion detector in mixed radiation field such as laser-driven ion acceleration. Nevertheless, low linear energy transfer, low-LET, particle such as high energy protons which exceed the threshold of CR-39 cannot produce the etch pit. The low-LET particle also create the damage but the damage density is too low to create the etch pit. Table 2.1 shows the detection threshold of each type of CR-39 for protons.

Table 2.1 Detection thresholds of CR-39

BARYOTRAK	~3 MeV
HARZLAS (TD-1)	~20 MeV
HARZLAS (TNF-1)	~27 MeV

Three type of CR-39, BARYOTRAK, HARZLAS (TD-1), and HARZLAS (TNF-1), are provided by Fukuvi Chemical Industry Co., Ltd, Japan. BARYOTRAK were produced from the highly purified monomer. HARZLAS (TD-1) which contain a small quantity of antioxidant shows the higher sensitivity than BARYOTRAK up to 20 MeV. HARZLAS (TNF-1) has the highest sensitivity in CR-39 detectors, which is copolymerized with NIPPAm.

The maximum observable fluence is also threshold for CR-39 detector. Table 2.2 shows the threshold of the fluence in the cases of using optical microscope and atomic force microscope, AFM.

Table 2.2 Maximum observable fluence

Optical microscope	~10^5 ions/cm^2
AFM	~10^9 ions/cm^2

The usual chemical etching process is performed in 6M-KOH solution kept at 70℃ for more than 1 hour, and the size of etch pit open mouth was enlarged more than a few μm to observe by optical microscope. In this case, if the fluence exceeded the threshold, the precise observation cannot be carried out because the etch pits are overlapped each other. In the special case, the threshold is raised up to 10^9 ions/cm^2 by combination of AFM and short time etching.

The next topic is the thickness of layer removed *G* of CR-39. The thickness of layer removed is a critical important parameter for analysis of CR-39. In section 2.1.1, the thickness of layer removed has been utilized to determine the ranges and traveling directions. Generally, the bulk etching speed is 2 μm/h for CR-39, but it is necessary that more detail value of the thickness of layer removed to precise analysis. A few methods exist to evaluate the thickness of layer removed such as AFM method [36]. In this study, the thickness of layer removed has been determined by the etch pit size which created by fission fragment. Figure 2.7 shows the cross sectional view of the etch pit which created by the fission fragment from ^{252}Cf.

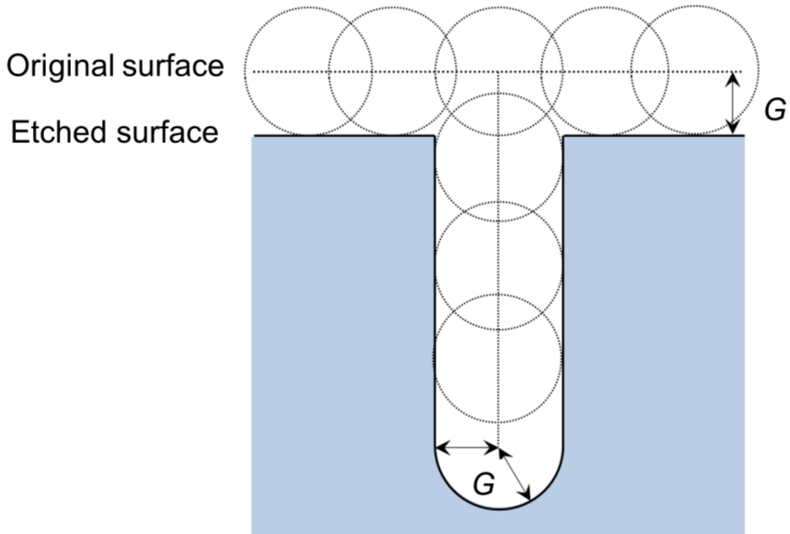

Fig. 2.7 Etch pit profile of fission fragment from ^{252}Cf.

The fission fragment, which is consisted by a few MeV heavy ions such as Xe ion, can irradiate by using ^{252}Cf spontaneous fission source. Such heavy ions create large damage which correspond to the etch pits with the sensitivities more than 100, because of the large stopping power in CR-39. The damaged regions are etched instantly, i.e. track etching process is finished very quickly, and then the etching process was occupied by bulk etching speed. Therefore, the etch pit radius and the thickness of layer removed will became the same as shown in Fig. 2.7.

2.2 ZnS(Ag) fluorescent screen

The ZnS(Ag) fluorescent screen with the thickness of several-tens micrometer has been developed for single shot diagnosis of laser-driven ion beam. In order to diminish the noise signals from the contaminants such as laser-accelerated electrons and X-rays, thickness of the fluorescent screen has been optimized based on the Bethe-Bloch equation. For the fluorescence material, the silver doped zinc sulfide, ZnS(Ag), has been employed because of the higher luminescence and longer decay constant (200 ns) than plastic scintillator [37]. The response of developed fluorescent screen was characterized by high energy protons from the conventional accelerator in Hyogo Ion Beam Medical Center, HIBMC.

2.2.1 The Bethe-Bloch equation for ions and electrons

Generally, it is necessary to consider the signal to noise (S/N) ratio of the ion signals to the background signals, such as X-rays and electrons when using the scintillator as an ion detector. In the case of laser-driven ion acceleration, the background noises are mainly generated by the electrons that collide with the fluorescence materials, because the energy deposited on the scintillator of an X-ray (~tens keV) is smaller than that of an electron (~tens MeV) by three orders of magnitude. It is necessary that a scintillator has small deposition energy from electron collision to improve the S/N ratio.

Bethe and Bloch developed the following equation for the energy loss of an electron that has collided with a material:

$$-\frac{dE_{elec}}{dx_{elec}} = \frac{2\pi}{m_e c^2}\cdot\frac{n}{\beta_e^2}\cdot\left(\frac{e^2}{4\pi\varepsilon_0}\right)^2\cdot\left[\begin{array}{l}\ln\left(\frac{m_e c^2 \beta_e^2 E_{elec}}{2I^2\cdot\left(1-\beta_e^2\right)}\right)-\left(2\sqrt{1-\beta_e^2}-1+\beta_e^2\right)\ln 2\\ +\left(1-\beta_e^2\right)+\frac{1}{8}\left(1-\sqrt{1-\beta_e^2}\right)^2-\sigma\end{array}\right], \tag{2.20}$$

where, E_{elec} is energy of the electron, x_{elec} is the distance travelled by the electron, β_e is the velocity of the electron which is normalized with the light speed, e is elementary charge of the electron, m_e is electron rest mass, n is electron density of the material, I is mean excitation potential of the material, ε_0 is vacuum permittivity, and σ is density correction.

The electron density of the material can be calculated by,

$$n = \frac{N_A\cdot Z\cdot\rho}{A\cdot M_u}, \tag{2.21}$$

where ρ is the density of the material, Z and A are the atomic number and mass number, respectively, N_A is Avogadro number, and M_u is the molar mass constant. Then, the Bethe-Bloch equation can be substituted as

$$-\frac{dE_{elec}}{dx_{elec}} = f\left(\beta_{elec}, I\right), \tag{2.22}$$

where $f(\beta_{elec}, I)$ is function of the electron velocity and the mean excitation potential.

On the other hand, the Bethe-Bloch equation for the energy loss of an ion is given by

$$-\frac{dE_{ion}}{dx_{ion}} = \frac{2\pi}{m_e c^2} \cdot \frac{n}{\beta_e^2} \cdot \left(\frac{e^2}{4\pi\varepsilon_0}\right)^2 \cdot \left[\ln\left(\frac{2m_e c^2 \beta_i^2}{I \cdot (1-\beta_i^2)}\right) - \beta_i^2 - \frac{\sigma}{2}\right], \tag{2.23}$$

where E_{ion}, x_{ion}, and β_i are physical quantities similar to those used in Eq. 2.20, and z is the particle charge. And then, the energy loss of an ion can be described as follows:

$$-\frac{dE_{ion}}{dx_{ion}} = z^2 f(\beta_i, I). \tag{2.24}$$

Therefore, the energy loss of an ion in a material depends on the charge, velocity of the particle, and means excitation potential.

In order to increase the S/N ratio of the fluorescent screen, the scintillator should be optimized to the energy loss (deposited energy on the scintillator) of the ion and electron. For the optimization, it is necessary to calculate the deposited energy ratio of the ion to the electron.

By integrating the dE/dx equation, the deposited energy is obtained as follows:

$$\Delta E = \int_0^x \left(\frac{dE}{dx}\right) dx. \tag{2.25}$$

Substituting Eq. 2.25 into Eqs. 2.24 and 2.22, the following equation is obtained:

$$S/N_{ratio} = \Delta E_i / \Delta E_e = \frac{\int_0^x \left(\frac{dE_{ion}}{dx_{ion}}\right) dx_{ion}}{\int_0^x \left(\frac{dE_{elec}}{dx_{elec}}\right) dx_{elec}} = \frac{z^2 \int_0^x f(\beta_i, I) dx_{ion}}{\int_0^x f(\beta_e, I) dx_{elec}}. \tag{2.26}$$

In Eq. 2.26, the electron speed is mostly assumed to be the speed of light ($\beta_e \approx 1.0$), and if I is fixed as I_{scinti} with the scintillator, the energy deposited on the scintillator can be calculated as

$$\int_0^x f(\beta_e, I_{scinti}) dx_{elec} = Constant_{scinti} \cdot x. \tag{2.27}$$

Finally, the equation for the deposited energy ratio in the scintillator is

$$S/N_{ratio}(x, I_{scinti}, z, \beta_i) \cong \frac{z^2 \int_0^x f(\beta_e, I_{scinti}) dx_{ion}}{Constant_{scinti} \cdot x}. \tag{2.28}$$

According to Eq. 2.28, the deposited energy ratio depends on the thickness of the scintillator: x, the scintillator material: I_{scinti}, the amount of ion charge: z, and the energy of the ion: β_i. Therefore, to optimize a fluorescent screen as the laser-accelerated ion detector, z should be larger and x should be smaller.

2.2.2 Optimization of the fluorescent screen

To use Eq. 2.28, the S/N ratio on the scintillator must be calculated analytically. On the other hand, the influence from secondary particles generated by nuclear reaction processes is not defined in detail in this equation. Accordingly, Monte Carlo particle transportation code PHITS (see section 2.3) was employed to calculate the deposited the energy for the fluorescent screen.

In the present study, the silver doped zinc sulfide, ZnS(Ag) [38], has been applied for the scintillation material. Thanks to the long decay constant, ZnS(Ag) scintillation can be easily obtained the image by using usual charged coupled device, CCD. Although, the ZnS(Ag) is a crystal powder with the 2 μm diameter, the design of fluorescent screen on PHITS calculation has been assumed as shown in Fig. 2.8 to use as ion detector practically.

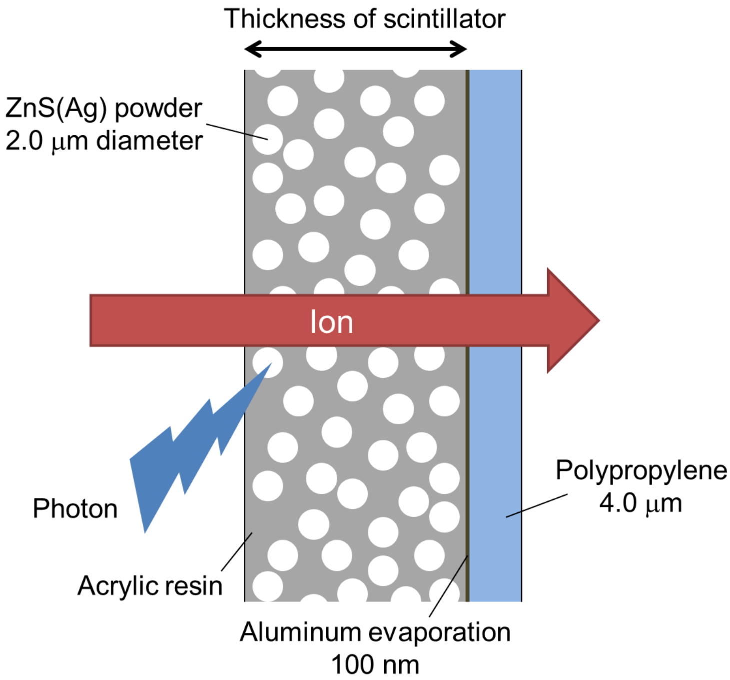

Fig. 2.8 Structure of the fluorescent screen. The ion deposits the energy on the ZnS(Ag) layer and generates photons corresponding to the energy.

Figure 2.8 shows the cross sectional view of the fluorescent screen. The ZnS(Ag) powder composed of particles with a radius of 2 μm and a density of 4.09 g/cm^3 is mixed with an acrylic resin and spread onto a 100 nm evaporated aluminum substrate that is adhered to a 4.0 μm polypropylene layer. The luminescence caused by the deposited energy of the ions is reflected by the evaporated aluminum side, which increase the amount of light.

Figure 2.9 shows the calculation result of deposited energy ratio on the ZnS(Ag) scintillator of a proton (a) and C^{6+} (b) to an electron as a function of energy.

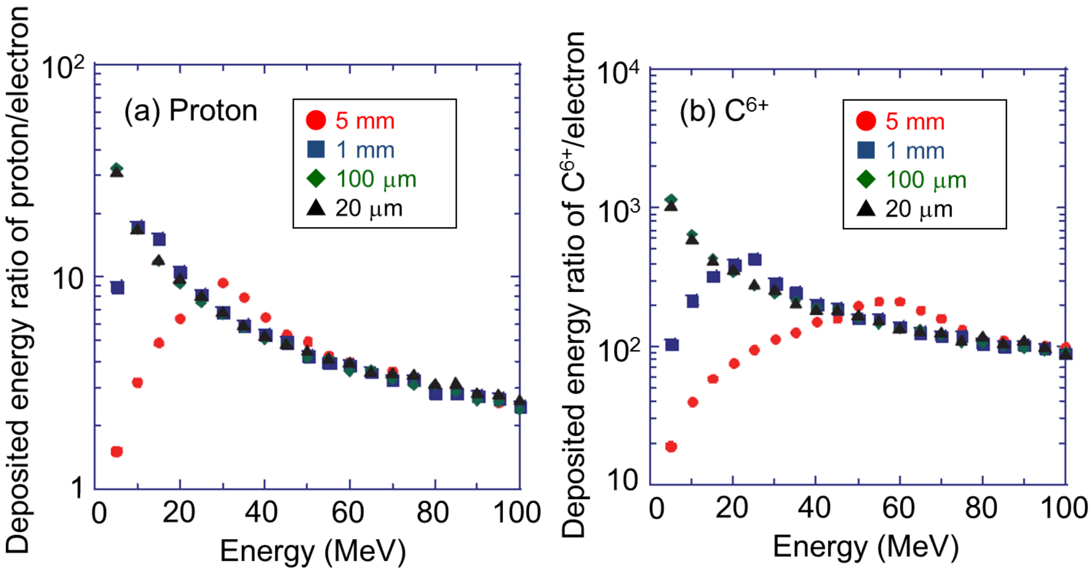

Fig. 2.9 Calculation result of the deposited energy ratio of an ion to an single electron on a ZnS(Ag) scintillator using the PHITS code for proton (a) and C^{6+} (b).

The deposited energy ratio of (a) a proton to an electron and (b) a C^{6+} to an electron on the Zns(Ag) scintillator are calculated at various thickness, such as 20 μm, 100 μm, 1 mm, and 5 mm. The deposited energy ratios of a proton and a carbon to an electron with the same kinetic energy are displayed at each point. Less than 10 MeV protons indicate the S/N ratio ~1 for a 5.0 mm thick scintillator. This result reflects the facts that increase of denominator in Eq. 2.28 because the deposited energy of the electron increases in proportion to the thickness of the scintillator. When compared the Figs. 9 (a) and (b), the S/N ratio of the carbon is higher than that of the proton. This trend is also apparent in Eq. 2.28 as the factor z^2.

From the result of PHITS calculation, a scintillator, which is thinner than 100 μm, is suitable for the protons detection. Therefore, the thickness of ZnS(Ag) and acrylic resin has been determined as 20 μm.

2.2.3 Calibration of the fluorescent screen

In order to clarify the response characteristics for high energy protons, the calibration experiment of the fluorescent screen has been carried out by using the conventional accelerator in Hyogo Ion Beam Medical Center, HIBMC.

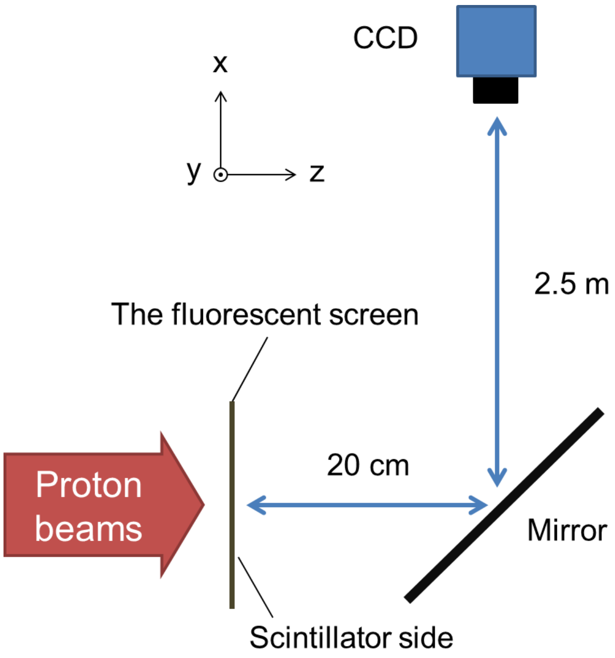

Fig. 2.10 The schematic top view of the response characterization experiment for the developed fluorescent screen.

Figure 2.10 shows the schematic top view of the experimental set up. The proton beams from synchrotron were delivered to the horizontal irradiation port, and then irradiated to the fluorescent screen which is installed perpendicular to the beam traveling direction. The luminescence was reflected to the 90 degree to the beam direction and the image was observed by CCD for each shot, because the CCD sensor can be easily damaged by ionizing radiation.

Firstly, the response characterization for the number of incident ions was carried out. In this characterization, 80 MeV protons were irradiated. Figure 2.11 shows the luminescence images obtained by CCD (a) and spatial intensity distributions on the fluorescent screen at the various number of incident ions (b).

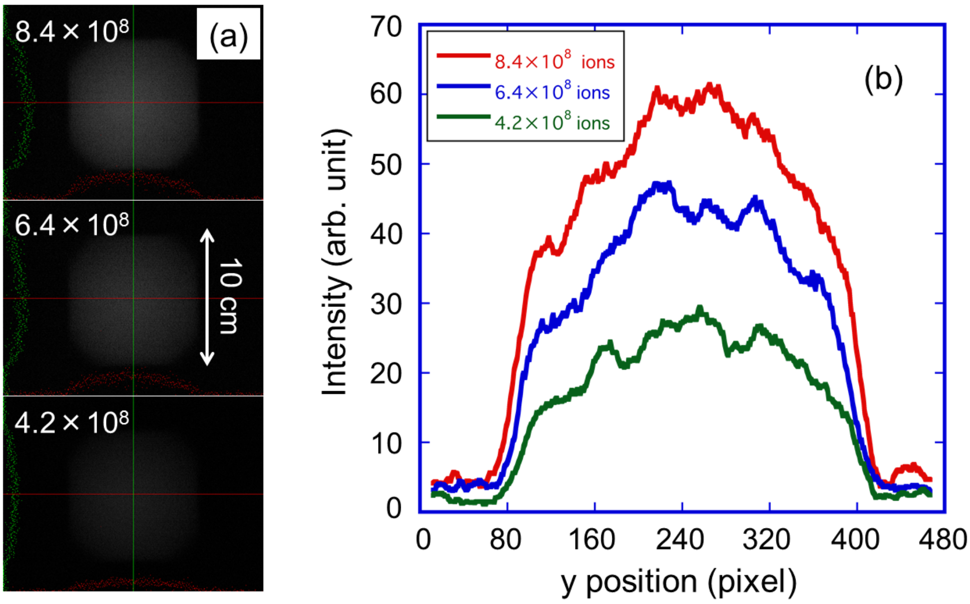

Fig. 2.11 The luminescence images of the fluorescent screen (a) and the spatial intensity distributions for y position (b).

From the result of Figure 2.11 (b), the spatial distributions of a proton beam was clearly obtained by the luminescent screen. And the brighter luminescence has been obtained with increasing the number of incident ions.

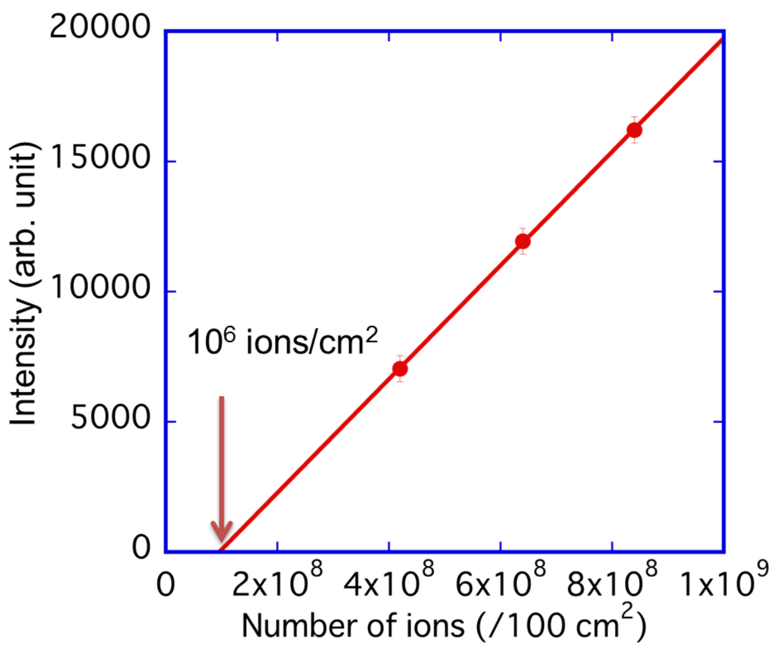

Fig. 2.12 The response curve of the fluorescent screen as a function of the number of incident ions.

Figure 2.12 shows the intensity calibration curve as a function of the number of incident ions. This trend line was obtained by plotted points which are evaluated values of each integrated area below the spatial distribution curve. From the correlation between the number of incident ions and luminescence intensity, the developed fluorescent screen has the good linearity for the number of incident ions. The x-intercept of the calibration curve, indicated by arrow in Fig. 2.12, which is 1×10^6 ions/cm^2, is correspond to the minimum detection intensity of the CCD device, 0.4 lx. Therefore, this system can diagnose from 1×10^6 ions/cm^2 to the 80 MeV protons.

Secondly, the response characterization for the energy of incident ions was carried out. In this characterization, the fluenece of protons were fixed at 8×10^4 ions/cm^2 and the energies were varied from 5 MeV to 230 MeV by synchrotron and energy filters. Figure 2.13 shows the intensity calibration curve as a function of the stopping power in water.

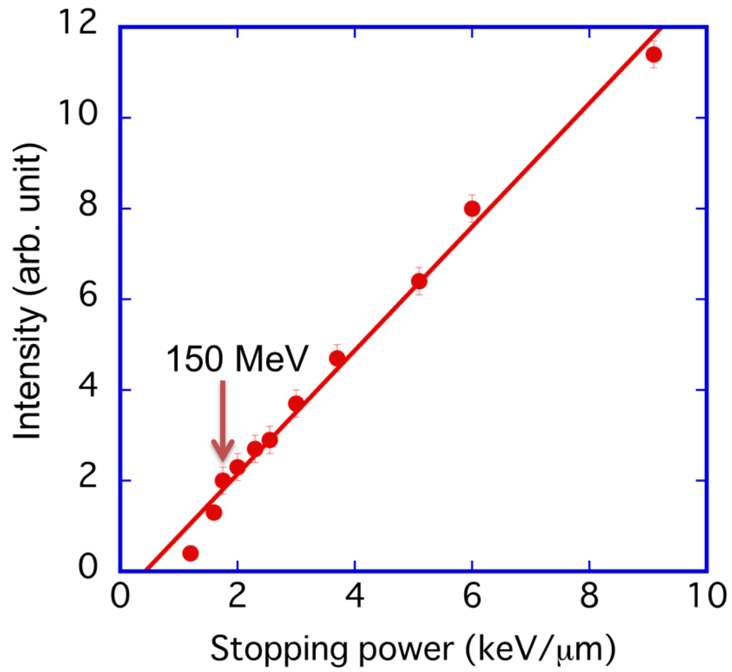

Fig. 2.13 The response curve of the fluorescent screen as a function of the stopping power of incident ions.

The arrow in Fig. 2.13 indicates protons with the energy of 150 MeV. From this trend line, the linearity has been confirmed from 5 to 150 MeV. More than 150 MeV protons cannot create the enough luminescence for the CCD because of the low deposited energy. Therefore, this system can apply for the diagnosis of proton beams from 5 MeV to 150 MeV with good linearity.

2.3 Calculation code for particle transportation

2.3.1 Particle and heavy ion transportation code, PHITS

A general-purpose Monte Carlo particle and heavy ion transport code system (PHITS) [39] that is based on various quantum dynamics models and evaluated nuclear data libraries for simulating three-dimensional nucleus-nucleus interactions was used. From the PHITS version 2.52, the evaluated cross sections in the giant resonance region for photo-nuclear reaction have been included. The PHITS software can predict the various scattering phenomena and the secondary particles from quantum reaction processes in the experimental configuration.

In this study, the precise behaviors of the laser-accelerated particles were evaluated in the experimental setups which were reconstructed on PHITS code. In order to increase the reliability of the ion detectors, the secondary particles from the result of nuclear reactions were also calculated (section 4.2.2.3 and 5.1).

Additionally, PHITS code has been applied to the development of the fluorescent screen to optimize the S/N ratio (section 2.2.2). The design of the ion detector system, which is diminished the photo-neutron fluxes, has also been carried out using PHITS code (section 6.2).

2.3.2 Three-dimensional electro-magnetic field analysis software AMaze

Three-dimensional electro-magnetic field analysis software package AMaze [40] include 4 programs the names of MetaMesh, Magnum, HiPhi, and OmniTrak. MetaMesh can create the three dimensional mesh of the input experimental configuration. Magnum and HiPhi calculate the magnetic field and electric field, respectively, by the finite element method using the mesh which is created by MetaMesh. Then, the charged particles trajectories in the experimental configuration have been calculated by the OmniTrak. Therefore, the precise experimental configuration can be designed by using AMaze.

Compared with the PHITS code, AMaze can reconstruct the magnetic field and electric field almost as same as the measured fields (see 3.3.2.1). So the trajectories of charged particles which pass through the magnetic field and electric field are more reliable than PHITS code in details. However, the particle will be stopped when it hit the materials, because AMaze has no models and libraries of nuclear reactions. Therefore, the combination of PHITS code and AMaze can be a powerful calculation tool for the design of the experimental Configuration.

3.1 Outline of the laser-driven ion acceleration experiments using solid targets

In this section, the laser-driven ion acceleration experiment using thin foil target conducted with the J-KAREN laser at JAEA-KPSI has been explained. Figure 3.1 shows the schematic of the experimental setup in focusing chamber.

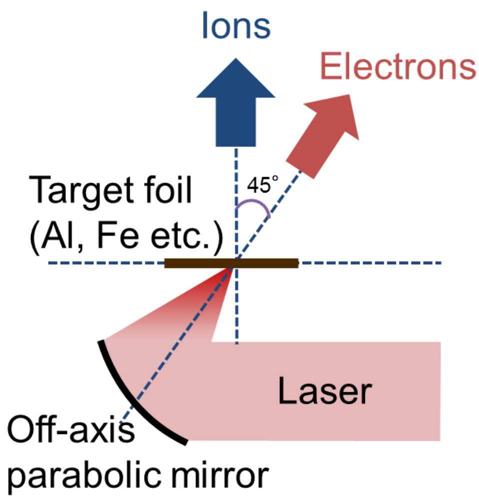

Fig. 3.1 A scheme of the laser-driven ion acceleration experiment with target normal Sheath acceleration mechanism.

A J-KAREN laser pulse comes from the right side of the plane and focused on a target foil with 45 degree by using an off-axis parabolic mirror. When an intense laser pulse focused on thin foil target, a laser field-driven force accelerates many electrons to relativistic velocity, and also some of these electrons pass through the thin target and generate a strong electrostatic accelerating field exceeding 1 MV/mm. It is achieved that the laser-accelerated proton energies to several MeV. This acceleration mechanism is called Target Normal Sheath Acceleration, TNSA [12]. With this mechanism, ions with high Z/m ratio are preferentially accelerated, and thus protons of hydrocarbons and water on the surface are accelerated most effectively. Recently, the energy of laser-accelerated protons has increased that the energy of laser-accelerated proton more than several-tens MeV as increasing the intensity of laser [6].

Here, notice that the traveling direction of laser-accelerated ions and the electrons with TNSA mechanism. The ions are accelerated to the target normal direction, on the other hand, the electrons are accelerated to the same direction of the laser-axis. The ion detector, set at the target normal direction, is less influenced by the contaminants such as laser-accelerated electrons and secondary particles from high energy electrons. Therefore, the on-line detector such as plastic scintillator can relatively easy to apply as ion detector for TNSA experiments. For example, time-of-flight, TOF, method using plastic scintillator has been succeeded to detect a few MeV protons [20].And also the on-line Thomson parabola, TP, systems were developed using Micro Channel Plate, MCP, with phosphor screen [21]. Both techniques can obtain the energy spectrum of laser-accelerated ions shot by shot. Especially, Thomson parabola could obtain high accuracy of charge resolution, but MCP with phosphor screen detector loses the detection efficiency as increasing the particle energy. And also TOF causes gradual loss of accuracy of energy resolution of high energy component as increasing the particle energy.

Accordingly, stacked CR-39 detector is one of the candidate detector to obtain the maximum energy of the laser-accelerated particles with more detailed measurement. And also the developed fluorescent screen is also the candidate detector to obtain the two-dimensional on-line imaging such as detection part of TP system.

3.2 A high energy component of laser-accelerated protons from thin foil target detected by stacked CR-39

As a frontier experiment, stacking method of track detectors has been applied to diagnose the spatial distribution and ion energy roughly in the field of laser-driven particle acceleration. Unfortunately, it have not been carried out the precise analyses for etch pits including etch pit growth behavior, therefore, it is fail to perform full potential of CR-39.

In the present study, it has been demonstrated that the precise measurement of laser-accelerated protons with CR-39 stacked detector, which reach full ability of CR-39. By means of multi-step etching technique, the determination of maximum energy of protons was performed with higher energy resolution than the past research.

3.2.1. Laser-driven proton acceleration experiment

In the present study, the J-KAREN laser pulses of 8 J are delivered to the experimental chamber. The pulse duration of the laser is 40 fs in full width at half maximum (FWHM). In this experiment, polyimide film with 7.5 μm thickness was used for the target, which positioned at the laser focus.

Figure 3.2 shows a cross sectional view of the 70×70 mm^2 wide ion detector unit used in the present experiment, which consists of a 13 μm thick Al foil filter, 105 μm thick radiochromic film (GAFCHROMIC HD-810), and 8th layer stacked CR-39 (HAZLAS TD-1, Fukuvi Chemical Industry) with a nominal thickness of 0.9 mm. The Al foil filter was placed in front of this track detector to protect it from damage induced by the transmitted portion of the main laser pulse and also low energy particles below 1 MeV/n caused by coulomb explosion. In the present study, laser-driven particle acceleration experiment has been carried out in evacuated chamber below 10^{-3} Pa. The storage times in vacuum before and after shot are limited less than 15 min. Therefore, it is no need to consider that the degradation of sensitivity for CR-39 detectors by the vacuum effect [41].

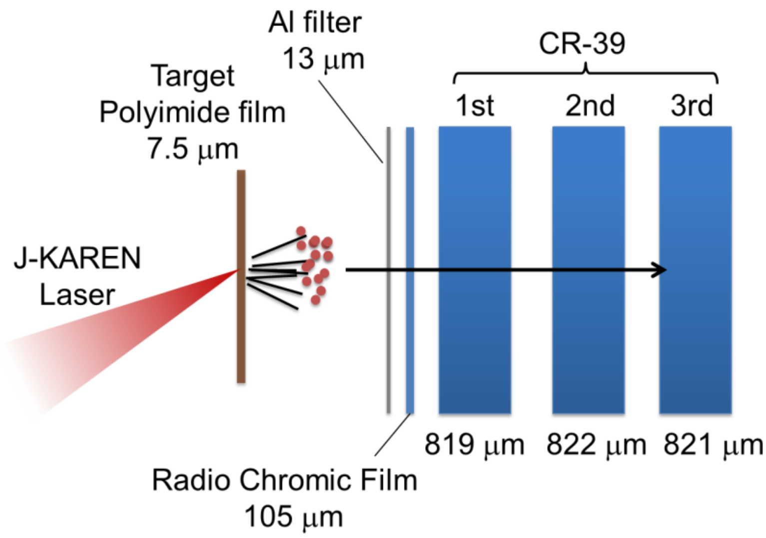

Fig. 3.2 Cross sectional view of the laser-driven particle acceleration experimental set up with polyimide film target.

After irradiation, CR-39 samples were chemically etched in a stirred 6 M-KOH solution kept at 70℃ for total 19 h using the multi-step etching technique [42]. Surface observations on the etched samples were made under an optical microscope (BX60-F3, OLYMPUS), which is operated on PC with an image processor (WinROOF Ver 5.04, MITANI Corporation).

3.2.2. Result and discussion

Figure 3.3 shows the optical images of the CR-39 detectors, Fig. 3.3(a) is indicating the first layer, Fig. 3.3(b) is the second layer and Fig. 3.3(c) is the third layer, which obtained by optical scanner after the 1.5 h chemical etching process. As shown in these photographs, one can identify three different regions in brightness. In the brightest area in Fig. 3.3(a) and (b), the CR-39 layers have etch pits on both front and rear surfaces. In the gray areas with medium brightness the layers have etch pits only on the front surface. In the darkest area in Fig. 3.3(b) and (c), there is no etch pit except from the scattered ions from experimental system. We could observe the etch pits from first layer to front surface of third layer, i.e., incident protons into the third layer of CR-39 are high energy component including maximum energy proton in the laser-accelerated protons. And also, these pictures indicate that the low energy component which generated by coulomb explosion has very large divergence and the high energy component is good directional beam.

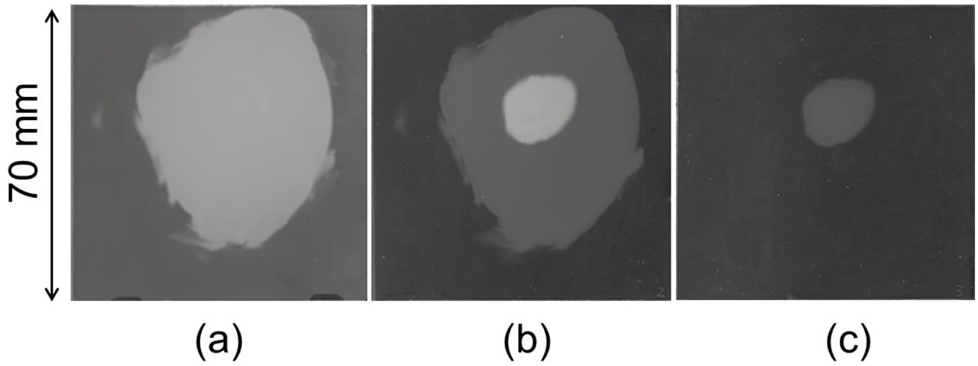

Fig. 3.3 Spatial distribution of laser-accelerated proton beam from view of beam axis appeared on CR-39 detectors. The brightest areas have the etch pits on the both rear and front surface, the gray areas with medium brightness have etch pits only on the front surface and the darkest area has no etch pit except from scattered particles.

The numbers of etch pit on the third layer are 10^7 ions/cm^2 at the beam center and 10^5 ions/cm^2 at beam halo. Note that the maximum observable fluence on CR-39 would be limited below 10^5 ions/cm^2 under the optical microscope, because of the etch pits overlapping. Therefore, the precise measurement of etch pit radius could have not been carried out at the beam center, then the analysis has been carried out at beam halo. About 70 etch pits have been observed at the beam halo with multi-step etching technique, in which the etching and the microscopic observations are repeated every 30 min with chemical etching until all etch pits were round out, in other words etch pit in spherical phase.

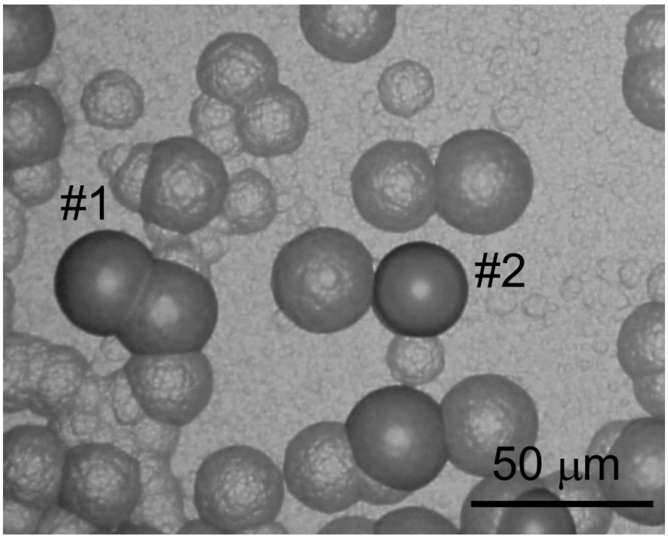

Fig. 3.4 Optical microscope image of etch pits on front surface of third layer, chemical etched 19 h.

Fig. 3.4 shows an optical microscopic image for the etched CR-39 detector in the third layer. The total bulk etch is 55 μm. In the present study, the analysis focused on the numbered etch pits as #1 and #2, and follow their growth behavior, which have relatively clear contrast at the boundaries compared to the others. As described in the followings, all etch pits in this figure are in spherical phase, where the pit wall is totally formed by the bulk etching starting from the track end-points. Evolution behavior of etch pits has been investigated well from the viewpoint of etch pit geometry [31]. As long as the bulk etch rate is constant, the growth rate of squared pit radius is proportional to the bulk etch G, i.e., the thickness of layer removed, in the spherical phase. Based on the etch pit growth curve, plotting the squared radius against the bulk etch, the projected range R_0 can be obtained by using the next relation,

$$R_0 = G + \frac{1}{4}\left(\frac{dr^2}{dG}\right) - \frac{r^2}{\left(\frac{dr^2}{dG}\right)}. \tag{3.1}$$

where r is etch pit radius and dr^2/dG is slope of the squared radius against the bulk etch. Fromm et al. have derived the identical relationship with different formulation and demonstrated its validity for protons and alpha particles with various incident energies [43].

Figure 3.5 shows etch pit growth curves for #1 and #2, plotting each radius as a function of the thickness of layer removed. As shown in this figure, the slopes for the curves increase gradually up to the points indicated by each arrow. These are caused by the depth dependence of the track etch rate around the Bragg peaks. In the deeper etching after each indication by the arrows, the curves begin to saturate. These are results of the staring of the spherical phase.

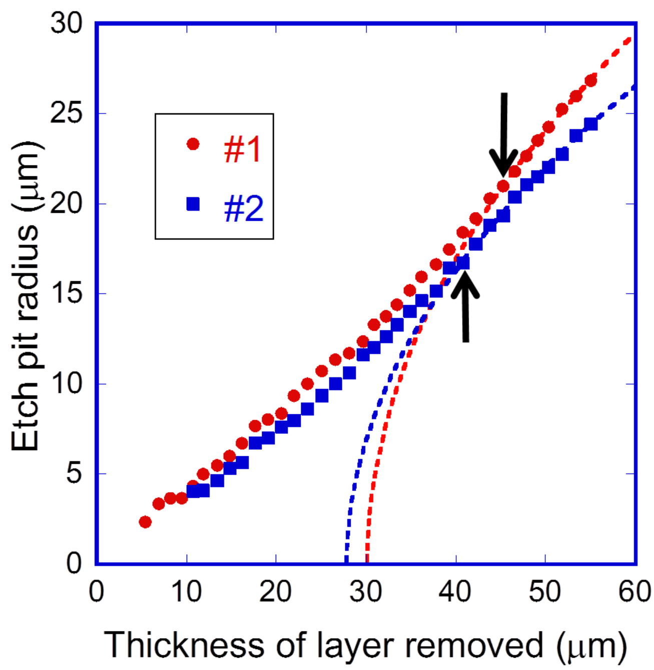

Fig. 3.5. Etch pit growth curve with multi-step etching, plotting radius of numbered etch pit in Fig. 3.4. The arrows indicate the starting point of the spherical phase. The dotted lines correspond to the fitting lines in Fig. 3.6.

Fig. 3.6 indicates the etch pit evolution behavior plotting squared radius. Both etch pit growth curves have straight sections in the deeper etching regions after each arrow. It is obvious that etch pits #1 and #2 in Fig. 3.4 are in spherical phase from the present diagram. The slope of the squared pit radius against the bulk etch was attained by the least squared fitting as shown in Fig. 3.6 with broken lines. The starting points of the spherical phase were selected as the fitted lines have larger correlation coefficient. From the attained slope of linear sections and etch pit radii at the bulk etch of 55 μm, the projected range has been calculated in third layer of CR-39 using Eq. 3.1.

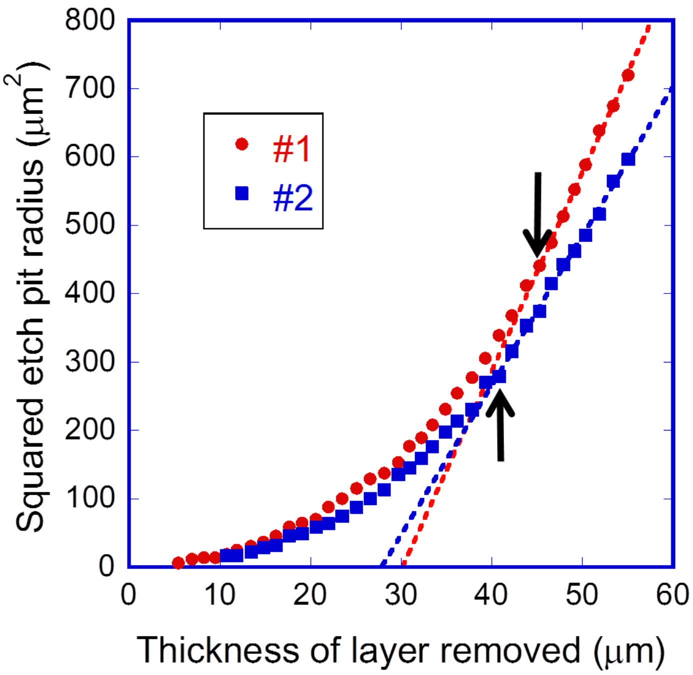

Fig. 3.6. Etch pit growth curve with multi-step etching, plotting squared radius of numbered etch pit in Fig. 3.4. The arrows indicate the starting point of the spherical phase. These straight dotted lines indicated the fitting curve of linear section, which parts are equal to the etch pits in spherical phase.

The evaluated ranges in the third layer of CR-39 are 63.23 μm and 61.62 μm for etch pits #1 and #2, respectively. Then, the proton energy has been estimated from total range in detector unit with SRIM code [44]. Note that the thickness of CR-39 detectors has variability, nominal thickness is 0.9 mm, actual thicknesses which measured by micrometer are 819 μm and 822 μm for the first and the second layer, respectively. For example, the proton, created etch pit #1, passed through the first and second layers and reached third layer, i.e., it passed through 1704.23 μm in CR-39. Figure 3.7 shows the relation between incident energy and range of proton in CR-39.

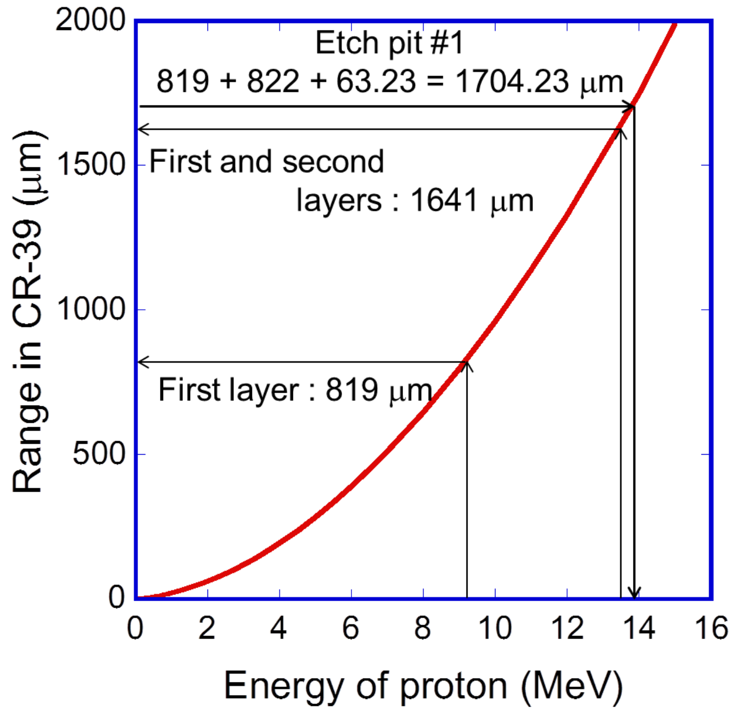

Fig. 3.7. Relation between incident energy and range of proton in CR-39 calculated by SRIM code.

As shown in Fig. 3.7, the proton with an incident energy of 9.14 MeV will stop just on the rear surface of the first layer or on the front surface of the second layer. The other example tells us proton with 13.50 MeV will stop on the rear surface of the second layer or on the front surface of the third layer. Total range of proton which produced etch pit #1 is 1707.23 μm, simply adding the thickness of the first and second layers, and the evaluated proton range in the third layer. Using this diagram, the values of 13.75 MeV can be derived on the first layer as the incident energy of the considering proton. This proton had passed through the both Al foil and the radiochromic film before arriving at the CR-39 stack, as shown in Fig. 3.2. So the proton energy of 14.39±0.05 MeV can be derived as generated from the target, taking into account the energy reduction in these other materials. Similar analysis for etch pit #2 gives us proton energy of 14.37±0.05 MeV.

As an alternative method, it has been determined that the maximum energy of laser-accelerated protons by TOF method. The energy resolutions of ordinary TOF method are ΔE±1 MeV at the energy more than 10 MeV. Therefore, in the present study, it is first time to decide the maximum energy with uncertainty ΔE=0.1 MeV in the field of laser-driven particle acceleration experiment.

3.2.3. Conclusion

In the present study, the precise measurement of laser-accelerated protons with CR-39 stacked detector unit has been demonstrated, which reach full ability of CR-39. Thanks to the stacking, the proton energy higher than 10 MeV can be measured, which penetrate a single CR-39 sheet with the thickness of 0.9 mm. By means of multi-step etching technique, it has been determined that the maximum energy of protons was 14.39±0.05 MeV in this laser-driven proton acceleration experiment. This method, using stacked CR-39 detector unit, allows us to measure the energies with uncertainty $\Delta E=0.1$ MeV which is ten times higher in resolution compared to TOF ordinary measurement in the field of laser-driven particle acceleration experiment.

3.3 On-Line Thomson Parabola Spectrometer System for Laser-Accelerated ions

3.3.1 Principle of Thomson parabola spectrometer

The principle of Thomson parabola spectrometer is shown in Fig. 3.8. The system has been applied electric field and magnetic field to parallel direction. The accelerated ions were collimated with the pinhole.

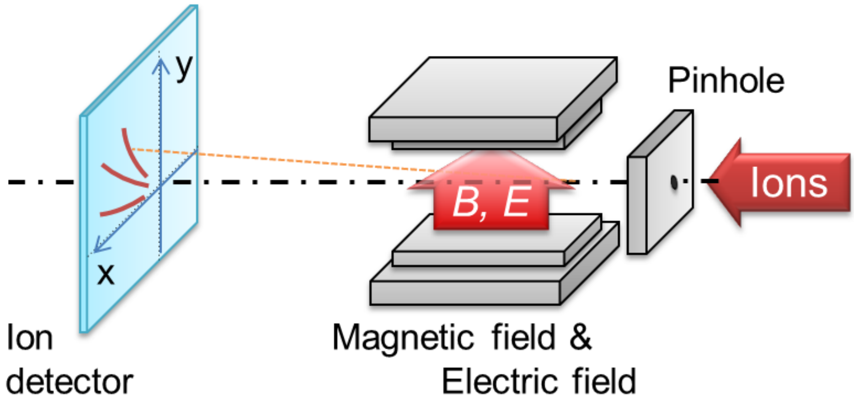

Fig. 3.8 Principle of Thomson parabola system.

The collimated ions were deflected to the y direction by the electric field depends on the charge state and the x direction by the magnetic field depends on the momentum. The deflection of the x and y axis can describe in SI unit as Eq. 3.2 and Eq. 3.3.

$$x = \frac{ZeEl}{mv^2}\left(\frac{l}{2}+L\right), \tag{3.2}$$

$$y = \frac{ZeBl}{mv^2}\left(\frac{l}{2}+L\right), \tag{3.3}$$

where Z is charge number, e is elementary charge, E is electric field, B is magnetic field, l is magnetic and electric field distance, L is distance from the magnetic and electric field end to the ion detector, m is mass of the particle, and v is the velocity.

Using these equations, the Eq. 3.4 can be obtained,

$$y = \frac{2E}{B^2l^2}\left(\frac{m}{Z}\right)x^2. \tag{3.4}$$

Where $2E/B^2l^2$ is defined by the design of equipment. Therefore, the ions of a fixed m/Z create a unique parabolic trajectory on the ion detector. The Thomson parabola system can be an efficient diagnostic system for laser-accelerated ions, because the multi-charged and wide-spread energy ions were generated in the laser-driven ion acceleration experiments.

3.3.2 Experimental Layout and Simulation of Particle Transport

3.3.2.1 Thomson parabola spectrometer with a long flat topped B-field

In order to achieve a high resolution of the charge-to-mass ratio and the kinetic energies of the ions, the Thomson Parabola (TP) spectrometer typically requires the strengthening of the peak B-field and E-field. If neodymium magnets and non-magnetic material (copper or aluminum) electrodes are used to obtain a strong magnetic field, the B-field distribution is a “non-flat topped shape” in the central part of the electrode, and has a bell-shaped distribution [45]. For a higher resolution, a magnetic field distribution that has a long flat portion is required. A magnetic material (in this case, iron) is used in the electrodes for obtaining “long-flat-topped distribution,” thus, the energies of the ions located on the detector can be analyzed with good accuracy.

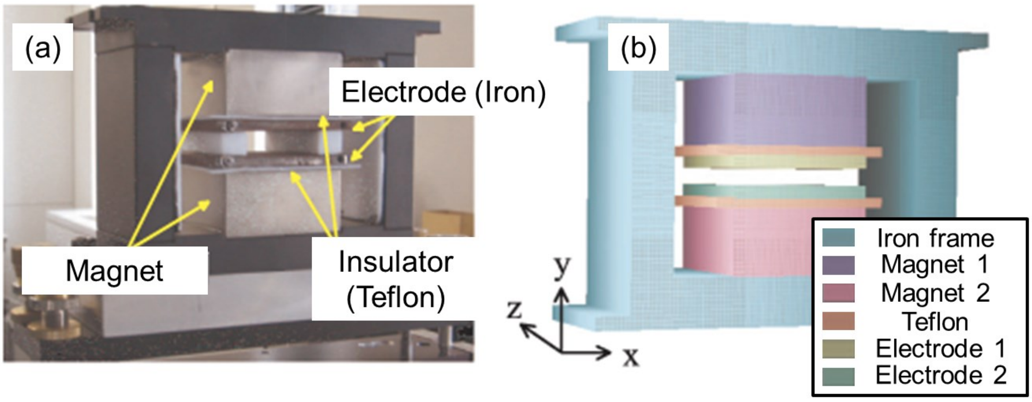

Fig. 3.9 (a) Photograph of the TP used for this study. A long-flat-topped B-field is created with a neodymium magnet and an iron electrode. (b) Geometry used in the AMaze software

Figure 3.9 (a) shows the TP spectrometer made with neodymium magnets that are 5 cm long in the z-axis direction. In order to predict the ion orbits with high accuracy, it is important to apply the B-field and E-field that are actually measured. The detailed 3D distributions of the B-field and E-field in the TP spectrometer, Fig. 3.9 (a), are calculated with the 3D Band E-field analysis software AMaze. Figure 3.9 (b) shows the input geometry which reconstructed on AMaze for calculating the 3D B-field and E-field. The calculated result for the B-field at (x, y) = (0, 0) in the Z direction is shown as the red line, and the measured magnetic field distribution is shown as blue dots in Fig. 3.10.

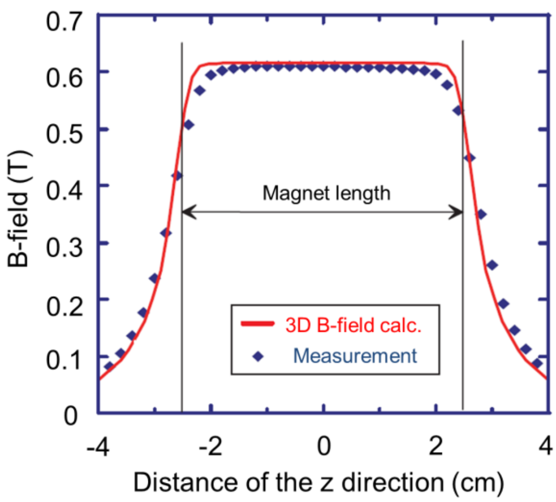

Fig. 3.10 Predicted magnetic field using the AMase software (line) and the measured value (dots). The length and width of the installed neodymium magnet are 5.0 cm.

Both distributions exhibit the shape of a dipole field with field strength of 0.6 T. The use of this long flat topped B-field increases the confidence in the analysis of the ion energy.

3.3.2.2 Simulation results of integrated depositions for the experimental layout

The ratio of the deposited energy of a single-ion event to a single electron event is shown in Fig. 2.9. In actual experiments, however, numerous electrons are produced in the laser-plasma interaction. While some electrons reach the fluorescent screen directly, some others are scattered against the chamber wall toward the fluorescent screen and increase the background signal. Others are converted to X-rays at the chamber walls and also increase the background level of the fluorescent screen. The integrated depositions caused by multiple electron events from the plasma are calculated. The characterization of the fluorescent screen for the on-line TP is executed for the experimental layout as shown in Fig. 3.11.

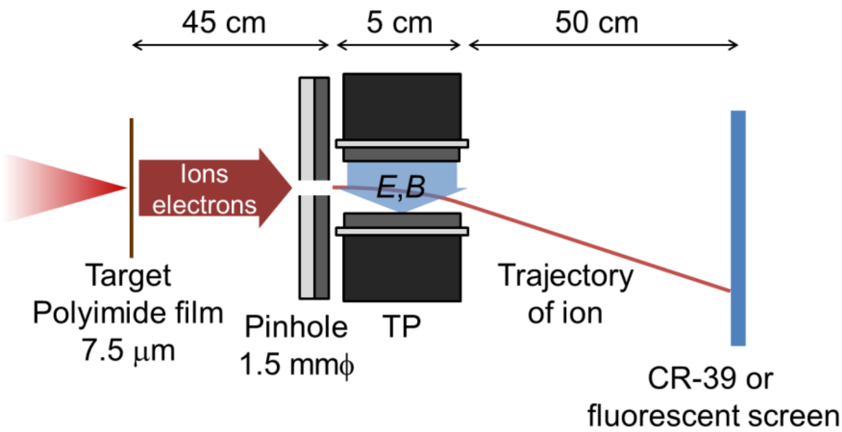

Fig. 3.11 Experimental layout for the characterization of the on-line TP. Distance between the laser irradiation point and the TP is 45 cm, and that between the TP and the detector location is 50 cm.

A 1.5 mm pinhole has been set in front of the TP spectrometer. The simulated result for the particle flux in the x-z plane is shown in Fig. 3.12. The trajectories of the electrons and protons in the energy band from 2.5 to 50 MeV are shown using a color scale in units of normalized flux (normalized by the total number of protons and electrons at the source). The electrons are bent by the B-field in the TP spectrometer, so that some electrons penetrate through the vacuum chamber wall and do not return to the system.

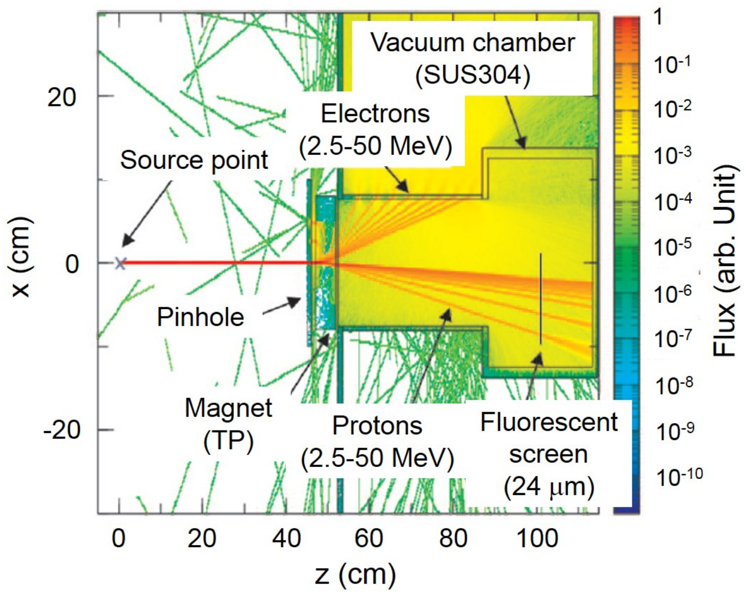

Fig. 3.12 Simulated results for the particle flux in the x-z plane orbit using the PHITS software for the experimental layout. The color scale indicates the simulated particle distribution. The fluorescent screen is installed at a distance of 100 cm from the source.

The results in Fig. 3.12 demonstrate that there is no positional dependence of the deposited energy on the electrons scattered from the chamber wall. The deposited energy ratio of the TP (integrated along the horizontal direction) on the fluorescent screen in the experimental layout is shown in Fig. 3.13.

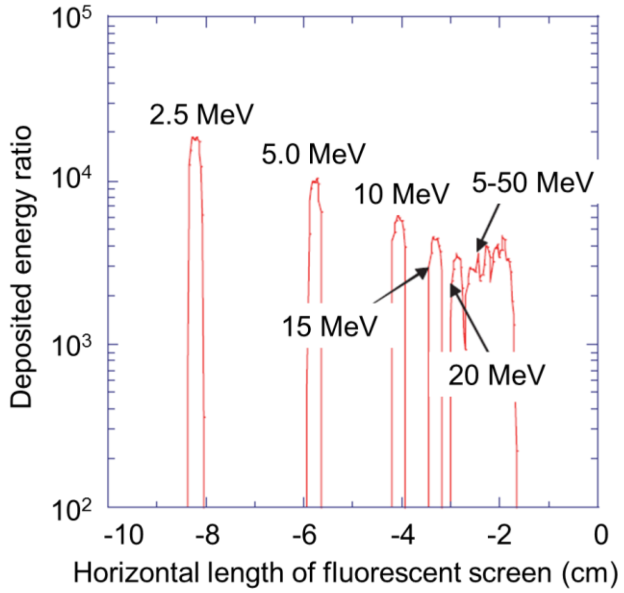

Fig. 3.13 Results of the simulation of the integrated proton to the electron deposited energy ratio on the fluorescent screen. The red line shows the deposited energy ratio of the proton to the average deposition of an electron on the fluorescent screen.

Because the number of events of the electrons that are detected on the fluorescent screen is less than that of the protons by three orders of magnitude, the deposited energy ratio of protons to electrons is improved to ~10^4.

3.3.3 Result of on-line imaging experiment

3.3.3.1 Calibration of number of ions with CR-39

To measure the absolute dose deposition of the ions on the fluorescent screen, a solid-state nuclear detector (CR-39) is installed instead of the fluorescent screen as is shown in Fig. 3.9. Ions are generated by the irradiation of a 7.0-μm-thick polyimide tape target with a laser pulse. The J-KAREN laser system at JAEA-KPSI provides P-polarized laser pulses at an incidence angle of 45.0° with a central wavelength of 800 nm, a duration of 60 fs (full width at half maximum), and an energy of 2.0 J. Peak irradiances of up to 4.0×10^{19} W/cm^2 are achieved on the target, and the intensity contrast ratio of the main pulse to that of the pre-pulse or pedestal component is set to 10^{11}. Figure 3.14 reveals the trajectories of the ions measured using the CR-39 detector following a 20 min etching process with 70℃, 6 M-KOH solution. The flux and energy calibration of the low-Z ions are performed using the results from the etched CR-39.

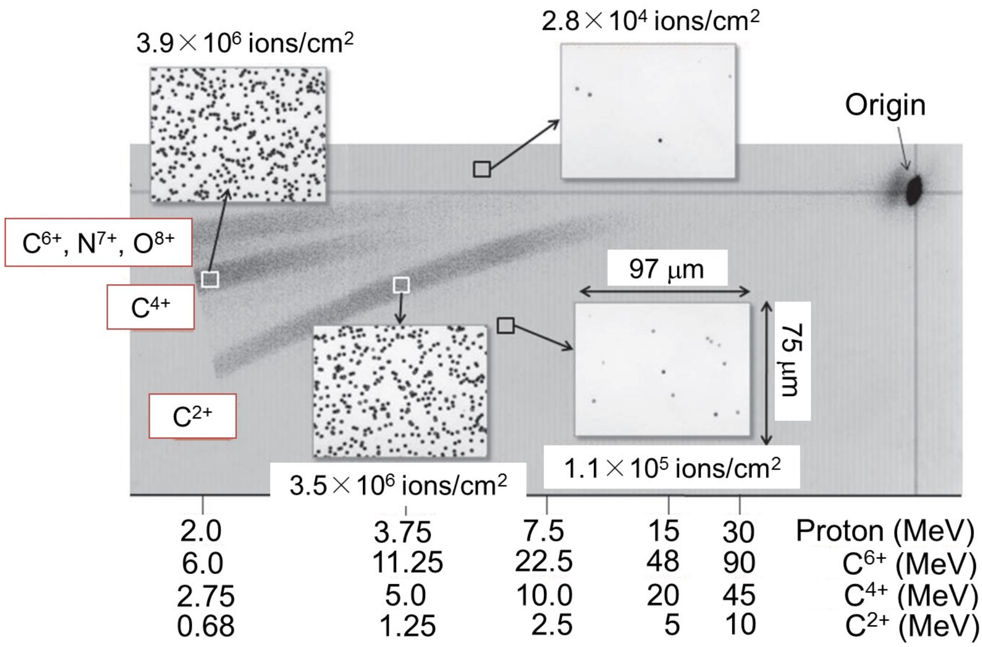

Fig. 3.14 Trajectories of the ions obtained with the Thomson parabola spectrometer using a CR-39 detector. The background is below 1.0×10^5 ions/cm^2.

In Fig. 3.14, the particles that make up the cloud of etch pits on the left side of the zero position are considered to be those having a neutral charge from the source (in the laser-produced plasma) and/or those that gained some amount of positive charge during the flight toward the detector. This figure shows many trajectories caused by carbons of various charged states. The flux of C^{2+} was measured to be 3.5×10^6 ions/cm^2 at 1.25 MeV, energy spread of 0.28 MeV (full width), and that of C^{4+} was measured to be 3.9×10^6 ions/cm^2 at 2.75 MeV, energy spread of 0.43 MeV (full width). The measurable energy range of a proton for an etching time of 20 min is less than 1 MeV, and a carbon for same etching time is less than 6 MeV. The pit of the proton trajectory cannot be observed by an optical microscope, because the size of pits is smaller or equal to 1.0 μm, which is the limit of the resolution of optical microscope for an etching time of 20 min. With the measured data, the total number of ions that arrive at the detector through the pinhole was determined to be ~3 × 10^7. Although the parabola trajectory made by the ions with the charge mass ratio is 1/2 mainly consist of carbon C^{6+} events on the CR-39 detector, a small amount of nitrogen N^{7+} and oxygen O^{8+} events are also observed.

3.3.3.2 Results of single-shot-imaging using the on-line

Figure 3.15 shows the measured ion trajectories using the fluorescent screen set at a position similar to that of the CR-39 detector in Fig. 3.9. For the observation of luminescence on the fluorescent screen, a standard charge-coupled device (CCD) is used. A CCD camera unit operated by an external trigger signal is placed approximately 1.0 m from the fluorescent screen surface. The specifications of the CCD were as follows: 8 bit, 0.8 megapixels, 0.4 lx minimum sensitivity. In this experiment, CCD has been used with an increased gain setting and a shutter speed of 0.001 s.

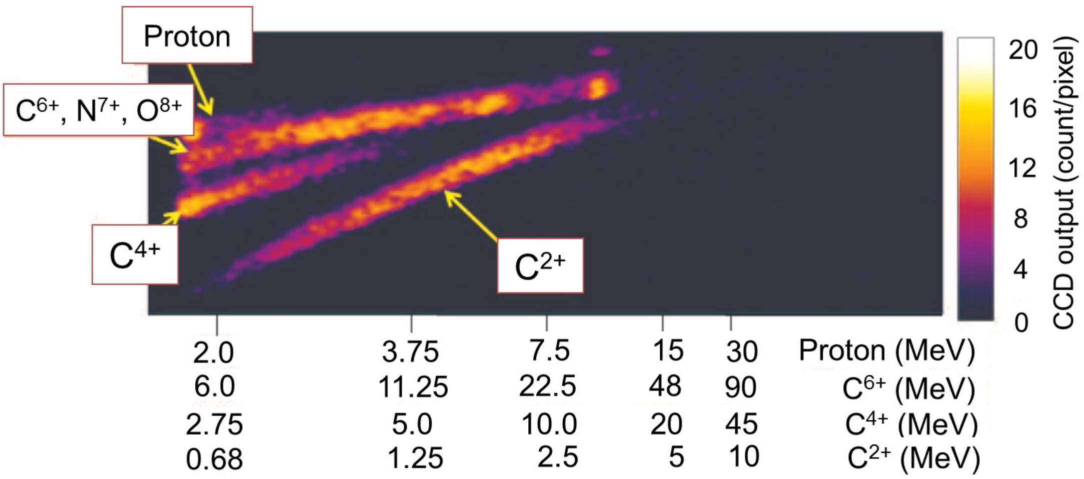

Fig. 3.15 Measured results using the on-line TP with the fluorescent screen.
The background noises are removed in these results.

The typical image of the luminescence of the fluorescent screen using a color scale that corresponds to the CCD output without background noises. Because the pinhole size is relatively large (1.5 mm in diameter), the trajectory of the protons with the energies more than ~4 MeV merges into these of other ions and cannot be resolved. In addition, the background level was relatively large because the shielding of the external light between the CCD and the fluorescent screen was insufficient.

3.3.4 Discussion

The resolution of the analysis is limited by that of the CCD and thus, the sensitivity of the CCD device is critical. To evaluate the sensitivity of the CCD, the integrated deposition on the fluorescent screen is simulated using the PHITS code. The energy distribution of the ions, which is obtained by the luminescence of the fluorescent screen that are used as input parameters for the simulations are shown in Fig. 3.16.

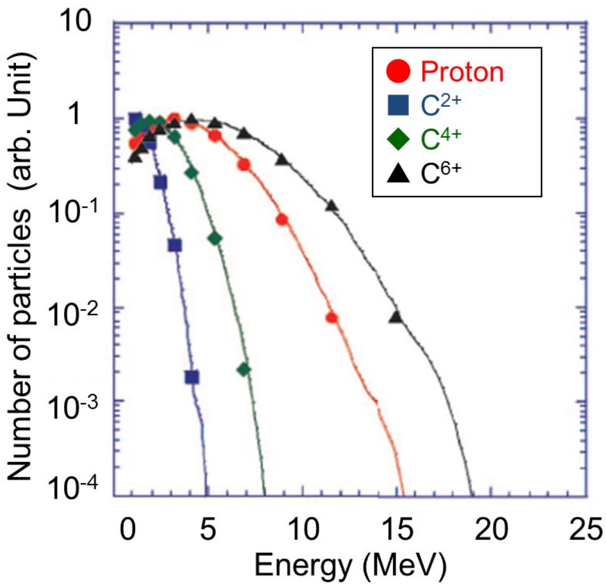

Fig. 3.16 Energy spectrum of the ions assumed by the measured data, and it is used as the input for the PHITS calculation.

For the generated C^{6+}, C^{4+}, C^{2+} carbons, and protons in the simulation, the assumed maximum energy of carbon is from 6 to 18 MeV which is depending on the charge state, and that of the proton is ~15 MeV. The measured peak energies of the number of carbon ions were obtained from the result of CR-39. Figure 3.17 shows the results of the simulation.

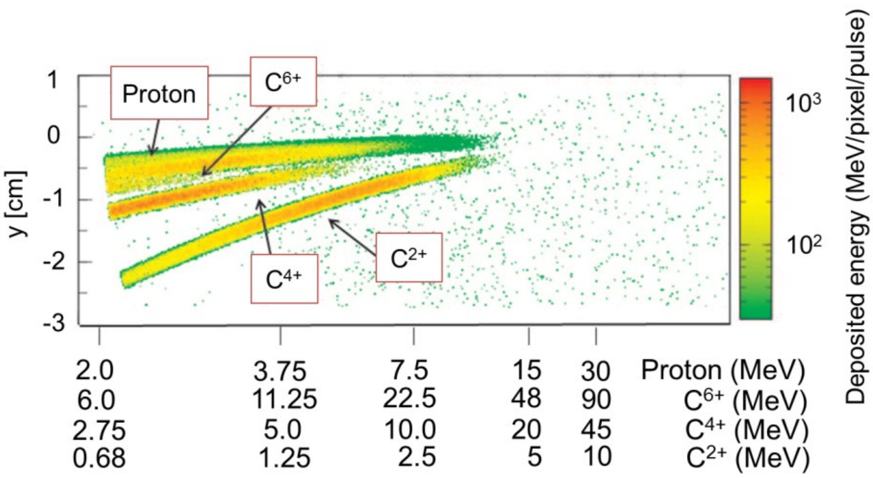

Fig. 3.17 The calculation result of the deposited energy per single laser shot. The areas from yellow to red can measure with CCD, 0.4 lx.

In this simulation, the total number of ions was set that arrive at the CR-39 surface is ~3×10^7. The color scale is in units of the deposited energy on the fluorescent screen per CCD pixel with single laser shot, MeV/pixel/pulse, in the range from 9.4×10^3 to 2.0×10^2 MeV/pixel/pulse. On the other hand, the threshold of the deposited energy for the observation is ~1.3×10^3 MeV/pixel/pulse which is correspond to the minimum sensitivity of the CCD, 0.4 lx [46]. The area indicated by the color between red and yellow on Fig. 3.17 can be diagnosed, because of only the area with the deposited energy higher than the threshold for the observation can be measured on the on-line system. The calculation result is consistent to the measured trajectories shown in Fig. 3.15.

Using this method, the system can design with a minimum sensitivity of CCD and the total number of ions that arrived at the fluorescent screen. Additionally, if an absolute calibration [47,48] is performed using a calibrated reference detector after designing of the on-line system and also the sensitivity of CCD is confirmed, the on-line diagnosis will be reliable. For example, using a sensitive CCD device such as an electron-multiplying CCD (minimum sensitivity is ~0.001 lx) in combination with TP, which can detect the luminescence of 100 MeV protons from the fluorescent screen, it will be possible to diagnose ions greater than 100 MeV/n in the future.

3.3.5 Conclusion

A thin fluorescent screen has been developed for an on-line TP spectrometer. Using the developed fluorescent screen, it has been developed that a new TP spectrometer system with the flat-top magnetic field. The first analysis of laser-accelerated ions by developed TP system at J-KAREN laser has been succeeded. The trajectories of the ions are measured by the fluorescent screen with a usual CCD camera. PHITS code, which is employed for the design of the fluorescent screen, can also calculate the trajectories. And calibration of the TP system has been carried out using CR-39. The result of calculation and CR-39 show the good agreement with the measured trajectories. Therefore, the various on-line TPs with fluorescent screen will be realized using this design technique.

Chapter 4 Laser-Driven Ion Acceleration Experiments using Cluster-Gas Targets

4.1 Outline of the laser-driven ion acceleration experiments using cluster-gas targets

In a field of laser-driven ion acceleration, development of target materials has been carried out in several research groups to increase the maximum energy of the ions and reveal the new ion acceleration mechanism. For example, carbon ions with the maximum energy of 15 MeV/n are accelerated by using a diamond like carbon foil with the thickness of 10 nm [49]. In the case of non-solid target, cluster-gas target attracts much attention in a field of laser-driven ion accelerations, because the energy of laser-accelerated ions are tenfold higher than the case of usual thin foil targets [8]. In this section, the outline of laser-driven ion accelerations using cluster-gas target have been introduced.

The density of plasma which is created by intense laser is important to the efficient laser-driven ion accelerations via the interaction of intense laser with matter. The case of thin foil targets, it can create the over-dense plasmas which reflect the laser. On the other hand, the gas targets create the under-dense plasmas which absorb a few percent of the laser energy. These plasma densities are not optimized for efficient ion acceleration. However, these targets are difficult to control their density. On the other hand, the cluster-gas target which is embedded atomic clusters in background gases can control the density between the solid targets and gas targets. Therefore, the cluster-gas target can obtain the sub-critical density plasmas, which can effectively absorb the energy of laser, and it has the potential to generate high energy ions.

Figure 4.1 shows one of the experimental setup for laser-driven ion acceleration using cluster-gas target in JAEA-KPSI.

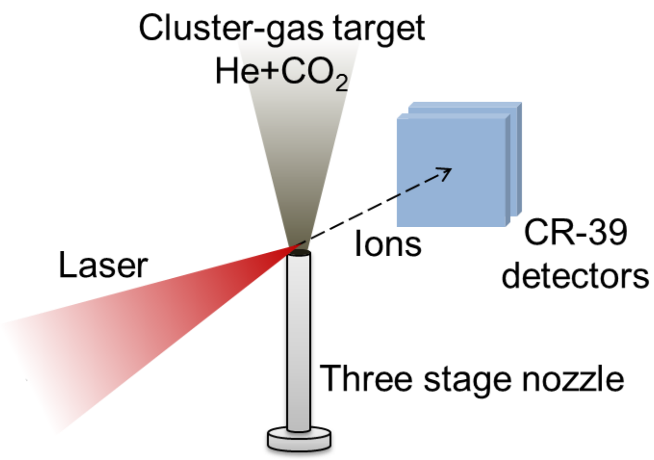

Fig. 4.1 Schematic view of a setup of laser-driven ion acceleration experiment using cluster-gas target.

The focusing intense laser irradiate to the cluster-gas target. The cluster-gas target is produced by a three stage conical nozzle which is connected by pulsed solenoid valve [50]. Using 6 MPa gas consisting 90% He and 10% CO_2, submicron size CO_2 clusters can produce in He gas with this system

[51]. The accelerated ions were detected by stacked CR-39.

In the case of cluster-gas target, the directions of laser-accelerated ions and electrons are different from the case of solid targets. Figure 4.2 shows the direction of generated ions and high energy electrons from cluster-gas target. As described in section 3.1, in the case of thin foil targets, the ions are traveled to the target normal direction and electrons were accelerated the same traveling direction of laser. On the other hand, the generated ions were classified two components in the case of cluster-gas target. One of the two is generated by coulomb explosion of the clusters. The maximum energy of ions which were produced by coulomb explosion is approximately 1 MeV/n. And also, the ions which were classified as coulomb explosion component are radiate in all directions as shown in Fig. 4.2.

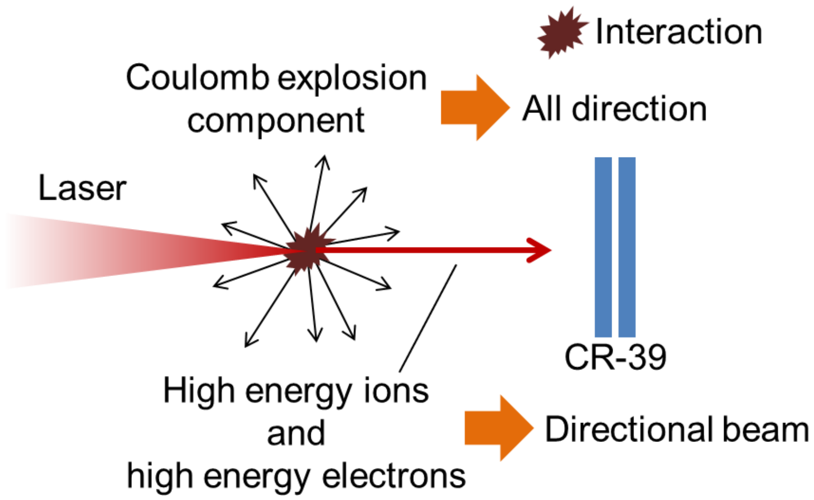

Fig. 4.2 The travelling direction of generated ions and high energy electrons from cluster-gas target.

The other component ions are accelerated by the vortex magnetic field which is produced by interaction of laser with cluster-gas target. Theoretically, the strong vortex magnetic field can produce high energy ions such as several-tens of MeV. These ions are accelerated to the same direction of laser travelling direction. And also, the accelerated electrons travel to the same direction, which can be crucial issue to diagnose the laser-accelerated ion beams.

In such case, ion detector system should be protected by the contaminants to reduce the noise signals. Accordingly, the ion beam diagnosis methods, which developed for thin foil target, are difficult to employ in the case of cluster-gas target. In the present study, the new simple diagnosis method has been developed for high energy ion beams using backscattered particles, which can use in a field contaminated with X-rays and high energy electrons.

4.2 The diagnosis method for high energy ion beams using backscattered particles for laser-driven ion acceleration experiments

In principle, however, it is impossible to detect ions with energies higher than the detection threshold limit of the CR-39 detector. In the case of BRYOTRAK, which is produced from the highly purified CR-39 monomer, it cannot detect He ions having energies of 40MeV or more. Therefore, a method to detect ions whose energies are far beyond the detection threshold limit of the CR-39 detector is required to further facilitate the laser ion acceleration experiments. Here, a new simple diagnosis method has been demonstrated for high energy ions to identify the ion beam profile and detect the presence of the high energy component beyond the detection threshold limit of the CR-39 detector.

4.2.1 Experimental Methods

The proof-of-principle experiment for the new method was carried out at Takasaki Ion Accelerators for Advanced Radiation Application (TIARA) facility in JAEA,[52]) which deliver a 5 nA $^{4}He^{2+}$ ion beam with an energy of 100 MeV (25 MeV/nucleon). As shown in Fig. 4.3 (a), the intensity distribution of the incident $^{4}He^{2+}$ ion beam had a $16\times3mm^2$ vertically long structure, recorded using an imaging plate (IP; Fuji Film BAS-SR) covered with a 6 μm thick Al foil protector, which blocks low-energy background particles in the vacuum beam line. The total fluence on the IP was adjusted to 2.0×10^9 ions/cm^2 by controlling the beam pulse duration using a beam chopper.

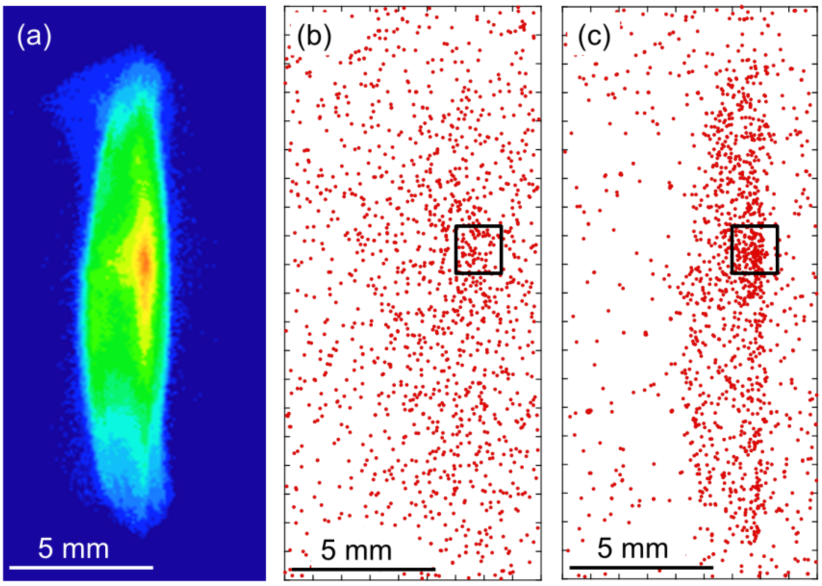

Fig. 4.3 (a) Intensity distribution of the incident 100MeV $^{4}He^{2+}$ ion beam recorded on the imaging plate (IP). Spatial distributions of etch pits on (b) the front and (c) rear surfaces of the CR-39.

Figure 4.4 shows a side view of the $70\times140mm^2$ ion detector unit used in the present experiment, which consists of a 6 μm thick Al foil protector, a 100 μm thick CR-39 detector (BRYOTRAK), a 3 mm thick poly(methyl methacrylate) (PMMA), and a 2 mm thick Teflon. The rear surface of the CR-39 detector is directly contacted onto the plastic plate (PMMA) which works as a backscatterer and a moderator.

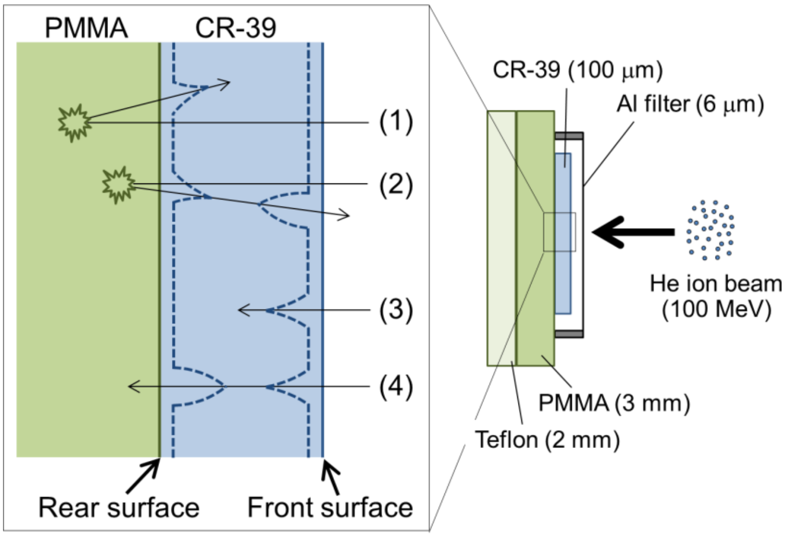

Fig. 4.4 Schematic cross-sectional view of the ion detector unit for the backscattering technique experiment, and four possible etch pit production processes (1)–(4).

The detector unit was exposed to the ion beam with a total fluence of 2.0×10^8 ions/cm^2. The irradiated CR-39 samples were chemically etched in a stirred 6M KOH solution at 70 ℃ for a total 6 h using a multi-step etching technique.

4.2.2 Results and Discussion

4.2.2.1 Observation of etch pits having elliptical opening shapes

The energy of an incident ion beam (100MeV) is far beyond the detection threshold limit (40MeV) of BARYOTRAK (Fukuvi Chemical Industry) for He ions, i.e., the stopping power of the ion is too small to create etchable tracks inside the 100 μm thick CR-39 detector. However, in contrast to this fact, a large number of etch pits are observed in Figs. 4.3 (b) and 3(c), which show spatial distributions of the etch pits registered on the front and rear surfaces of the CR-39 detector, respectively, obtained by scanning the whole CR-39 surfaces by fast scanning microscopy (Seiko Precision HSP-1000). The spatial distribution for the rear surface well reproduces the intensity distribution of the incident ion beam, while that for the front surface is somewhat blurred.

The surfaces of the etched sample were examined in greater details by using an optical microscope (Olympus BX60-F3). It is found that most of the etch pits on the rear surface have elliptical openings, which indicates that high energy ions are obliquely entered into the CR-39 surface with random angles. On the other hand, almost no etch pit was observed when the single 100 μm thick CR-39 detector without the plastic plates was exposed to the ion beam.

These observations strongly suggest that the incident 100MeV He ions once passed through the CR-39 detector without creating any etchable track, and that various nuclear reactions were induced by the incident He ions in the plastic plates. As a result, various product ions including intact He ions hit into the CR-39 detector from the rear surface, and etchable tracks were created on both the rear and front surfaces via processes (1) and (2) shown in Fig. 4.4. In fact, as shown in Fig. 4.5, the etch pit radii suggest that the pits are created by protons, He ions, and other heavy ions. Note that the range for 100MeV He ions is calculated as 4.3mm in the plastic plates, and that the number of the etch pits having elliptical openings on the rear surface is about ten times greater than that on the front surface.

4.2.2.2 Evaluation of traveling directions of ions with respect to the CR-39 surface

The etch pits located around the beam center were investigated by establishing their growth curves, in which the semi-minor axis of an elliptical-cone etch pit have been measured. Concerning the relationship between pit structures and growth curves, it has been examined that the growth curve behaviors for the semi-minor axis of an elliptical opening are identical to those for the radius of a circler opening. The multi-step etching technique, in which the chemical etching and the microscopic observations of pit size are repeated, is employed to establish growth curves. Figures 4.5 (a)-(c) shows typical microscopic images of the temporal evolution of etch pits. The results of the typical growth curve were analyzed for the three etch pits having elliptical openings (#1-#3) are shown in Figs. 4.5 (d) and (e).

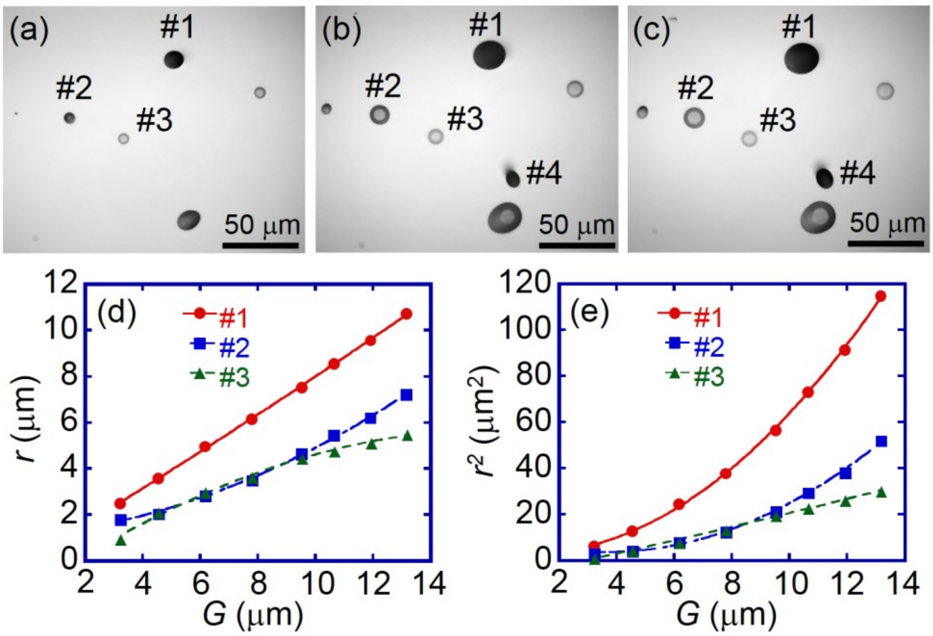

Fig. 4.4. Typical images of etch pits on the rear surface of the CR-39 detectors after etching for (a) 2, (b) 4, and (c) 6 h. The growth curves for the etch pits #1-#3, plotting with (d) the semi-minor axis r and (e) the squared one r^2 as a function of removed surface layer G.

Since the growth curves for r and r^2 for the pits #1 and #2 are expressed as convex-downward increasing functions of G, respectively, the pit structures can be categorized into the trumpet profile, which means that the ions were passed through the rear surface from outside. Therefore, it can be concluded that the pits #1 and #2 are created by the backscattered particles. The microscope observations shown in Figs. 4.5 (a)-(c) show that the etch pits have different brightness, which is dominated by the pit profile. An etch pit with a sharp cone angle exhibits a dark opening like pit #1, which could be created by relatively heavier particles such as carbon. On the other hand, a shallow etch pit with a large cone angle shows a brighter center region like pit #2, which could be created by relatively lighter particles such as protons or He. Since the growth curve for r^2 for pit #3 is linearly proportional to G, while that for r can be expressed as a convex-upward increasing function of G, the pit structure can be categorized into being spherical and shallow, which means that the ions passed through the rear surface from outside. Therefore, it can be concluded that pit #3 is also created by the backscattered particles. Since the pit #3 has a brighter center, it can be concluded that the pit #3 was created by relatively lighter particles such as protons or He. It is worth noticing that several etch pits show up in the process of chemical etching. For example, etch pit #4 seen in Figs. 4.5 (b) and (c) appears after 4 h etching. It is conceivable that this kind of etch pit can be produced by nuclear spallations as well as high energy neutrons generated in the plastics including backscatterers and CR-39 detector.

The same analysis was carried out for 50 and 100 etch pits located inside the square boxes of the front and rear surfaces, respectively, because the density of etch pits inside the beam spot area on the front surface is about one half of that for the rear surface [see Figs. 4.3 (b) and (c)]. On the rear surface, it has been found that all the analyzed etch pits, except for a few etch pits that cannot be identified, have the trumpet profiles and the spherical phases, which leads us to conclude that almost all of the etch pits on the rear surface are created by the backscattered particles via processes (1) and (2) in Fig. 4.4. On the front surface, it has been found that 80% of the analyzed etch pits have the spherical phases and 20% have the bell profiles, which leads us to conclude that the former etch pits are created by the low-energy ($E \leqq 40$MeV) background particles the process (3) in Fig. 4.4, while the latter etch pits are created by the backscattered particles that penetrated through the CR-39 detector from the rear surface via process (2) in Fig. 4.4. Therefore, the experimental results show that about 10% of the backscattered particles passed through the CR-39 from the rear to the front surface. The total number of the backscattered particles can be roughly estimated as $\sim 10^4$ ions/cm^2. Therefore, about 0.01% of the incident ions were reflected back by the plastic plates.

4.2.2.3 PHITS code simulations

Simulations using the PHITS code, which model the experimental configurations, have been performed to evaluate the yields of the backscattered particles from PMMA/Teflon sheet to the rear surface of the CR-39 detector. The results show that about 8% of the backscattered particles passed through the CR-39 from the rear to the front surface, and that 0.01-0.001% of the incident ions are reflected back by the plastic plates. The simulations also show that the backscattered particles are neutrons, protons, He, and other heavy ions such as carbon, which are produced by nuclear reactions in the plastic plates. These are consistent with the experimental results.

4.2.3 Conclusions

It has been demonstrated that the simple diagnosis method for high energy ion beams using a single CR-39 detector mounted on plastic plates. A large number of etch pits having elliptical openings were observed on the rear surface of the CR-39 detector by 100 MeV He ion beam irradiation of the CR-39 detector unit, whose energy was far beyond the detection threshold limit (40 MeV) of the CR-39 detector. The spatial distribution of the etch pits well reproduced the intensity distribution of the incident He ion beam. The growth curve behavior analyses using the multi-step etching technique revealed that the etch pits having elliptical openings were created by the backscattered particles, which were produced by various nuclear reactions in the plastic plates and hit into the CR-39 detector from the rear surface. About 0.01% of the incident ions were reflected back by the plastic plates, which agreed with the results of the PHITS code simulations.

This method allows a simple diagnosis of the ion beam profile and determination of the presence of the high energy component beyond the detection threshold limit of the CR-39 detector even in mixed-radiation fields, therefore, this method in combination with a magnetic energy spectrometer can be a powerful tool for the characterization of laser-driven ion beams having a broad energy spectrum.

This method has been applied to the laser-driven ion acceleration experiment using CO_2 (cluster) + He (gas) target, which is conducted with the J-KAREN at JAEA-KPSI. In the experiments, He ions with the maximum energy of 50 MeV/n were detected by using the developed method in a field contaminated with X-rays and high energy electrons [7].

Chapter 5 An Evaluation of Photo-Neutrons in Laser-Driven Ion Acceleration Experiments

5.1 An evaluation of photo-neutrons using PHITS code

In laser-driven ion acceleration experiments using the cluster-gas targets, a significant amount of fast electrons, which drives the ion acceleration, are produced along with high energy ions with several-tens of MeV. In the recent experiment using CO_2 clusters embedded in H_2 gas conducted with the J-KAREN laser facility (1 J, 40 fs) at JAEA-KPSI, the maximum energy of electrons reaches up to 200 MeV. As described in section 1.1.3, such high energy electrons could produce high energy photons via bremsstrahlung processes. Accordingly, the photons could produce photo-neutrons via a series of (γ, n) reactions. In order to diagnose the "laser-accelerated protons" exclusively in such photo-neutron contaminated fields, it is a crucial issue to evaluate the effects of photo-neutrons in CR-39 track detectors, because the CR-39 can also record etchable tracks of "recoiled protons" kicked out by the neutrons as "fake proton signals". In order to diagnose the laser-accelerated proton beams using CR-39, it has been carried out that an evaluation of photo-neutrons which derived from laser-accelerated high energy electrons using PHITS code.

5.1.1 Reconstruction of the experimental condition

In order to calculate the photo-neutron fluxes in ion detector unit, the experimental setup in JAEA-KPSI was reconstructed in PHITS. Figure 5.1 shows the top view of the experimental set up which is described by PHITS code.

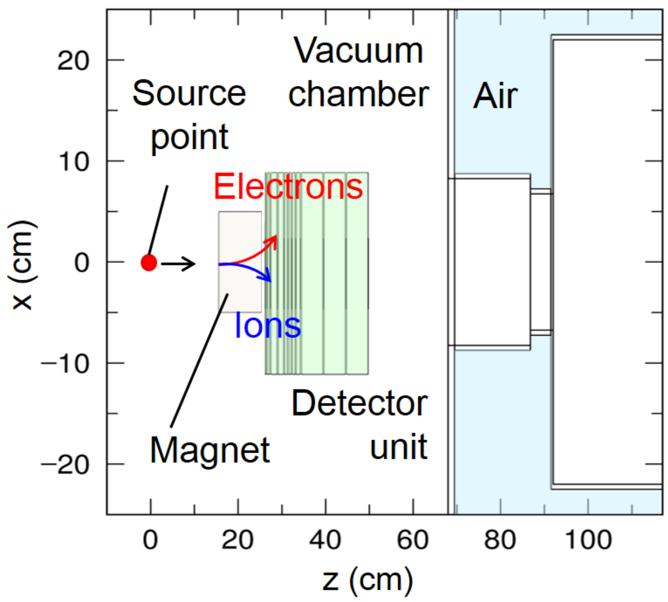

Fig. 5.1 Top view of the experimental setup in PHITS code.

The focusing intense laser comes from left side and irradiate to the CO_2 (cluster) + H_2 (gas) target on the nozzle, which is the source point. Then, ions and electrons were accelerated to the same direction of laser axis along the black arrow in Fig. 5.1. The laser-accelerated electrons were deflected to the upper side of the plane by the magnetic field, on the other hand, the laser-accelerated ions were deflected to the lower side of the paper. The deflected electrons, which higher energy components, were entered into the stacked detector unit and also vacuum chamber wall which is consisted the stainless steel. And lower energy components were entered into the phosphor screen DRZ-high which is the detection part of the electron spectrometer (ESM). On the other hand, the deflected laser-accelerated ions were entered into the stacked CR-39 detector unit as shown in Fig. 5.2.

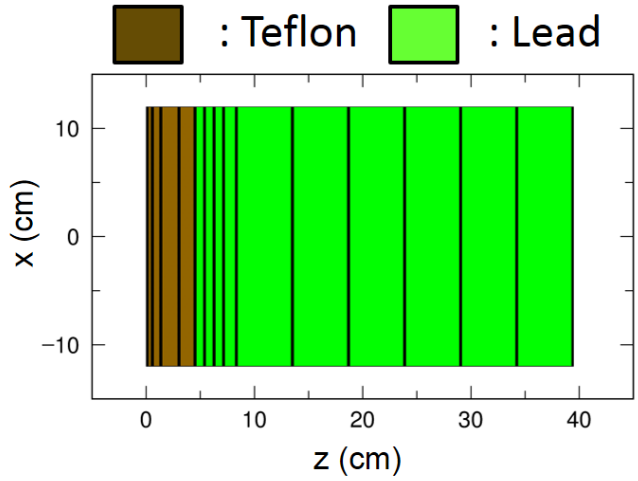

Detectable energy point (MeV)		
10	125	410
30	150	500
50	170	575
80	200	655
100	310	730

Fig. 5.2 Stacked CR-39 detector unit and detectable energy points.

The designed stacked detector unit was consisted by Teflon and lead blocks for energy filters and two-ply CR-39 were inserted between the each energy filter. The designed detector unit provides the energy spectrum of laser-accelerated protons with a wide energy range from 1 to 730 MeV in 40 cm which is the limit of the space of vacuum chamber. The detector unit was installed at just behind the magnet to measure the laser-accelerated ions as much as possible.

5.1.2 Preliminary experiment

As a preliminary experiment, the energy spectrum of laser-accelerated electrons applied CO_2 (cluster) + H_2 (gas) target were measured by using the ESM. In this preliminary experiment, the stacked detector unit has not been installed to obtain the full-range energy spectrum of electrons.

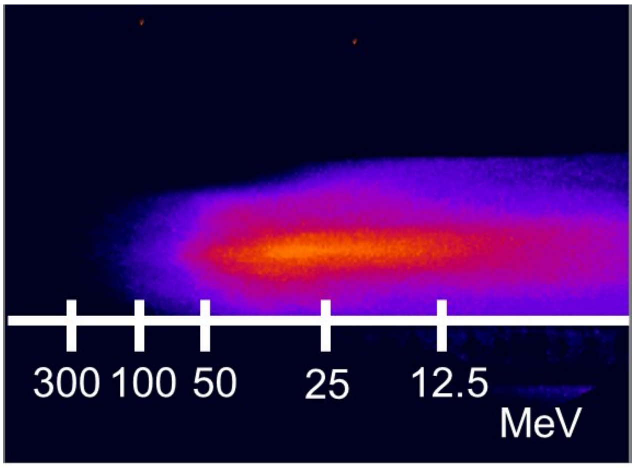

Fig. 5.3 The energy spectrum of laser-accelerated electrons on phosphor screen.

The wide-spread energy spectrum has been observed with the maximum energy of 200 MeV as shown in Fig. 5.3 and total charge is about 1 nC per single laser shot. The averaged spectrum of laser-accelerated electrons was duplicated on PHITS code and generated at source point. In this study, the divergence of laser-accelerated electrons was set 0 degree i.e. cylindrical beam and the transport direction was also set along the arrow in Fig 5.1 which is the same direction of laser.

5.1.3 An evaluation of photo-neutron fluxes in the stacked detector unit

Figure 5.4 shows the spatial distribution of the photo-neutron fluxes (a), and the fluxes of neutron, electron and photon in detector unit as a function of depth in detector unit (b) calculated by PHITS code.

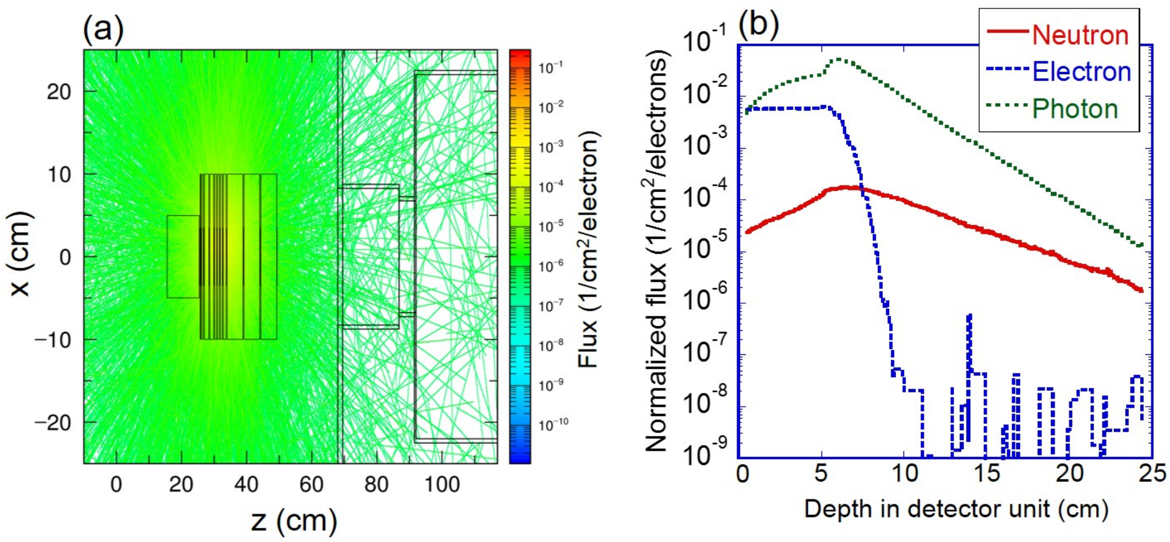

Fig. 5.4 The spatial distribution of the photo-neutron fluxes (a), and the fluxes in detector unit as a function of depth in detector unit (b).

From this result, it can be estimated that the maximum photo-neutron flux is 10^{-4} per electron, therefore,

10^6 photo-neutrons were generated per single laser shot in the stacked detector unit. This number of photo-neutrons can create the 10 etch pits on CR-39 per one laser shot because the detection efficiency of neutrons by CR-39 is around 10^{-4} pits/neutrons. In laser-driven ion acceleration experiments using cluster-gas target, it can create a significant amount of fake protons signals because of the laser shot accumulated more than 2000 shots using same CR-39 detectors.

In conclusion, the flux of photo-neutrons in detector unit has been evaluated using PHITS code. The high energy electrons can produce a significant amount of noise signals for CR-39. It is important that the designed ion detector system evaluate the photo-neutron fluxes using PHITS code and optimize the configuration of experimental setup to minimize the photo-neutron contaminants.

5.2 Discrimination method of etch pits created by laser-accelerated protons and recoiled protons by photo-neutrons using CR-39

In laser-driven ion acceleration experiment using cluster-gas target, a significant amount of photo-neutrons were generated as described in 5.1. In order to measure the laser-accelerated proton beams precisely using CR-39, the etch pits created by laser-accelerated protons and the etch pits of recoiled protons by photo-neutrons must be distinguished. In the present study, it has been developed that the discrimination method of laser-accelerated protons and recoiled protons based on the incident angles determined by the shape of etch pit open mouth and the incident energies determined by the both radius and grayscale of the etch pit. Finally, the developed method has been applied to the laser-driven ion acceleration experiment using CO_2 (cluster) + H_2 (gas) target.

5.2.1 A discrimination method based on the etch pit shape

5.2.1.1 The pattern of etch pit by protons

In order to understand the difference of laser-accelerated protons and recoiled protons by neutrons, the all assumed pattern of incident protons were described as shown in Fig. 5.5. Figure 5.5 indicate the cross sectional view of the two-ply of CR-39 and the laser-accelerated protons and neutrons were come from left side. The pattern No. 1 shows the case of laser-accelerated proton and Nos. 2-4 show the case of recoiled protons by neutrons.

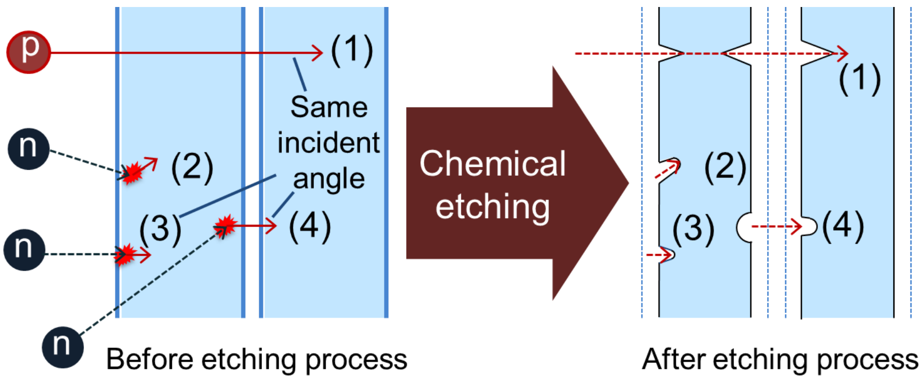

Fig. 5.5 Patterns of incident protons for two-ply CR-39.

The case of laser-accelerated protons such as No.1 in Fig. 5.5, the incident angle is almost perpendicular to the detection surface of CR-39. And also the incident angles of laser-accelerated protons can be calculated using particle transportation code if it deflected by external magnetic field because the generation point of protons were uniquely decided by experimental set up.

The next case (No.2 in Fig. 5.5) is neutron entered into CR-39 and recoiled proton with oblique incident to the detection surface of CR-39. In this case, the etch pit can be assigned to the derived from neutrons because the incident angles were different from the laser-accelerated protons such as the case No.1 in Fig. 5.5.

The next cases (Nos.3 and 4 in Fig. 5.5) are neutron entered into CR-39 and recoiled proton with normal incident to the detection surface of the first and second layer of CR-39. The case Nos.3 and 4 cannot be distinguished based on the incident angles because the incident angles are same as laser-accelerated protons. Accordingly, the differences of incident energies were used instead of the incident angles. The incident energies of laser-accelerated protons were distributed from low energy to several-tens of MeV. On the other hand, the energies of recoiled protons must be lower than the initial neutrons energies. The energies of photo-neutrons in the laser-driven ion acceleration experiments can be estimated below a few MeV, the recoiled protons energies were also below a few MeV. Therefore, the etch pit which exceed the maximum energy of photo-neutron can be assigned to laser-accelerated protons even when the etch pit with normal incidence.

Taken together, the etch pits with the ideal incident angles and higher energy than photo-neutrons could be assigned to laser-accelerated protons. The other etch pits, which unsatisfied the upper requirements, were assigned to recoiled protons derived from photo-neutrons.

5.2.1.2 Incident angles

Figure 5.6 shows the top view of the etch pit open mouth and cross sectional view of the etch pit with incident angle θ.

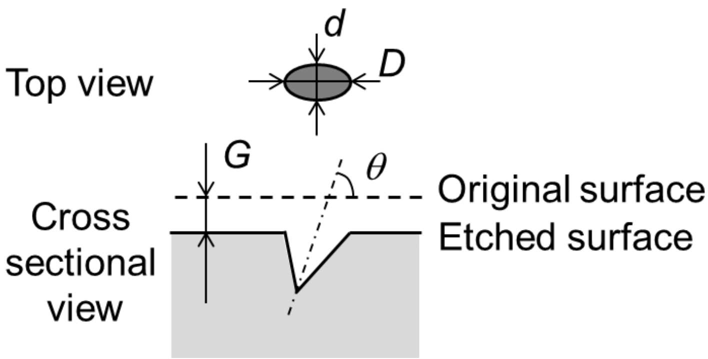

Fig. 5.6 Top view of the etch pit open mouth and cross sectional view of the etch pit.

The minor axis d and major axis D of the each etch pit open mouth can be obtained by usual optical microscope observation. And the thickness of layer removed G can be evaluated by the etch pit radius of fission fragment from ^{252}Cf source (see in 2.1.3). The eth pit cross sectional view, however, as shown in Fig. 5.6 cannot observe directory by the optical microscope. Therefore, the incident angle must be evaluated from the only minor axis d, major axis D, and thickness of layer removed G. In the present study, the equation (5.1), which derived by Somogyi [31], was employed to obtain the incident angle with the limited information from the optical microscope observations.

$$\sin\theta = \frac{1+\left(\frac{d}{2G}\right)^2}{\sqrt{\left(1-\left(\frac{d}{2G}\right)^2\right)^2+4\left(\frac{D}{2G}\right)^2}}, \tag{5.1}$$

where d is minor axis and D is major axis of the etch pit open mouth, the G is thickness of layer removed, and the θ is the incident angle to the surface of CR-39. The incident angle of each etch pit, which is obtained by laser-driven ion acceleration experiments, was obtained by substituting the d, D, and G to the eq. 5.1 and inverse function of the sine.

5.2.1.3 Incident energies

In order to obtain the incident energy, the multi-step etching technique (see in 2.1.3) can be applied. But the multi-step etching technique is not suitable method for the case of a large number of etch pits are existed on CR-39, because the multi-step etching technique needs to observe the same etch pit before and after the etching for every etch pits. Realistically, a several hundred is the maximum number of the etch pits for applying the multi-step etching technique. Accordingly, the analysis method was developed to obtain the incident energies for each etch pit only one-time etching based on the minor axis of the etch pit open mouth and grayscale of the center part of the etch pit.

The case of laser-accelerated protons, the etch pits grow from the surface of CR-39. On the other hand, the case of recoiled protons derived from photo-neutrons, the etch pits grow from the recoiled position which is the inner side of CR-39. When mixture these two cases, the etch pit of high energy laser-accelerated proton and the etch pit of recoiled proton cannot be distinguished by the etch pit minor axis only, because the etch pit minor axis can be almost same length. Therefore, not only etch pit minor axis but grayscale of center part of the etch pit were employed. The correlation of the grayscales and the incident energies has been studied by Law et al [53]. The grayscale of the etch pit center part reflect the information of the etch pit tip shape and the depth. The etch pit tip shape and the depth can be varied depends on the incident energies of protons.

As a preliminary experiment, 0.5, 1, 3, 4, and 5 MeV protons were irradiated to CR-39 samples respectively by using the conventional accelerator at HIMAC [54]. These samples were chemically etched by 6M-KOH solution at 70℃, which is the completely same condition as CR-39 samples used in laser-driven acceleration experiment. After the chemical etching processes, CR-39 samples were observed by the wide area scanning optical microscope HSP-1000, and then the etch pit minor axis d and grayscale g have been obtained. Figure 5.7 shows the result of this preliminary experiment, minor axis (a) and grayscale (b).

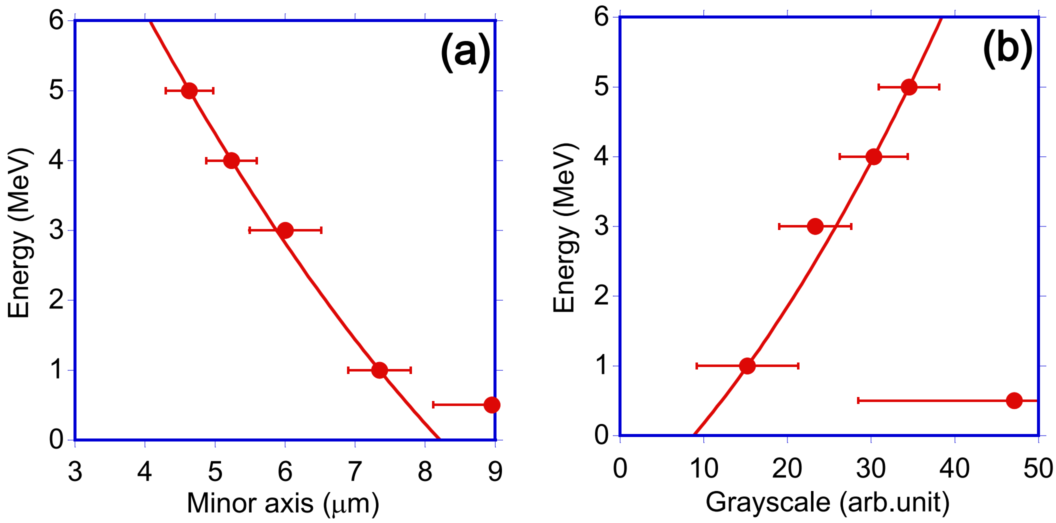

Fig. 5.7 Calibration curves for protons energy as functions of minor axis (a), and grayscale (b).

The etch pit minor axis becomes smaller with an increase of the incident energy as shown in Fig. 5.7 (a). The case of 0.5 MeV, the etching depth was beyond the range of protons i.e. etch pits were rounded out. The correlation between minor axis and incident energy can be described as approximate function except 0.5 MeV.

The grayscale of etch pit center part becomes larger i.e. brighter with an increase of the incident energy as shown in Fig. 5.7 (a) except 0.5 MeV. This result indicate that the high energy protons create the shallow etch pit because of the smaller stopping power and low energy protons create the deep etch pit because of the larger stopping power. On the other hand, the large grayscales of etch pits with the energy of 0.5 MeV indicated the rounded etch pits tips. The correlation between grayscale and incident energy can also describe as approximate function except 0.5 MeV.

From these result, the two quadratic functions as follows were obtained by the least squared method. These two functions express the energy calibration curve for protons as a function of minor axis (5.2), and grayscale (5.3).

$$E = 0.08966d^2 - 2.549d + 14.89, \quad (5.2)$$

$$E = 0.0020281g^2 + 0.10644g - 1.0937, \quad (5.3)$$

where d is minor axis of the etch pit open mouth, g is the grayscale of the etch pit center part, and E is incident energy.

Note that the eq. 5.3 cannot be applied for higher energy region more than 7 MeV, because the value of grayscale will be same as the 0.5 MeV. In this study, the applied energy region of eq. 5.3 was limited as 1-7 MeV.

CR-39 samples, which obtained by laser-driven ion acceleration experiments, were analyzed under the condition as the etch pit must be satisfied the both eq. 5.2 and eq. 5.3 at the same time. For example, the etch pits which were incorrectly evaluated their energies were excluded from the analysis targets such as the etch pit which evaluated 3 MeV by eq. 5.2 but 6 MeV evaluated by eq. 5.3. In the present study, the etch pits which satisfied the difference less than 1.5 MeV between evaluated incident energies from eq. 5.2 and eq. 5.3 were analyzed.

Thus, the incident energy of laser-accelerated proton was evaluated for each etch pit based on the etch pit minor axis and grayscale of the etch pit center part.

5.2.2 Laser-driven ion acceleration experiment

5.2.2.1 Experimental setup

Figure 5.8 shows the schematic top view of the laser-driven ion acceleration experiment using cluster-gas target. Focusing J-KAREN laser irradiated to the CO_2 (cluster) + H_2 (gas) target, and then ions and electrons were accelerated to the same traveling direction of laser axis. The laser-accelerated electrons and ions were deflected by the external magnetic field using dipole magnet behind the slit with 11 mm width. The laser-accelerated electrons were deflected to the upper side of the plane and entered into electron dump which consisted by Teflon and lead block with the thickness of 5 cm respectively.

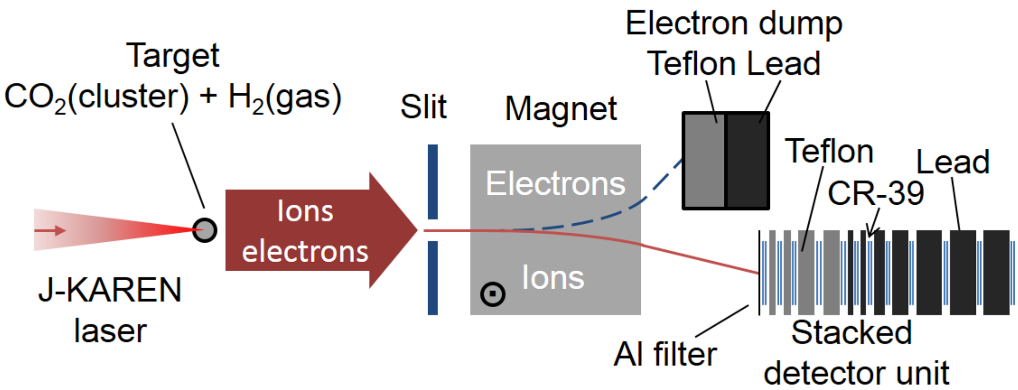

Fig. 5.8 Schematic top view of the laser-driven ion acceleration experiment using cluster-gas target.

On the other hand, the laser-accelerated ions were deflected to the lower side of the plane and entered into the stacked CR-39 detector unit (see Fig. 5.2). In order to avoid CR-39 were exposed to the laser light directly, a 6 μm thick aluminum filter was mounted on the stacked detector unit. In this experiment, HARZLAS (TD-1) were applied as a CR-39 detector.

After the 2500 laser shots accumulation, the CR-39 samples were chemically etched 5 hours by 6M-KOH solution at 70 degree of Celsius, and then the microscope observations using HSP-1000 were carried out. In the microscope observations, the minor axis, major axis and grayscale were evaluated for each etch pit.

The generated photo-neutrons energies were evaluated by time-of-flight method using ^{3}He detector. ^{3}He detector was set in the same plane of the laser axis and 5.5 m from the vacuum chamber wall. The photo-neutrons signals from ^{3}He detector were analyzed by oscilloscope and measured the time from the laser shot timing.

5.2.2.2 Threshold of discrimination

Firstly, the thresholds of the incident angles of laser-accelerated protons for CR-39 were decided. The incident angles were calculated by three-dimensional electro-magnetic field analysis software AMaze. The tracks of laser-accelerated protons in vacuum chamber were simulated under the precise magnetic field which is installed in the experiment. From the calculation results, the ideal incident angles for CR-39 were decided as 5-15 degree and 0-10 degree for below 30 MeV and above 30 MeV respectively. These angles were considered the width of the slit. Accordingly, if the incident angle which is evaluated by the etch pit analysis was within the limits, there are some possibilities that the etch pits includes those from laser-accelerated protons. On the other hand, the etch pit beyond the limits of ideal incident angles can be assigned to it created by recoiled proton.

Secondly, it has been considered that the threshold of incident energy for each layer of CR-39 were determined from the maximum energy of photo-neutron. Figure 5.9 shows the energy spectrum of photo-neutrons which is obtained by time-of-flight method using ^{3}He detector with 2500 laser shots accumulation.

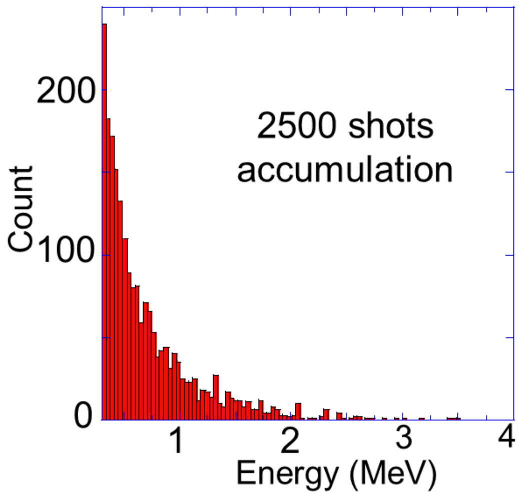

Fig. 5.9 Energy spectrum of photo-neutrons.

From the experimental results, the maximum energy of photo-neutron was 4 MeV, so the energies of recoiled protons were decided below 4 MeV. Therefore, there are some possibilities that the etch pits includes those from laser-accelerated protons which have been evaluated more than 4MeV.

To summarize, it can assign to the laser-accelerated protons that the etch pits were evaluated above 4 MeV and within the limits of ideal incident angles. And other etch pits can be assigned to recoiled protons.

5.2.3 Results and discussion

5.2.3.1 Incident angle and incident energy distributions

The angular distribution and energy distribution of the etch pits on first layer of stacked CR-39 were obtained as shown in Fig. 5.10.

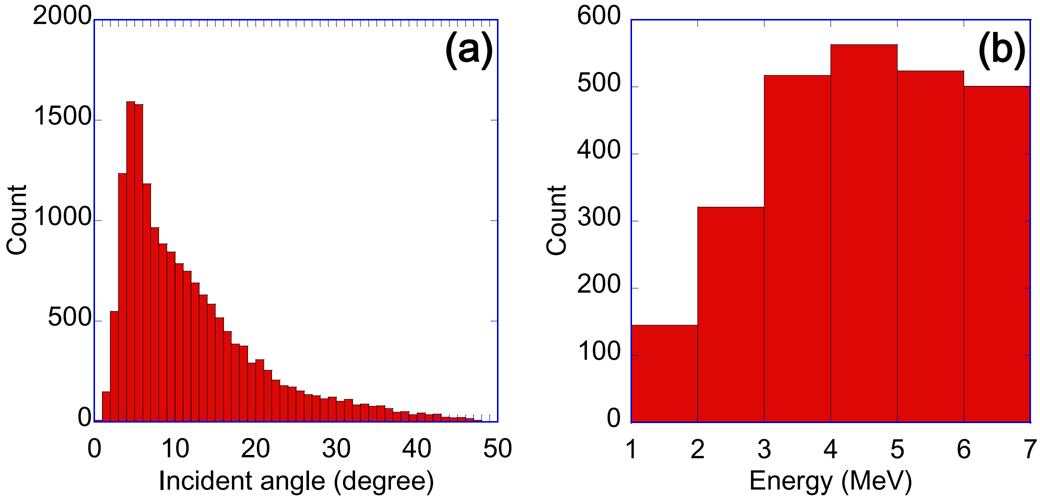

Fig. 5.10 Angular distribution (a), and energy distribution (b) of the etch pits on the first layer.

From the result of angular distribution as shown in Fig. 5.10 (a), the protons which include the recoiled protons were mostly incident below 10 degree. The small number of etch pits were evaluated above 30 degree, but note that the protons with large incident angles are exist. The detection efficiency of CR-39 depends on the angle of incidence of charged particles. Above a critical angle, no etchable track can be made visible by the etching process [55]. The critical angle depends on the stopping power of charged particle. For example, a proton with 3 MeV and above 25 degree of incidence cannot create the etch pit.

From the result of energy distribution as shown in Fig. 5.10 (b), the number of high energy protons is larger than low energy component. This is because the etch pit which is created by recoiled proton with large incident angle indicate very shallow and elliptical open mouth. In this case, the size and grayscale of the etch pit may regard as the high energy components. In the present study, such etch pit is never selected as the laser-accelerated proton thanks to the combination of incident angles and incident energies.

5.2.3.2 Selection of the etch pits

Firstly, the etch pits analysis has been carried out based on the developed discrimination method for front surface of the first layer of stacked CR-39. Figure 5.11 (a) shows the example of the selected etch pit as a laser-accelerated protons. The etch pit minor axis is 3.6 μm and grayscale is 41, therefore, the incident energy can be estimated around 6.8 MeV from the eq. 5.2 and eq. 5.3. And also, the incident angle was 4 degree. On the other hand, Fig. 5.11 (b) shows the instance of the unselected etch pits. From the optical microscope image, it is clear that these etch pits have large incident angles, so these etch pits can be created by recoiled protons.

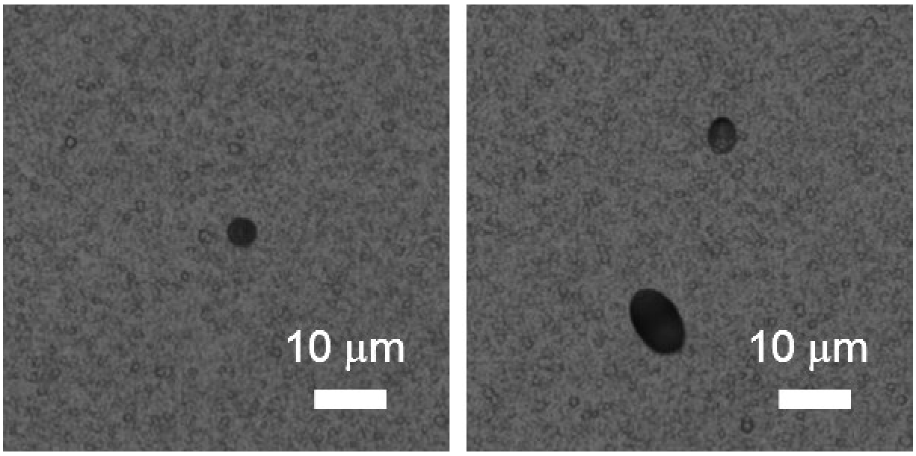

Fig. 5.11 Etch pits of the laser accelerated proton (a), and recoiled protons (b).

The same analysis has been carried out for the front surface of every layer of stacked CR-39. Table 5.1 shows the analysis results of first and second layer of CR-39 which is inserted just behind the 6 μm aluminum filter. Note that the analysis area of CR-39 is 6×6 cm^2.

Table 5.1 The number of etch pits on CR-39.

	All	Selected
1st layer	19299	95
2nd layer	39678	108

The number of all etch pits on the second layer is larger than it on the first layer. This is because the first layer of CR-39 worked as a radiator for recoiled proton generation when the photo-neutrons entered into the stacked CR-39 detector unit from the front side. The small number of etch pits were selected as laser-accelerated protons.

Figure 5.12 shows the result of the etch pit selection for all first layer of inserted two-ply CR-39 between the energy filters as a function of depth in stacked detector unit. The dotted line indicates the number of etch pits on CR-39 which is obtained by the etched blank sample.

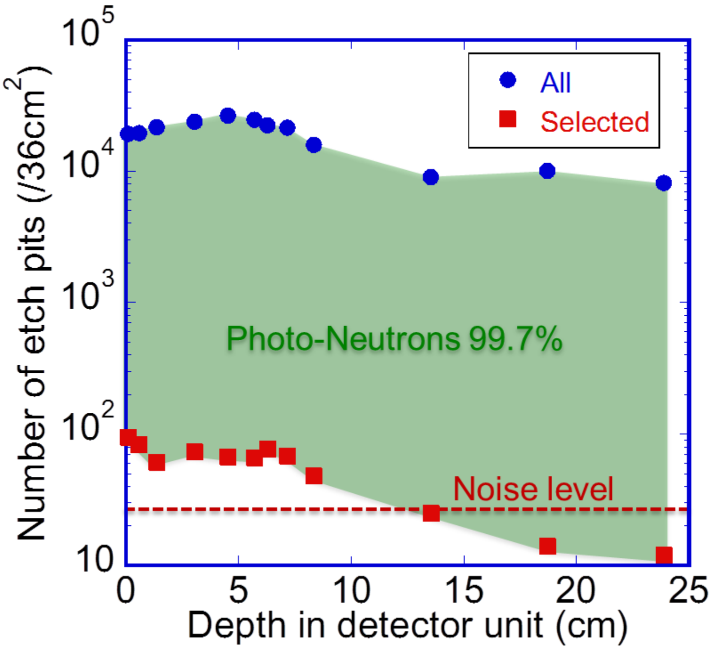

Fig. 5.12 The number of etch pits as a function of depth in stacked CR-39 detector unit.

After the analysis, around 0.3% of all the etch pits were selected. The selected etch pits strongly indicate the laser-accelerated protons because the incident energies are above 4 MeV and the incident angles are within the ideal limit.

Here, the error of this discrimination result was estimated, especially the reliability of selected 0.3%. In this experiment, no neutrons with the energies above 4MeV were detected. Accordingly, criteria are such that a neutron with the energy above 4MeV was generated with a 1/2500 i.e. 0.04% possibility. In addition, it assumed that the neutron recoiled above 4 MeV proton, and the recoiled proton was incident with ideal incident angle. These assumptions are clearly smaller than 1. Then, the possibility of select the etch pit which derived from photo-neutron is enough smaller than 0.04% using the developed method. Therefore, the selected 0.3% etch pits strongly indicate the signals of laser-accelerated protons.

5.2.4 Conclusion

The etch pit discrimination method for laser-accelerated protons and recoiled protons by neutrons has been developed, which is based on the incident angles and incident energies of protons. The developed method adopted not only minor axis but the grayscale of the center part of etch pit to obtain the incident energy. It allow us to evaluate the incident energy more precisely.

The developed method has been applied to the laser-driven ion acceleration experiment using CO_2 (cluster) + H_2 (gas) target, and then 0.3% of all etch pits strongly indicate the laser-accelerated protons and other 99.7% were assigned to derive from photo-neutrons.

This discrimination method can be applied to the ion beam diagnostics using CR-39 in the field contaminated with photo-neutrons.

Chapter 6 Design of laser-accelerated ion beam measurement system

6.1 Concept of laser-accelerated ion beam measurement system with low background noises

Through the whole study, it has been revealed that diminish the noise signals are the most important matter for laser-accelerated ion beam diagnosis. Especially, the noise signals from photo-neutrons can be the serious issue for leaser-driven ion beam diagnostics using CR-39 detectors. To diminish the background noises, especially photo-neutrons, the important point of laser-accelerated ion beam measurement system is as follows:

- Never hit the high energy electrons to the chamber wall.
- Using low-Z materials where hit the high energy electrons.
- Reduce the range of high energy electrons in high-Z materials.
- Protect the photo-neutrons generated in the magnet materials.

These points are mainly corresponds to the treatment of the high energy electrons. Here, the high energy is defined as more than 8 MeV. Because such electrons can produce high energy photons, which energies exceed the threshold of the photo-nuclear reaction. The high energy electrons must be reduced the energy in the low Z materials to diminish the number of high energy photons.

6.2 Design of the system

Figure 6.1 shows the designed system for diagnostics of laser-accelerated ions and electrons.

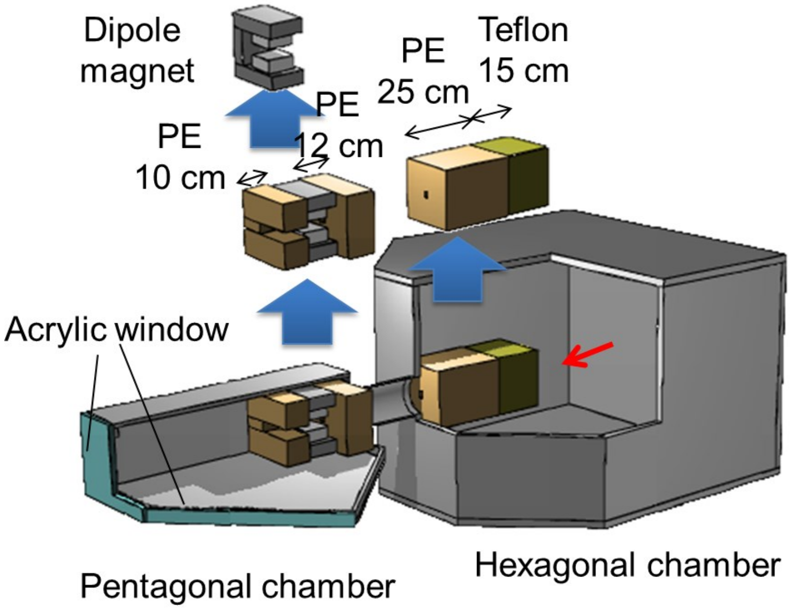

Fig. 6.1 Schematic view of the designed system.

The intense laser comes from the right side along the red arrow and focused on the target which is set at the center of the hexagonal vacuum chamber. The laser-accelerated ions and electrons were transported to the pentagonal vacuum chamber through the two-stage collimators which is composed of 15 cm length Teflon (polytetrafluoroethylene) block and 25 cm length PE (polyethylene) block. After transported to the pentagonal chamber, the ions and electrons through the additional 12 cm length PE collimator, and then deflected by the magnetic field. The electrons are deflected to the front side of the plane, and then entered into phosphor screen which is detection part of electron spectrometer (ESM). The luminescence of the phosphor screen is imaged by CCD shot by shot through the acrylic window. On the other hand, the ions are deflected to the back side of the plane and enter into the stacked CR-39 detector using Teflon blocks as energy filters. Note that the width of the collimators can be changed depends on the required resolution of the ESM. And also, the additional Teflon blocks are set just behind the magnet.

The important point of this design with low background noises is as follows. 20×20 cm^2 wide and 15 cm depth Teflon collimator has been set near the generation point of ions and electrons as shown in Fig. 6.1. If the high energy electrons accelerated to any unexpected forward direction, this Teflon block reduce the energy of high energy electrons with the small number of high energy photons, because this Teflon block can cover the all visible angle of the front chamber wall from the generation point. And also, the number of photo-neutrons which generated in the Teflon block by the unexpected directional electron beam can be diminished by the PE blocks.

In pentagonal vacuum chamber, the high energy electrons after through the collimators are deflected by the magnetic. The trajectory of electrons were changed which depends on their energy. The higher energy components which proceed with small deflection will hit the front wall of chamber. In order to decrease the number of high energy photons, the acrylic window has been chosen for the front wall material. On the other hand, the lower energy components will hit the side wall of the chamber. If the chamber shape is rectangle, the electrons enter into the chamber wall and progress through the long distance inside the materials. Then, the pentagonal chamber is suitable for the ion beam diagnostics.

The last point is generation of photo-neutrons in the dipole magnet. The dipole magnet which is consisted of stainless steel and Nd magnet have to be installed to measure the electron spectrum and separate the ions. Therefore, the PE block has been installed just after the dipole magnet to protect the stacked detector unit from neutrons.

6.3 Simulations of the fluxes of photo-neutrons

In order to confirm the neutron fluxes in the designed system, the Monte Carlo particle transportation simulations have been carried out using PHITS code. The details of the ion measurement system has been reconstructed on the PHITS as shown in Fig. 6.2 (a), and the electron beam is generated at the source point and transported along the red arrow with divergence 10 degree. Figure 6.2 (b) shows the parameters of installed electron beam, the maximum energy is 200 MeV and electron temperature is 50 MeV.

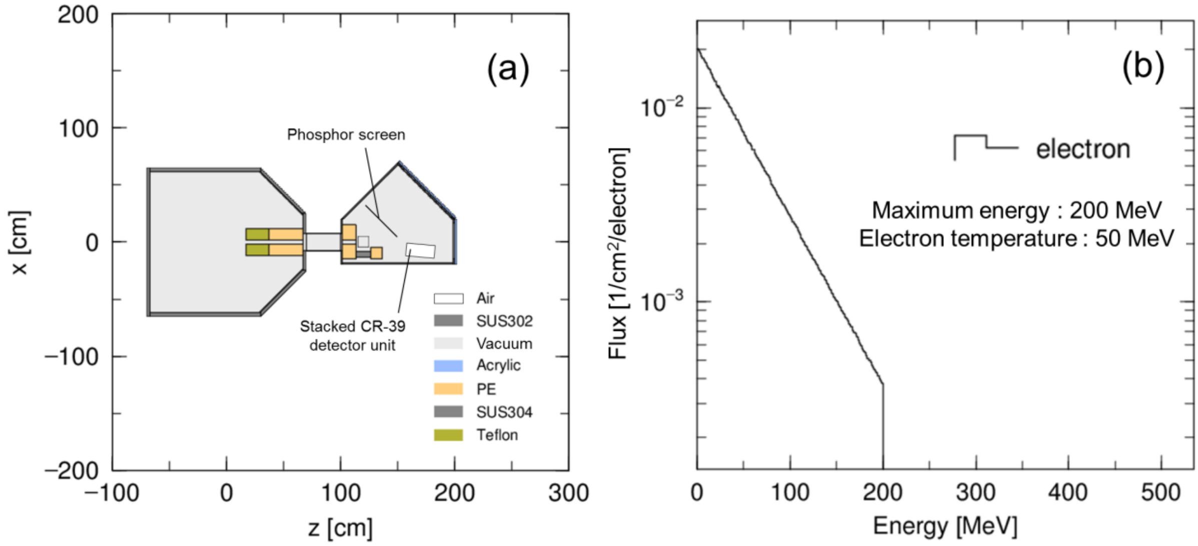

Fig. 6.2 Schematic top view of the ion measurement system reconstructed on PHITS code (a) and the energy spectrum of the installed electron (b).

Figure 6.3 shows the calculation results of electrons (a), photons (b), and neutrons (c).

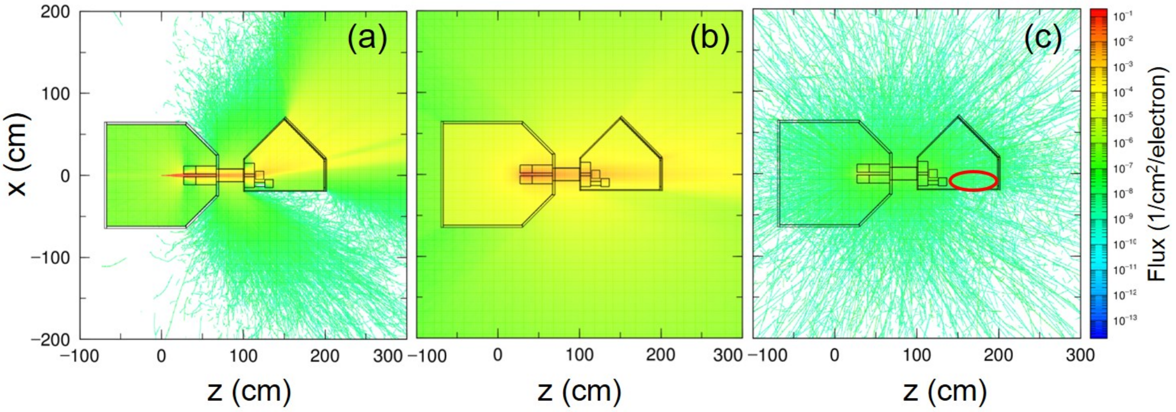

Fig. 6.3 Calculated trajectories of electrons (a), photons (b), and neutrons (c).

Figure 6.3 (a) shows the electron trajectories. This result indicates that the high energy electrons were deflected by the magnet and passed through the acrylic window. Figure 6.3 (b) shows the distribution of photons. Most of photons were generated at the Teflon collimator. Figure 6.3 (b) shows the flux of photo-neutrons. This result indicates that the neutron flux can be reduced as 10^{-8} per the number of the source electrons at the stacked detector unit position rounded by red circle. The case of CO_2 (cluster) + H_2 (gas) target, the averaged electron charge was 1 nC i.e. around 10^{10} electrons were accelerated, so the number of neutrons can be expected as 10^2 per single laser shot by the simulation. This number of photo-neutron cannot create the etch pit per single laser shots, because the detection efficiency of neutrons by using CR-39 is around 10^{-4} pits/neutrons.

The simulation results revealed that the designed system can be utilized for the precise diagnosis of laser-accelerated ion beams with less contaminant by photo-neutrons.

Chapter 7 Conclusions

For the precise measurement of laser-accelerated ions, two diagnosis methods and one analysis method of CR-39 were developed as follows:

1. CR-39 track detectors have been applied for laser-driven ion acceleration experiment. To precise diagnose laser-accelerated ions, the analysis techniques of CR-39 were employed for the first time such as multi-step etching.

2. Laser-accelerated protons from thin foil target were measured by using CR-39 stacked detector unit. The spatial distribution of the etch pits shows that the high energy components indicated the directional beam. By means of multi-step etching technique, the maximum energy of the proton was determined as 14.39 ± 0.05 MeV in the experiment. This method, which combined the stacked CR-39 detector unit and multi-step etching, allows us to measure the energies with uncertainty ΔE=0.1 MeV. The uncertainty is ten times higher than the conventional measurement systems such as time-of-flight method in energy resolution.

3. For intense high energy ion beams, it has been developed that the new simple diagnosis method for high energy ion beams using a single CR-39 detector mounted on plastic back-scatterers, which can use in a field contaminated with X-rays and high energy electrons. The proof-of-principle experiment has been demonstrated using He ion beams with the energy of 100 MeV which exceed the detection threshold of CR-39. A large number of etch pits were observed on the rear surface of the CR-39 by and the spatial distribution of the etch pits on rear surface well reproduced the intensity distribution of the incident He ion beam. By using the multi-step etching technique, the growth curve behavior indicated the etch pits were created by the backscattered particles from the plastic back-scatterer. About 0.01% of the incident ions were reflected back by the plastic plates, which agreed with the results of the PHITS code simulations.

4. The diagnosis method using backscattered particles has been applied to the laser-driven ion acceleration experiment using CO_2 (cluster) + He (gas) target, which is conducted with the J-KAREN at JAEA-KPSI. In the experiments, He ions with the maximum energy of 50 MeV/n were detected by using the developed method in a field contaminated with X-rays and high energy electrons.

5. The discrimination method for laser-accelerated protons and recoiled protons by photo-neutrons using CR-39 has been developed, which based on the incident angles and incident energies of protons. The analysis system for wide area CR-39 was created to evaluate the incident angles and incident energies of protons in one time microscope observation. It has been employed that not

only minor axis but also the grayscale of the center part of etch pit in order to obtain the incident energy precisely for each particle.

6. The developed discrimination method has been applied to the laser-driven ion acceleration experiment using CO_2 (cluster) + H_2 (gas) target. The etch pits of protons with the energy exceeding 4MeV, the maximum energy of photo-neutrons, and ideal incident angles were assigned to laser-accelerated protons. It has been revealed that 0.3% of all etch pits strongly indicated the laser-accelerated protons and other 99.7% were derived from photo-neutrons.

For the online diagnosis of laser-accelerated ions, the Thomson parabola spectrometer system was developed as follows:

7. The ZnS(Ag) fluorescent screen has been developed for an online Thomson parabola spectrometer. The thickness of fluorescent screen was optimized to diminish the luminescence by electrons based on the Bethe-Bloch equation.

8. It has been demonstrated that the diagnosis of laser-accelerated ions from thin foil target by using a Thomson parabola spectrometer system with the fluorescent screen. The trajectory of the ions, i.e. luminescence of the fluorescent screen, was measured by a usual CCD camera with the minimum sensitivity of 0.4 lx. The each trajectory has been assigned the charge-mass ratio by PHITS code simulation. In addition, the calibration study using CR-39 has been carried out. The results of the CR-39 and calculations are consistent to the measured trajectories.

To diminish the noise signals from photo-neutrons, the laser-accelerated ion beam measurement system was designed using PHITS code as follows:

9. The large size Teflon and PE blocks, low *Z* materials, were used as collimators to avoid the electrons entered into experimental chamber wall. In addition, the generated photo-neutrons in magnet materials were protected by PE blocks. The shape and the window material of the designed pentagonal chamber was considered from the view point of the behavior of high energy electrons. The flux of photo-neutrons has been evaluated by PHITS code when the high energy electrons were generated in the designed configuration. The simulation results indicated that the number of neutrons at detector position could be expected as 10^2 per single laser shot, which was small enough to diagnose only laser-accelerated protons.

Acknowledgments

The author would like to express the heartfelt appreciation to Professor Dr. Tomoya Yamauchi of Kobe University for his guidance, adequate discussions and unfailing encouragement.

The author is also grateful to Professor Dr. Keiji Oda of Kobe University for valuable discussions, suggestions and warm encouragement.

The author is much indebted to Professor Dr. Koji Kuraoka and Professor Dr. Hideo Okamura of Kobe University for fruitful discussions and suggestions.

The author cannot find proper words to express the gratitude to Dr. Yuji Fukuda and Dr. Hironao Sakaki of Kansai Photon Science Institute, Japan Atomic Energy Agency for their rigorous guidance and unfailing encouragement, without which this work could never have accomplished.

The author is also indebted to Dr. Mamiko Nishiuchi, Dr. Satoshi Jinno, Dr. Akifumi Yogo, Dr. Koichi Ogura, Dr. Anatoly Ya. Faenov, Dr. Tatiana Pikuz, Dr. Kiminori Kondo, and Mr. Toshihiko Hori of Kansai Photon Science Institute, Japan Atomic Energy Agency for their cooperation in experiments and fruitful discussions.

The author wishes to thank Dr. Tomihiro Kamiya and Dr. Satoshi Kurashima of Takasaki Advanced Radiation Research Institute, Japan Atomic Energy Agency for their cooperation in experiments of ion irradiation at Takasaki Ion Accelerators for Advanced Radiation Application, TIARA.

The author would like to thank to Dr. Takashi Akagi of Hyogo Ion Beam Medical Center for fruitful discussions and cooperation in ion irradiation experiments.

The author also would like to thank to Dr. Kyo Kume and Dr. Takushi Takata of Wakasa-wan Energy Research Center for their valuable discussions and cooperation in ion irradiation experiments.

The author is much indebted to Mr. Yutaka Mori, Mr. Kenya Matsukawa and Ms.Yuri Matai of Laboratory of Radiation Sciences and Application of Graduate School of Maritime Sciences of Kobe University for supporting of this study. And also, the author would like to thank to Mr. Shunsuke Kaifu and Mr. Atsuto Hattori of graduate of the laboratory.

In closing, the author would like to express the special thanks to my family and Ms. Yu Nagai for supporting of my academic life.

References

[1] H. Daido, M. Nishiuchi, and A. S. Pirozhkov, "Review of laser-driven ion sources and their applications," Rep. Prog. Phys., 75 (2012) 056401 (71 pages).

[2] V. V. Lozhkarev, G. I. Freidman, V. N. Ginzburg, E. V. Katin, E. A. Khazanov, A. V. Kirsanov, G. A. Luchinin, A. N. Mal'shakov, M. A. Martyanov, O. V. Palashov, A. K. Poteomkin, A. M. Sergeev, A. A. Shaykin, I. V. Yakovlev, S. G. Garanin, S. A. Sukharev, N. N. Rukavishnikov, A. V. Charukhchev, R. R. Gerke and V. E. Yashin, "200 TW 45 fs laser based on optical parametric chirped pulse amplification," Opt. Express, 14 (2006) pp. 446-454.

[3] S. V. Bulanov, I. N. Inovenkov, V. I. Kirsanov, N. M. Naumova, and A. S. Sakharov, "Nonlinear depletion of ultrashort andrelativistically strong laser pulses in an underdense plasma," Phys. Fluids B, 4 (1992) pp. 1935-1942.

[4] G. Mourou, T. Tajima, and S. V. Bulanov, "Optics in the relativistic regime," Rev. Mod. Phys., 76 (2006) pp. 309-371.

[5] H. Kiriyama, M. Mori, Y. Nakai, T. Shimomura, H. Sasao, M. Tanoue, S. Kanazawa, D. Wakai, F. Sasao, H. Okada, I. Daito, M. Suzuki, S. Kondo, K. Kondo, A. Sugiyama, P. R. Bolton, A. Yokoyama, H. Daido, S. Kawanishi, T. Kimura, and T. Tajima, "High temporal and spatial quality petawatt-class Ti:sapphire chirped-pulse amplification laser system," Opt. Lett., 35 (2010) pp. 1497-1499.

[6] K. Ogura, M. Nishiuchi, A. S. Pirozhkov, T. Tanimoto, A. Sagisaka, T. Zh. Esirkepov, M. Kando, T. Shizuma, T. Hayakawa, H. Kiriyama, T. Shimomura, S. Kondo, S. Kanazawa, Y. Nakai, H. Sasao, F. Sasao, Y. Fukuda, H. Sakaki, M. Kanasaki, A. Yogo, S. V. Bulanov, P. B. Bolton, K. Kondo, "Proton acceleration to 40 MeV using a high intensity, high contrast optical parametric chirped-pulse amplification/Ti:sapphire hybrid laser system," Opt. Lett., 37 (2012) pp.2868-2870.

[7] Y. Fukuda, H. Sakaki, M. Kanasaki, A. Yogo, S. Jinno, M. Tampo, A.Ya. Faenov, T.A. Pikuz, Y. Hayashi, M. Kando, A.S. Pirozhkov, T. Shimomura, H. Kiriyama, S. Kurashima, T. Kamiya, K. Oda, T. Yamauchi, K. Kondo, S.V. Bulanov, "Identification of high energy ions using backscattered particles in laser-driven ion acceleration with cluster-gas targets," Radiat. Meas., 50 (2013) pp.92-96.

[8] Y. Fukuda, A. Ya. Faenov, M. Tampo, T. A. Pikuz, T. Nakamura, M. Kando, Y. Hayashi, A. Yogo, H. Sakaki, T. Kameshima, A. S. Pirozhkov, K. Ogura, M. Mori, T. Zh. Esirkepov, J. Koga, A. S. Boldarev, V. A. Gasilov, A. I. Magunov, T. Yamauchi, R. Kodama, P. R. Bolton, Y. Kato, T. Tajima, H. Daido, and S. V. Bulanov, "Energy Increase in Multi-MeV Ion Acceleration in the Interaction of a Short Pulse Laser with a Cluster-Gas Target," Phys. Rev. Lett., 103 (2009) 165002 (4 pages).

[9] G. Cristoforetti, M. P. Anania, A. Ya. Faenov, A. Giulietti, D. Giulietti, S. B. Hansen, P. Koester, L. Labate, T. Levato, T. A. Pikuz, and L. A. Gizzi, "Spatially resolved analysis of Kα x-ray emission from plasmas induced by a femtosecond weakly relativistic laser pulse at various polarizations," Phys. Rev. E, 87 (2013) 023103 (12 pages).

[10] B. Nordell, "Measurement of Photoneutron Energy Spectra from Tin, Lead and Uranium using an NE-213 Neutron Spectrometer," Nucl. Instrum. Meth., 224 (1984) pp.547-556.

[11] T. Ditmire, J. W. G. Tisch, E. Springate, M. B. Mason, N. Hay, J. P. Marangos, and M. H. R. Hutchinson, "High Energy Ion Explosion of Atomic Clusters: Transition from Molecular to Plasma Behavior," Phys. Rev. Lett., 78 (1997) pp.2732-2735

[12] S. P. Hatchett, C. G. Brown, T. E. Cowan, E. A. Henry, J. S. Johnson, M. H. Key, J. A. Koch, A. B. Langdon, B. F. Lasinski, R. W. Lee, A. J. Mackinnon, D. M. Pennington, M. D. Perry, T. W. Phillips, M. Roth, T. C. Sangster, M. S. Singh, R. A. Snavely, M. A. Stoyer, S. C. Wilks, and K. Yasuike, "Electron, photon, and ion beams from the relativistic interaction of Petawatt laser pulses with solid targets," Phys. Plasmas, 7 (2000) pp.2076-2082.

[13] M. Borghesi, D. H. Campbell, A. Schiavi, M. G. Haines, O. Willi, A. J. MacKinnon, P. Patel, L. A. Gizzi, M. Galimberti, R. J. Clarke, F. Pegoraro, H. Ruhl, and S. Bulanov, "Electric field detection in laser-plasma interaction experiments via the proton imaging technique," Phys. Plasmas, 9 (2012) pp.2214-2220.

[14] R. L. Fleischer, P. B. Price, and R. M. Walker: Nuclear Tracks in Solids: Principles and Applications (University of California Press, Berkeley, CA, 1975)

[15] M. Kanasaki, A. Hattori, H. Sakaki, Y. Fukuda, A. Yogo, S. Jinno, M. Nishiuchi, K. Ogura, K. Kondo, K. Oda, T. Yamauchi, "A high energy component of the intense laser-accelerated proton beams detected by stacked CR-39," Radiat. Meas., 50 (2013) pp.46-49.

[16] K. Oda, K. Yoshida, T. Yamauchi, Y. Honda, T. Ikeda, and S. Tagawa, "Effects of low-LET radiations on CR-39 track detector," Radiat. Meas., 28 (1997) pp.85-88.

[17] W. L. C. McLaughlin, J. C. Humphreys, D. Hocken, and W. J. Chappas, "Sensitometry of the response of a new radiochromic film dosimeter to gamma radiation and electron beams," Nucl. Instrum. Methods Phys. Res. A, 302 (1991) pp.165-176.

[18] T. Suzuki, C. Mori, K. Yanagida, A. Uritani, H. Miyahara, K. Takahashi, J. Miyahara, M. Yoshida, F. Takahashi, "Characteristics of prompt scintillation from imaging plate," Nucl. Instrum. Methods Phys. Res. A, 390 (1997) pp.155-159.

[19] C. G. Freeman, G. Fiksel, C. Stoeckl, N. Sinenian, M. J. Canfield, G. B. Graeper, A. T. Lombardo, C. R. Stillman, S. J. Padalino, C. Mileham, T. C. Sangster, and J. A. Frenje, "Calibration of a Thomson parabola ion spectrometer and Fujifilm imaging plate detectors for protons, deuterons, and alpha particles," Rev. Sci. Instrum., 82 (2011) 073301 (6 pages).

[20] A. Yogo, K. Sato, M. Nishikino, T. Maeda, H. Sakaki, T. Hori, K. Ogura, M. Nishiuchi, T. Teshima, H. Nishimura, K. Kondo, P. R. Bolton, and S. Kawanishi, "Measurement of DNA Double-Strand Break Yield in Human Cancer Cells by High-Current, Short-Duration Bunches of Laser-Accelerated Protons," Jpn. J. Appl. Phys., 50 (2011) 106401 (7 pages).

[21] K. Harres, M. Schollmeier, E. Brambrink, P. Audebert, A. Blažević, K. Flippo, D. C. Gautier, M. Geißel, B. M. Hegelich, F. Nürnberg, J. Schreiber, H. Wahl, and M. Roth, "Development and calibration of a Thomson parabola with microchannel plate for the detection of laser-accelerated MeV ions," Rev. Sci. Instrum., 79 (2008) 093306 (9 pages).

[22] H. Sakaki, M. Kanasaki, Y. Fukuda, M. Nishiuchi, T. Hori, A. Yogo, S. Jinno, and K. Niita, “Development of a single-shot-imaging thin film for an online Thomson parabola spectrometer,” Rev. Sci. Instrum., 84 (2013) 013301 (7 pages).

[23] K. Oda, M. Ito, H. Miyake, M. Michijima, and J. Yamamoto, “Track Formation in CR-39 Detector Exposed to D-T Neutron,” Nucl. Instrum. Methods Phys. Res. B, 35 (1988) pp.50-56.

[24] S. Kodaira, N. Yasuda, H. Kawashima, M. Kurano, N. Hasebe, T. Doke, S. Ota, T. Tsuruta, H. Hasegawa, S. Sakai, T. Nishi, K. Ogura, “Characteristics of the copolymerized CR-39/DAP track detector for the observation of ultra heavy nuclei in galactic cosmic rays,” Radiat. Meas., 44 (2009) pp.775-778.

[25] http://www.ppg.com/optical/opticalproducts/opticalmaterials/Pages/CR-39

[26] Y. Mori, T. Yamauchi, M. Kanasaki, Y. Maeda, K. Oda, S. Kodaira, T. Konishi, N. Yasuda, and Rémi Barillon, “Radiation chemical yields for loss of ether and carbonate ester bonds in PADC films exposed to proton and heavy ion beams,” Radiat. Meas., 46 (2011) pp.1147-1153.

[27] J. Drach, P.B. Price, M.H. Salamon, “Characteristics of cronar polyethylene terephthalate track detectors,” Nucl. Instrum. Methods. Phys. Res. Sec. B, 28 (1987) pp.49-52.

[28] R. L. Fleischer, P. B. Price, and R. M. Walker, “Criterion for Registration in Dielectric Track Detectors,” Phys. Rev., 156 (1967) pp.353-355.

[29] R. Barillon, M. Fromm, A. Chambaudet, H. Marah, A. Sabir, “Track etch velocity study in a radon detector (LR 115, cellulose nitrate),” Radiat. Meas., 28 (1997) pp.619-628.

[30] K Ogura, M Asano, N Yasuda, M Yoshida, “Properties of TNF-1 track etch detector,” Nucl. Instrum. Methods Phys. Res. B, 185 (2001) pp.222-227.

[31] G. Somogyi and S. A. Szalay, “Track-diameter kinetics in dielectric track detectors,” Nucl. Instrum. Methods, 109 (1973) pp.211-232.

[32] G. Somogyi, “Development of etched nuclear tracks,” Nucl. Instrum. Methods, 173 (1980) pp.21-42.

[33] R.P. Henke and E.V. Benton, “On geometry of tracks in dielectric nuclear track detectors,” Nucl. Instrum. Methods, 97 (1971) pp.483-489.

[34] H. G. Paretzke, E.V. Benton, and R.P. Henke, “On particle track evolution in dielectric track detectors and charge identification through track radius measurement,” Nucl. Instrum. Methods, 108 (1973) pp.73-80.

[35] T. Yamauchi, T. Taniguchi, and K. Oda, “Study on response of CR-39 detector to light ions,” Radiat. Meas., 31 (1999) pp.261-264.

[36] C. E. Johnson, E. R. Benton, N. Yasuda, E. V. Benton, “Analysis of short-range tracks and large track fluences in CR39 PNTD using atomic force microscopy,” Radiat. Meas., 44 (2009) pp.742-745.

[37] W. R. Leo, Techniques for Nuclear and Particle Physics Experiments: A How-to Approach (Springer-Verlag, Berlin/Heidelberg, 1992), p. 160.

[38] M. Katagiri, T. Nakamura, M. Ebine, A. Birumachi, S. Sato, E.M. Shooneveld, and N.J. Rhodes, “High-position-resolution neutron imaging detector with crossed wavelength shifting fiber read-out using two ZnS/6LiF scintillator sheets,” Nucl. Instrum. Methods Phys. Res. A, 573 (2007) pp.149-152.

[39] T. Sato, K. Niita, N. Matsuda, S. Hashimoto, Y. Iwamoto, S. Noda, T. Ogawa, H. Iwase, H. Nakashima, T. Fukahori, K. Okumura, T. Kai, S. Chiba, T. Furuta, and L. Sihver, "Particle and Heavy Ion Transport code System, PHITS, version 2.52," J. Nucl. Sci. and Technol., 50 (2013) pp.913-923.

[40] http://www.fieldp.com/amaze.html

[41] B. Dörschel, D. Hermsdorf, and S. Starke, "Influence of oxygen on the track etch rate along light ion trajectories in CR-39," Radiat. Meas., 40 (2005) pp.234-239.

[42] K. Oda, I. Csige, R. P. Henke, and E. V. Benton, "A new method for internal calibration of nuclear track detectors," Int. J. Radiat. Appl. Instrum. Nucl. Tracks Radiat. Meas., 20 (1992) pp.505-510.

[43] M. Fromm, F. Membrey, A. El Rahamany, and A. Chambaudet, "Principle of light ions micromapping and dosimetery using CR-39 polymeric detector: modelized and experimental uncertainties," Nucl. Tracks Radiat. Meas., 21 (1993) pp.357-365.

[44] J. F. Ziegler, "SRIM-2003," Nucl. Instrum. Meth. B, 219-220 (2004) pp.1027-1036.

[45] D. C. Carroll, P. Brummitt, D. Neely, F. Lindau, O. Lundh, C. G.Wahlstrom, and P. McKenna, "A modified Thomson parabola spectrometer for high resolution multi-MeV ion measurements -Application to laser-driven ion acceleration" Nucl. Instrum. Methods Phys. Res. A, 620 (2010) pp.23-27.

[46] H. Sakaki, M. Nishiuchi, T. Hori, P. R. Bolton, A. Yogo, M. Katagiri, K. Ogura, A. Sagisaka, A. S. Pirozhkov, S. Orimo, K. Kondo, H. Iwase, K. Niita, H. Souda, A. Noda, Y. Iseki, and T. Yoshiyuki, "Prompt In-Line Diagnosis of Single Bunch Transverse Profiles and Energy Spectra for Laser-Accelerated Ions," Appl. Phys. Express, 3 (2010) 126401 (3 pages).

[47] Y. Glinec, J. Faure, A. Guemnie-Tafo, V.Malka, H. Monard, J. P. Larbre, V. DeWaele, J. L. Marignier, and M. Mostafavi, "Absolute calibration for a broad range single shot electron spectrometer," Rev. Sci. Instrum., 77 (2006) 103301 (6 pages).

[48] S. Masuda, E. Miura, K. Koyama, and S. Kato, "Absolute calibration of an electron spectrometer using high energy electrons produced by the laser-plasma interaction," Rev. Sci. Instrum., 79 (2008) 083301 (4 pages).

[49] A. Henig, D. Kiefer, K. Markey, D. C. Gautier, K. A. Flippo, S. Letzring, R. P. Johnson, T. Shimada, L. Yin, B. J. Albright, K. J. Bowers, J. C. Ferna´ndez, S. G. Rykovanov, H.-C. Wu, M. Zepf, D. Jung, V. Kh. Liechtenstein, J. Schreiber, D. Habs, and B. M. Hegelich, "Enhanced Laser-Driven Ion Acceleration in the Relativistic Transparency Regime," Phys. Rev. Lett., 103 (2009) 045002 (4pages).

[50] A. S. Boldarev, V. A. Gasilov, and A. Y. Faenov, "On the generation of large clusters in forming gas-jet targets for lasers," Tech. Phys., 49 (2004) pp.388-395.

[51] S. Jinno, Y. Fukuda, H. Sakaki, A. Yogo, M. Kanasaki, K. Kondo, A.Ya. Faenov, I.Yu. Skobelev, T.A. Pikuz, A.S. Boldarev, and V.A. Gasilov, "Mie scattering from submicron-sized CO_2 clusters formed in a supersonic expansion of a gas mixture," Opt. Express, 21 (2013), pp.20656-20674.

[52] K. Arakawa, Y. Nakamura, W. Yokota, M. Fukuda, T. Nara, T. Agematsu, S. Okumura, I. Ishibori, T. Karasawa, R. Tanaka, A. Shimizu, T. Tachikawa, Y. Hayashi, K. Ishii, and T. Satoh: Proc. 13th Int. Conf. Cyclotrons and Their Applications, (1992) p.119.

[53] Y.L. Law, D. Nikezic, and K.N. Yu, "Optical appearance of alpha-particle tracks in CR-39 SSNTDs," Radiat. Meas., 43 (2008) pp.S128-S131.

[54] N. Yasuda, T. Konishi, K. Matsumoto, T. Yamauchi, T. Asuka, Y. Furusawa, Y. Sato, K. Oda, H. Tawara, K. Hieda, "Dose distribution of carbon ions in air assessed using imaging plates and ionization chamber," Radiat. Meas., 40 (2005) pp.384-388.

[55] F. Membrey, M. Fromm, A. El Rahamany, and A. Chambaudet, "Critical Angle for Light Ions Registered in a CR-39 SSNTD: Variations with Energy, Etching Conditions and Etching Time" Nucl. Tracks Radiat. Meas., 21 (1993) pp.417-424.

List of published papers by the author

- Original article

(1) CR-39 を用いたレーザー駆動陽子線計測における光中性子起因エッチピット弁別手法の開発
金崎真聡、福田祐仁、近藤公伯、小田啓二、山内知也、レーザー研究42巻2号、168-173 (2014).

(2) Laser-accelerated Protons as Diagnostic for Efficient Pulse Cleaning with a Saturable Absorber Pair and a Compensating Amplifier,
A. Yogo, K. Kondo, M. Mori, H. Kiriyama, K. Ogura, T. Shimomura, N. Inoue, Y. Fukuda, H. Sakaki, S. Jinno, M. Kanasaki, and P. R. Bolton, Optics Express 22, 2060-2069 (2014).

(3) A high energy component of the intense laser-accelerated proton beams detected by stacked CR-39,
M. Kanasaki, A. Hattori, H. Sakaki, Y. Fukuda, A. Yogo, S. Jinno, M. Nishiuchi, K. Ogura, K. Kondo, K. Oda, and T. Yamauchi, Radiation Measurements 50, 46-49 (2013).

(4) On the mechanism of the sensitization of PADC (poly(allyl diglycol carbonate)) track detectors by carbon dioxide treatment,
N. M. Hassan, Y. Matai, T. Kusumoto, Y. Mori, M. Kanasaki, K. Oda, H. Kitamura, T. Konishi, S. Kodaira, N. Yasuda, and T. Yamauchi, Radiation Measurements 59, 23-29 (2013).

(5) Mie scattering from submicron-sized CO_2 clusters formed in a supersonic expansion of a gas mixture,
S. Jinno, Y. Fukuda, H. Sakaki, A. Yogo, M. Kanasaki, K. Kondo, A.Ya. Faenov, I.Yu. Skobelev, T.A. Pikuz, A.S. Boldarev, and V.A. Gasilov, Optics Express 21, 20656-20674 (2013).

(6) Characterization of submicron-sized CO_2 clusters formed with a supersonic expansion of a mixed-gas using a three-staged nozzle,
S. Jinno, Y. Fukuda, H. Sakaki, A. Yogo, M. Kanasaki, K. Kondo, A. Ya. Faenov, I. Yu. Skobelev, T. A. Pikuz, A. S. Boldarev, and V. A. Gasilov, Applied Physics Letter 102, 164103 (4 pages) (2013).

(7) Applicability of Polyimide Films as Etched-Track Detectors for Ultra-Heavy Cosmic Ray Components,
T. Yamauchi, K. Matsukawa, Y. Mori, M. Kanasaki, A. Hattori, Y. Matai, T. Kusumoto, A. Tao, K. Oda, S. Kodaira, T. Konishi, H. Kitamura, N. Yasuda, and R. Barillon, Applied Physics Express 6, 046401 (4 pages) (2013).

(8) Applicability of the polyimide films as an SSNTD material,
T. Yamauchi, S. Kaifu, Y. Mori, M. Kanasaki, K. Oda, S. Kodaira, T. Konishi, N. Yasuda, and R. Barillon, Radiation Measurements 50, 16-21 (2013).

(9) Chemical cross sections induced by ions in solid organic detectors: Experimentation and simulation,
R. Barillon, Y. Mori, M. Kanasaki, T. Yamauchi, and N. Yasuda, Radiation Measurements 50, 38-42 (2013).

(10) Identification of high energy ions using backscattered particles in laser-driven ion acceleration with cluster-gas targets,
Y. Fukuda, H. Sakaki, M. Kanasaki, A. Yogo, S. Jinno, M. Tampo, A.Ya. Faenov, T.A. Pikuz, Y. Hayashi, M. Kando, A.S. Pirozhkov, T. Shimomura, H. Kiriyama, S. Kurashima, T. Kamiya, K. Oda, T. Yamauchi, K. Kondo, and S.V. Bulanov, Radiation Measurements 50, 92-96 (2013).

(11) Vacuum effects on the radiation chemical yields in PADC films exposed to gamma rays and heavy ions,
Y. Mori, T. Yamauchi, M. Kanasaki, A. Hattori, K. Oda, S. Kodaira, T. Konishi, N. Yasuda, S. Tojo, Y. Honda, and R. Barillon, Radiation Measurements 50, 97-102 (2013).

(12) Development of a single-shot-imaging thin film for an online Thomson parabola spectrometer,
H. Sakaki, M. Kanasaki, Y. Fukuda, M. Nishiuchi, T. Hori, A. Yogo, S. Jinno, K. Niita, Review of Scientific Instruments 84, 013301 (7 pages) (2013).

(13) The Diagnosis Method for High-Energy Ion Beams Using Backscattered Particles for Laser-Driven Ion Acceleration Experiments,
M. Kanasaki, Y. Fukuda, H. Sakaki, T. Hori, M. Tampo, K. Kondo, S. Kurashima, T. Kamiya, K. Oda and T. Yamauchi, Japanese Journal of Applied Physics 51, 056401 (4pages) (2012).

(14) Greater Radiation Chemical Yields for Losses of Ether and Carbonate Ester Bonds at Lower Stopping Powers along Heavy Ion Tracks in Poly(allyl diglycol carbonate) Films,
Y. Mori, T. Yamauchi, M. Kanasaki, A. Hattori, Y. Matai, K. Matsukawa, K. Oda, S. Kodaira, H. Kitamura, T. Konishi, N. Yasuda, S. Tojo, Y. Honda, and R. Barillon, Applied Physics Express 5, 086401 (3 pages) (2012).

(15) Proton acceleration to 40 MeV using a high intensity, high contrast optical parametric chirped-pulse amplification/Ti:sapphire hybrid laser system,
K. Ogura, M. Nishiuchi, A. S. Pirozhkov, T. Tanimoto, A. Sagisaka, T. Zh. Esirkepov, M. Kando, T. Shizuma, T. Hayakawa, H. Kiriyama, T. Shimomura, S. Kondo, S. Kanazawa, Y. Nakai, H. Sasao, F. Sasao, Y. Fukuda, H. Sakaki, M. Kanasaki, A. Yogo, S. V. Bulanov, P. R. Bolton, and K. Kondo, Optics Letters 37, 2868-2870 (2012).

(16) Thresholds of Etchable Track Formation and Chemical Damage Parameters in Poly(ethylene terephthalate), Bisphenol A polycarbonate, and Poly(allyl diglycol carbonate) Films at the Stopping Powers Ranging from 10 to 12,000 keV/μm,
T. Yamauchi, Y. Mori, A. Morimoto, M. Kanasaki, K. Oda, S. Kodaira, T. Konishi, N. Yasuda, S. Tojo, Y. Honda, and R. Barillon, Japanese Journal of Applied Physics 51, 056301 (5 pages) (2012).

(17) Quasi-monochromatic pencil beam of laser-driven protons generated using a conical cavity target holder,
M. Nishiuchi, A. S. Pirozhkov, H. Sakaki, K. Ogura, T. Zh. Esirkepov, T. Tanimoto, M. Kanasaki, A. Yogo, T. Hori, A. Sagisaka, Y. Fukuda, Y. Matsumoto, S. Entani, S. Sakai, C. M. Brenner, D. Neely, T. Yamauchi, S. V. Bulanov, and K. Kondo, Physics of Plasmas 19, 030706 (4 pages) (2012).

(18) CR-39を用いた後方散乱粒子による高強度ビーム簡易診断法
金崎真聡、福田裕仁、榊　泰直、堀　利彦、反保元伸、近藤公伯、倉島　俊、神谷富裕、山内知也、放射線37巻、127-131 (2011).

(19) イオン照射したPADC固体飛跡検出器の表面特性評価
森　豊、前田佑介、金崎真聡、山内知也、小田啓二、蔵岡孝治、安田仲宏、小西輝昭、小平　聡、誉田義英、藤乗幸子、放射線37巻、149-155 (2011).

(20) 新しい固体飛跡検出器としてのポリイミド薄膜
海部俊介、森　豊、金崎真聡、山内知也、小田啓二、小平　聡、小西輝昭、安田仲宏、放射線37巻、157-163 (2011).

(21) クラスターターゲットを用いた革新的レーザー駆動イオン加速研究における固体飛跡検出器CR-39の利用
福田祐仁、反保元伸、榊　泰直、近藤公伯、金崎真聡、山内知也、放射線37巻、169-172 (2011).

(22) Sensitization of PADC track detector in carbon dioxide gas,
T. Yamauchi, Y. Mori, H. Chikada, A. Sakamoto, J. Kii, M. Kanasaki, K. Oda, and M. Fujii, Radiation Measurements 44, 1105-1108 (2009).

- Proceedings

(1) Multi-charged heavy ion acceleration from the ultra-intense short pulse laser system interacting with the metal target,
M. Nishiuchi, H. Sakaki, S. Maeda, A. Sagisaka, A. S. Pirozhkov, T. Pikuz, A. Faenov, K. Ogura, M. Kanasaki, K. Matsukawa, T. Kusumoto, A. Tao, T. Fukami, T. Esirkepov, J. Koga, H. Kiriyama, H. Okada, T. Shimomura, M. Tanoue, Y. Nakai, Y. Fukuda, S. Sakai, J. Tamura, K. Nishio, H. Sako, M. Kando, T. Yamauchi, Y. Watanabe, S. V. Bulanov, and K. Kondo, Review of Scientific Instruments 85, 02B904 (3 pages) (2013).

(2) Measurements of electron-induced neutrons as a tool for determination of electron temperature of fast electrons in the task of optimization laser-produced plasma ions acceleration,
H. Sakaki, M. Nishiuchi, S. Maeda, A. Sagisaka, A. S. Pirozhkov, T. Pikuz, A. Faenov, K. Ogura, T. Fukami, K. Matsukawa, M. Kanasaki, Y. Fukuda, A. Yogo, T. Esirkepov, H. Kiriyama, T. Shimomura, Y. Nakai, M. Tanoue, K. Torimoto, M. Okamoto, T. Sato, K. Niita, J. Tamura, K. Nishio, H. Sako, T. Yamauchi, Y. Watanabe, S. Bulanov, and K. Kondo, Review of Scientific Instruments 85, 02A705 (3 pages) (2013).

(3) PADC 飛跡検出器中に形成される重イオントラックの構造分析
森　豊、楠本多聞、松川兼也、又井悠里、金崎真聡、小田啓二、小平　聡、北村　尚、小西輝昭、安田仲宏、藤乗幸子、誉田義英、山内知也、神戸大学大学院海事科学研究科紀要10巻、21-32 (2013).

(4) A diagnosis of intense ion beam by CR-39 detectors analyzing the back scattered particles,
M. Kanasaki, T. Yamauchi, Y. Fukuda, H. Sakaki, T. Hori, M. Tampo, S. Kurashima, T. Kamiya, K. Oda, and K. Kondo, AIP Conference Proceedings 1465, 142-147 (2012)

(5) Electron energy transport in the thin foil driven by high contrast high intensity laser pulse,
T. Tanimoto, M. Nishiuchi, Y. Mishima, K. Kikuyama, T. Morioka, K. Morita, M. Kanasaki, A. S. Pirozhkov, A. Yogo, K. Ogura, Y. Fukuda, H. Sakaki, A. Sagisaka, H. Habara, K. A. Tanaka, and K. Kondo, AIP Conference Proceedings 1465, 148-151 (2012).

(6) Recent progress in particle acceleration from the interaction between thin-foil targets and J-KAREN laser pulses,
M. Nishiuchi, A. S. Pirozhkov, H. Sakaki, K. Ogura, T. Zh Esirkepov, T.Tanimoto, A. Yogo, T. Hori, A. Sagisaka, Y. Fukuda, M. Kanasaki, H. Kiriyama, T. Shimomura, M. Tanoue, Y. Nakai, H. Sasao, F. Sasao, S. Kanazawa, S. Kondo, Y. Matsumoto, S. Sakai, C. Brenner, D. Neely, S. V. Bulanov, and K. Kondo, AIP Conference Proceedings 1465, 148-151 (2012).

(7) 二酸化炭素処理による PADC 飛跡検出器の増感機構
深尾裕亮、金崎真聡、森　豊、山内知也、小田啓二、小西輝昭、安田仲宏、神戸大学大学院海事科学研究科紀要9巻、69-78 (2012).

(8) プロトン照射した PADC 検出器表面上液滴の接触角異常
前田佑介、森　豊、金崎真聡、山内知也、小田啓二、小西輝昭、安田仲宏、藤乗幸子、誉田義英、蔵岡孝治、神戸大学大学院海事科学研究科紀要8巻、21-29 (2011).

(9) 紫外線照射下における高分子系飛跡検出器中カーボネートエステル結合損失の量子収率
坂本淳志、森　豊、金崎真聡、山内知也、小田啓二、神戸大学大学院海事科学研究科紀要7巻、87-98 (2010).

- Commentary

(1) イオンビーム特性評価を目的とした固体飛跡検出器 CR-39 の利用
金崎真聡、福田祐仁、榊　泰直、西内満美子、近藤公伯、倉島　俊、神谷富裕、服部篤人、小田啓二、山内知也、プラズマ・核融合学会誌88巻5号、261-275 (2012).

List of lectures by the author

- International conference

・ Oral presentation

(1) The Effect of Photo-Neutrons on Diagnostics Using CR-39 for Laser-Accelerated Ion Beam,
M. Kanasaki, Y. Fukuda, H. Sakaki, A. Yogo, S. Jinno, M. Nishiuchi, A. Hattori, K. Matsukawa, K. Kondo, K. Oda and T. Yamauchi, The 10th Conference on Lasers and Electro Optics Pacific Rim, MD1-8, Kyoto, Japan (June-July 2013).

(2) High energy components of the intense laser-driven proton beams detected by stacked CR-39,
M. Kanasaki, T. Yamauchi, M. Nishiuchi, A. S. Pirozhkov, H. Sakaki, K. Ogura, T. Tanimoto, A. Yogo, T. Hori, A. Sagisaka Y. Fukuda, H. Kiriyama, T. Shimomura, S. Kanazawa, K. Oda, and K. Kondo, 25th International Conference on Nuclear Tracks in Solids, ID093, Puebra, Mexico (September 2011).

(3) A diagnosis of intense ion beam by CR-39 detectors analyzing the back scattered particles,
M. Kanasaki, T. Yamauchi, Y. Fukuda, H. Sakaki, T. Hori, M. Tampo, S. Kurashima, T. Kamiya, K. Oda, and K. Kondo, he 3rd International Symposium Laser-Driven Relativistic Plasmas Applied to Science, Energy, Industry, and Medicine, Kyoto, Japan (June 2011).

・ Poster presentation

(1) A diagnosis method of laser-accelerated protons using CR-39 in a field contaminated by photo-neutrons,
M. Kanasaki, Y. Fukuda, H. Sakaki, A. Yogo, S. Jinno, M. Nishiuchi, K. Matsukawa, K. Kondo, K. Oda, and T. Yamauchi, The Eighth International Conference on Inertial Fusion Sciences and Applications, P.Th_44, Nara, Japan (September 2013).

(2) Design of a wide energy range stacked CR-39 detector diminishing contaminant photo-neutrons using Monte Carlo particle transport simulations,
M. Kanasaki, Y. Fukuda, H. Sakaki, A. Yogo, S. Jinno, M. Nishiuchi, A. Hattori, K. Matsukawa, K. Kondo, K. Oda, and T. Yamauchi, The International Symposium on Ultrafast Intense Laser Science, P-26, Jeju, Korea (October 2012).

- Domestic conference

(1) レーザー駆動イオンビーム計測における光中性子の影響評価
金崎真聡、福田祐仁、榊　泰直、余語覚文、神野智史、西内満美子、服部篤人、松川兼也、近藤公伯、小田啓二、山内知也、第60回応用物理学会春季学術講演会、厚木 (2013年3月).

(2) CR-39 及び ZnS(Ag)蛍光膜による固体ターゲットを用いたレーザー駆動イオンビームの計測
金崎真聡、福田祐仁、榊　泰直、余語覚文、神野智史、西内満美子、小倉浩一、赤城　卓、近藤公伯、小田啓二、山内知也、第27回固体飛跡検出器研究会、神戸 (2013年3月).

(3) 後方散乱粒子によるレーザー駆動イオンビームの簡易診断法
金崎真聡、福田祐仁、榊　泰直、余語覚文、神野智史、倉島　俊、神谷富裕、近藤公伯、小田啓二、山内知也、第27回固体飛跡検出器研究会、神戸 (2013年3月).

(4) クラスターターゲットを用いたレーザー駆動イオン加速実験における光中性子の評価
金崎真聡、福田祐仁、榊　泰直、余語覚文、神野智史、西内満美子、近藤公伯、小田啓二、山内知也、第27回固体飛跡検出器研究会、神戸 (2013年3月).

(5) レーザー駆動イオン加速実験における光中性子を考慮したイオン計測
金崎真聡、福田祐仁、榊　泰直、余語覚文、神野智史、西内満美子、服部篤人、松川兼也、近藤公伯、小田啓二、山内 知也、レーザー学会学術講演会第33回年次大会、姫路 (2013年1月).

(6) レーザー駆動イオンビーム・オンラインイメージング解析用 ZnS(Ag)蛍光膜の発光応答特性評価
金崎真聡、榊　泰直、福田祐仁、余語覚文、神野智史、近藤公伯、赤城　卓、服部篤人、松川兼也、小田啓二、山内知也、13p-B2-8、第73回応用物理学会学術講演会、愛媛 (2012年9月).

(7) CR-39 を用いた後方散乱粒子による高強度イオンビーム特性簡易診断法
金崎真聡、山内知也、福田祐仁、榊　泰直、堀　利彦、反保元伸、倉島　俊、神谷富裕、近藤公伯、第26回固体飛跡検出器研究会、神戸 (2012年3月).

(8) CR-39 を用いたレーザー駆動陽子線の高精度計測
金崎真聡、福田祐仁、榊　泰直、余語覚文、神野智史、西内満美子、小倉浩一、近藤公伯、小田啓二、山内知也、レーザー学会学術講演会第32回年次大会、仙台 (2012年1月).

(9) CR-39 を用いた後方散乱粒子による高強度イオンビーム特性簡易診断法
金崎真聡、山内知也、福田祐仁、榊　泰直，堀　利彦、反保元伸、倉島　俊、神谷富裕、近藤公伯、第58回応用物理学関係連合講演会、厚木 (2011年3月).

(10) PADC 飛跡検出器中に形成されるトラックに沿った水の密度

金崎真聡、森　豊、前田佑介、山内知也、小田啓二、小西輝昭、安田仲宏、第71回応用物理学会学術講演会、17a-L-3、長崎 (2010年9月).

(11) 二酸化炭素を吸蔵させた PADC の特性評価 (2)

金崎真聡、近田　啓、森　豊、坂本淳志、深尾裕亮、山内知也、小田啓二、小西輝昭、安田仲宏、第57回応用物理学関係連合講演会、神奈川 (2010年3月).

(12) PADC 飛跡検出器中に形成されるトラックに沿った水の密度

金崎真聡、浦城翔太、森　豊、坂本淳志、山内知也、小田啓二、小西輝昭、安田仲広、第25回固体飛跡検出器研究会、東京 (2010年3月).

(13) PADC 飛跡検出器中ヒドロキシル基濃度の評価

金崎真聡、森　豊、坂本淳志、山内知也、小田啓二、小西輝昭、安田仲宏、第70回応用物理学会学術講演会、富山 (2009年9月).

(14) 赤外分光法による有機材料中水酸基定量評価

金崎真聡、森　豊、坂本淳志、山内知也、小田啓二、第24回固体飛跡検出器研究会、東京 (2009年3月).